12-16-2020

Observations of the Origin of Downward Terrestrial Gamma-Ray Flashes

J. W. Belz
The University of Utah

P. R. Krehbiel
New Mexico Institute of Mining and Technology

J. Remington
The University of Utah

M. A. Stanley
New Mexico Institute of Mining and Technology

R. U. Abbasi
Loyola University Chicago

See next page for additional authors

Observations of the Origin of Downward Terrestrial Gamma-Ray Flashes

J.W. Belz[1], P.R. Krehbiel[2], J. Remington[1], M.A. Stanley[2], R.U. Abbasi[3], R. LeVon[1], W. Rison[2], D. Rodeheffer[2]

and the Telescope Array Scientific Collaboration

T. Abu-Zayyad[1], M. Allen[1], E. Barcikowski[1], D.R. Bergman[1], S.A. Blake[1], M. Byrne[1], R. Cady[1], B.G. Cheon[6], M. Chikawa[8], A. di Matteo[9*], T. Fujii[10], K. Fujita[11], R. Fujiwara[11], M. Fukushima[12,13], G. Furlich[1], W. Hanlon[1], M. Hayashi[14], Y. Hayashi[11], N. Hayashida[15], K. Hibino[15], K. Honda[16], D. Ikeda[17], T. Inadomi[18], N. Inoue[4], T. Ishii[16], H. Ito[19], D. Ivanov[1], H. Iwakura[18], H.M. Jeong[20], S. Jeong[20], C.C.H. Jui[1], K. Kadota[21], F. Kakimoto[5], O. Kalashev[22], K.Kasahara[23], S. Kasami[24], H. Kawai[25], S. Kawakami[11], K. Kawata[12], E. Kido[12], H.B. Kim[6], J.H. Kim[1], J.H. Kim[11], V. Kuzmin[22†], M. Kuznetsov[9,22], Y.J. Kwon[26], K.H. Lee[20], B. Lubsandorzhiev[22], J.P. Lundquist[1], K. Machida[16], H. Matsumiya[11], J.N. Matthews[1], T. Matuyama[11], R. Mayta[11], M. Minamino[11], K. Mukai[16], I. Myers[1], S. Nagataki[19], K. Nakai[11], R. Nakamura[18], T. Nakamura[27], Y. Nakamura[18], T. Nonaka[12], H. Oda[11], S. Ogio[11,28], M.Ohnishi[12], H. Ohoka[12], Y. Oku[24], T. Okuda[29], Y. Omura[11], M. Ono[19], A. Oshima[36], S. Ozawa[23], I.H. Park[20],M. Potts[1], M.S. Pshirkov[22,30], D.C. Rodriguez[1], G. Rubtsov[22], D. Ryu[31], H. Sagawa[12], R. Sahara[11], K. Saito[12], Y. Saito[18], N. Sakaki[12], T. Sako[12], N. Sakurai[11], K. Sano[18], T. Seki[18], K. Sekino[12], F. Shibata[16], T. Shibata[12], H. Shimodaira[12], B.K. Shin[11], H.S. Shin[12], J.D. Smith[1], P. Sokolsky[1], N. Sone[18], B.T. Stokes[1], T.A. Stroman[1], Y. Takagi[11], Y. Takahashi[11], M. Takeda[12], R. Takeishi[20], A. Taketa[17], M. Takita[12], Y. Tameda[24], K. Tanaka[32], M. Tanaka[33], Y. Tanoue[11], S.B. Thomas[1], G.B. Thomson[1], P. Tinyakov[9,22], I. Tkachev[22], H. Tokuno[5], T. Tomida[18], S. Troitsky[22], Y. Tsunesada[11,28], Y. Uchihori[34], S. Udo[15], T. Uehama[18], F. Urban[35], M. Wallace[1], T. Wong[1], M. Yamamoto[18], H. Yamaoka[33], K. Yamazaki[36], K. Yashiro[7], M. Yosei[24], H. Yoshii[37], Y. Zhezher[12,22], Z. Zundel[1]

[1]Department of Physics and Astronomy, University of Utah, Salt Lake City, Utah, USA
[2]Langmuir Laboratory for Atmospheric Research, New Mexico Institute of Mining and Technology, Socorro, NM, USA
[3]Department of Physics, Loyola University Chicago, Chicago, Illinois, USA
[4]The Graduate School of Science and Engineering, Saitama University, Saitama, Saitama, Japan
[5]Graduate School of Science and Engineering, Tokyo Institute of Technology, Meguro, Tokyo, Japan
[6]Department of Physics and The Research Institute of Natural Science, Hanyang University, Seongdong-gu, Seoul, Korea
[7]Department of Physics, Tokyo University of Science, Noda, Chiba, Japan
[8]Department of Physics, Kindai University, Higashi Osaka, Osaka, Japan
[9]Service de Physique Théorique, Université Libre de Bruxelles, Brussels, Belgium
[10]The Hakubi Center for Advanced Research, Kyoto University, Kitashirakawa-Oiwakecho, Sakyo-ku, Kyoto, Japan
[11]Graduate School of Science, Osaka City University, Osaka, Osaka, Japan
[12]Institute for Cosmic Ray Research, University of Tokyo, Kashiwa, Chiba, Japan
[13]Kavli Institute for the Physics and Mathematics of the Universe (WPI), University of Tokyo, Kashiwa, Chiba, Japan
[14]Information Engineering Graduate School of Science and Technology, Shinshu University, Nagano, Nagano, Japan
[15]Faculty of Engineering, Kanagawa University, Yokohama, Kanagawa, Japan
[16]Interdisciplinary Graduate School of Medicine and Engineering, University of Yamanashi, Kofu, Yamanashi, Japan
[17]Earthquake Research Institute, University of Tokyo, Bunkyo-ku, Tokyo, Japan
[18]Academic Assembly School of Science and Technology Institute of Engineering, Shinshu University, Nagano, Nagano, Japan
[19]Astrophysical Big Bang Laboratory, RIKEN, Wako, Saitama, Japan
[20]Department of Physics, Sungkyunkwan University, Jang-an-gu, Suwon, Korea

[21]Department of Physics, Tokyo City University, Setagaya-ku, Tokyo, Japan
[22]Institute for Nuclear Research of the Russian Academy of Sciences, Moscow, Russia
[23]Advanced Research Institute for Science and Engineering, Waseda University, Shinjuku-ku, Tokyo, Japan
[24]Department of Engineering Science, Faculty of Engineering, Osaka Electro-Communication University, Neyagawa-shi, Osaka, Japan
[25]Department of Physics, Chiba University, Chiba, Chiba, Japan
[26]Department of Physics, Yonsei University, Seodaemun-gu, Seoul, Korea
[27]Faculty of Science, Kochi University, Kochi, Kochi, Japan
[28]Nambu Yoichiro Institute of Theoretical and Experimental Physics, Osaka City University, Osaka, Osaka, Japan
[29]Department of Physical Sciences, Ritsumeikan University, Kusatsu, Shiga, Japan
[30]Sternberg Astronomical Institute, Moscow M.V. Lomonosov State University, Moscow, Russia
[31]Department of Physics, Ulsan National Institute of Science and Technology, UNIST-gil, Ulsan, Korea
[32]Graduate School of Information Sciences, Hiroshima City University, Hiroshima, Hiroshima, Japan
[33]Institute of Particle and Nuclear Studies, KEK, Tsukuba, Ibaraki, Japan
[34]National Institute of Radiological Science, Chiba, Chiba, Japan
[35]CEICO, Institute of Physics, Czech Academy of Sciences, Prague, Czech Republic
[36]Engineering Science Laboratory, Chubu University, Kasugai, Japan
[37]Department of Physics, Ehime University, Matsuyama, Ehime, Japan

Key Points:

- Downward Terrestrial Gamma-ray Flashes occur during strong initial breakdown pulses of negative cloud-to-ground and cloud lightning.
- The initial breakdown pulses consist of streamer-based fast negative breakdown having transient sub-pulse conducting events, or 'sparks'.
- The streamer to leader transition of negative stepping occurs during strong currents in the final stage of initial breakdown pulses.

* Currently at INFN, sezione di Torino, Turin, Italy
† Deceased

Corresponding author: Jackson Remington, jremington@cosmic.utah.edu

Abstract

In this paper we report the first close, high-resolution observations of downward-directed terrestrial gamma-ray flashes (TGFs) detected by the large-area Telescope Array cosmic ray observatory, obtained in conjunction with broadband VHF interferometer and fast electric field change measurements of the parent discharge. The results show that the TGFs occur during strong initial breakdown pulses (IBPs) in the first few milliseconds of negative cloud-to-ground and low-altitude intracloud flashes, and that the IBPs are produced by a newly-identified streamer-based discharge process called fast negative breakdown. The observations indicate the relativistic runaway electron avalanches (RREAs) responsible for producing the TGFs are initiated by embedded spark-like transient conducting events (TCEs) within the fast streamer system, and potentially also by individual fast streamers themselves. The TCEs are inferred to be the cause of impulsive sub-pulses that are characteristic features of classic IBP sferics. Additional development of the avalanches would be facilitated by the enhanced electric field ahead of the advancing front of the fast negative breakdown. In addition to showing the nature of IBPs and their enigmatic sub-pulses, the observations also provide a possible explanation for the unsolved question of how the streamer to leader transition occurs during the initial negative breakdown, namely as a result of strong currents flowing in the final stage of successive IBPs, extending backward through both the IBP itself and the negative streamer breakdown preceding the IBP.

1 Introduction

The interplay between lightning and high-energy particle physics was realized over two decades ago with the serendipitous observation of gamma radiation emanating from the Earth. The BATSE (Burst and Transient Source Experiment) instrument aboard NASA's Compton Gamma-Ray Observatory was designed to detect radiation from Gamma Ray Bursts (GRBs), deep-space events which are considered the most intense sources of electromagnetic radiation in the Universe. In 1994, BATSE unexpectedly recorded a series of brief, intense flashes of gamma rays, which appeared to originate at high altitudes ($\geq$15 km above ground level) above thunderstorm regions (Carlson et al., 2007; Fishman et al., 1994). The terrestrial gamma-ray flashes (TGFs) lasted from hundreds of microseconds up to a millisecond or more, and their energy spectrum was consistent with bremsstrahlung emission from electrons with energies of several million electron volts (MeV) or greater.

Subsequent observations, now numbering in the thousands of events, aboard the Ramaty High Energy Solar Spectroscopic Imager (RHESSI) satellite (Gjesteland et al., 2012; Grefenstette et al., 2009), NASA's Fermi Gamma-ray Space Telescope (Briggs et al., 2013; Foley et al., 2014; Roberts et al., 2017), and the Astrorivelatore Gamma a Immagini Leggero (AGILE) satellite (Marisaldi et al., 2014) have shown that, instead of being produced at high altitude above storms, the TGFs originate at lower altitudes commensurate with being inside storms. In particular, it has been shown that the TGFs are produced at the altitudes of intracloud (IC) lightning flashes, during upward negative breakdown at the beginning of the flashes (Cummer et al., 2011, 2015; Lu et al., 2010; Lyu et al., 2016; Mailyan et al., 2016; Shao et al., 2010; Stanley et al., 2006). The early RHESSI observations were found to be associated with millisecond-duration initial breakdown activity that occurs in the beginning stages of IC flashes. However, a direct connection with the initial breakdown events was uncertain due to a 1-3 ms timing uncertainty in the RHESSI data (Lu et al., 2011).

In recent years, a small subset of TGFs has been associated with high-peak current (few hundred kiloampere) IC discharge events, called energetic in-cloud pulses (EIPs) (Lyu et al., 2015). EIPs are energetic versions of what are called preliminary or initial breakdown pulses (Marshall et al., 2013), that are characteristic features of the beginning stages

of IC and negative cloud-to-ground (−CG) flashes. The EIP studies have utilized data from the Gamma-ray Burst Monitor (GBM) on Fermi (Briggs et al., 2010), which detects individual photons with microsecond timing accuracy, allowing more accurate correlation with ground-based low frequency (LF) radio atmospheric or "sferic" observations. Although EIPs are infrequent and the number of documented cases is small (a dozen or so), TGFs have been detected for 100% of EIPs that occurred within view of the Fermi satellite and within range of ground-based sferic sensors. As a result of this predictability, EIPs are considered to be high-probability producers of at least a class of TGF-generating lightning events (Cummer et al., 2017; Lyu et al., 2016, 2018). However, the detailed discharge processes that produce EIPs has not been understood, due to the lack of measurements of the parent flashes with ground-based instrumentation (such observations of a close EIP by Tilles (2020), reported while this paper was in review, provides the first detailed information on the discharge processes and storm environment that led to its occurrence, as discussed later).

As satellite-based observations of upward TGFs have accumulated, the question has been whether lightning produces downward TGFs that could be detected on the ground below or near thunderstorms. In particular, negative-polarity cloud-to-ground (−CG) discharges begin with downward negative breakdown that would be expected to produce TGFs directed earthward. Until recently, only a few TGFs had been detected at ground level in association with overhead lightning. Instead of being produced in the early stages of natural lightning, however, the gamma rays occurred either during the upward ascent of artificial trailing-wire, rocket-triggered lightning discharges (Dwyer, 2004; Hare et al., 2016), or at a later time in natural flashes, following high-current return strokes of −CG discharges (Dwyer et al., 2012; Ringuette et al., 2013; Tran et al., 2015). Also, a particularly strong downward TGF was recently reported during a winter thunderstorm by Wada et al. (2019) at the time of lightning discharge in the storm that appeared to be produced at low altitude ($\simeq$400 m) above ground. Otherwise, significant impediments to detecting downward TGFs have been a) the increasingly strong attenuation of gamma radiation at low altitudes in the atmosphere, and b) the ground-based detectors being either too far below and/or not widespread enough to detect the forward-beamed radiation. Both issues have been addressed with observations from the large-area (700 km^2) Telescope Array Surface Detector (TASD) cosmic ray facility in central Utah.

In data collected between 2008 and 2013 there were ten occasions in which the TASD was triggered by multiple bursts of energetic particles — not arising from cosmic rays. The events occurred within a millisecond of being detected by the U.S. National Lightning Detection Network (NLDN) (Abbasi et al., 2017), which identified them as being produced during −CG flashes. Follow-up observations with the TASD by the authors of the present study, obtained between 2014 and 2016 in coordination with a 3-D lightning mapping array (LMA) and a lightning electric field change sensor, detected ten additional events, each consisting of three to five lightning-initiated bursts (Abbasi et al., 2018). The bursts were typically $\simeq$10 μs or less in duration, and occurred over several hundred μs time intervals during the first millisecond of downward negative breakdown at the beginning of −CG flashes. Scintillator responses and simulation studies showed that the bursts primarily resulted from gamma radiation and collectively comprised low-fluence TGFs. The LMA observations showed the bursts coincided with impulsive in-cloud VHF radiation events during energetic downward negative breakdown, 3-4 km above ground level. Although the TASD and LMA observations had sub-microsecond time resolution, the electric field change measurements recorded only the relatively slow electrostatic field change, with insufficient bandwidth to detect the faster electric field changes of the initial breakdown activity.

Here we report observations of downward TGFs produced by four additional flashes (three –CGs and one low-altitude IC flash) obtained in 2018 during continued studies with the Telescope Array. For this study, the TASD and LMA observations were aug-

mented with crucially important, high-resolution VHF interferometric and fast electric field change measurements of the parent lightning discharges, obtained in relatively close proximity (16–24 km) to the TGFs. Coupled with sub-microsecond TGF measurements at TASD stations immediately below and near the flashes, the observations document the TGF occurrence with a high degree of temporal and spatial resolution not available before now. In each of the four flashes, the TGFs show a clear correspondence with downward negative breakdown during strong initial breakdown pulse (IBP) events in the first millisecond or so of the flashes. The negative breakdown progresses at a fast average speed ($\simeq$1–3 $\times 10^7$ m/s), indicative of a newly-recognized type of discharge process called fast negative breakdown (FNB) (Tilles et al., 2019). Such breakdown is the negative analog of fast positive breakdown found in an earlier study to be the cause of high-power discharges called narrow bipolar events (NBEs) (Rison et al., 2016).

For both polarities, the breakdown is produced by a propagating system of streamers that substantially enhance (up to 50% or more) the electric field ahead of the streamers' advancing front (Attanasio et al., 2019). For the negative polarity version, electron avalanches produced within the streamer system would propagate through and ahead of the advancing front, producing downward-directed gamma radiation. Detailed analysis of the observations indicate that the TGFs are often initiated at the time of characteristic "sub-pulses" that occur during large-amplitude, 'classic' sferics. From this, we infer that the sub-pulses are produced by transient spark-like discharges embedded within the negative streamer system, the conducting tips of which would initiate relativistic electron avalanches, whose further development is facilitated by the enhanced E field ahead of and beyond the streamer front. In other instances, TGFs appear to be initiated during brief episodes of accelerated-speed FNB.

Although obtained for downward negative breakdown of –CG flashes, the results are expected to apply equally well to negative breakdown at the beginning of upward IC flashes, for which the initial breakdown pulse activity is fundamentally the same as for downward CG flashes. Together, the results establish that downward TGFs of –CG flashes and satellite-detected upward TGFs of IC flashes are variants of the same phenomenon, and are produced during fast negative breakdown early in the developing negative leader stage of CG and IC flashes.

2 Results

2.1 Observations

Figure 1 shows the layout of the Telescope Array Surface Detector (TASD) and the Lightning Mapping Array (LMA) used in both the earlier and present studies. The VHF interferometer (INTF) and fast electric field change antenna (FA) were located 6 km east of the TASD, and utilized three receiving antennas with 106–121 m baselines oriented to maximize angular resolution over the TASD (see Methods Appendix A1).

On August 2, 2018, two small, localized storms occurred over the TASD that produced three TGFs relatively close (17 km) to the INTF. The first TGF-producing discharge occurred at 14:17:20 UT and was a −CG flash that generated two TASD triggers $\simeq$1 ms after it began. The flash was initiated at $\simeq$5.5 km MSL altitude by a moderately high-power (+28 dBW, 630 W) upward fast positive narrow bipolar event (Supporting Figure S6). The ensuing downward negative breakdown went to ground in $\simeq$8 ms, corresponding to a stepped leader speed of $\simeq 5\times 10^5$ m/s, somewhat faster than the normal stepped leader speeds of 1–2$\times 10^5$ m/s. The two triggers recorded three gamma-ray bursts, jointly called TGF A, when the breakdown was at $\simeq$ 4.5 km MSL altitude (3.1 km above ground level).

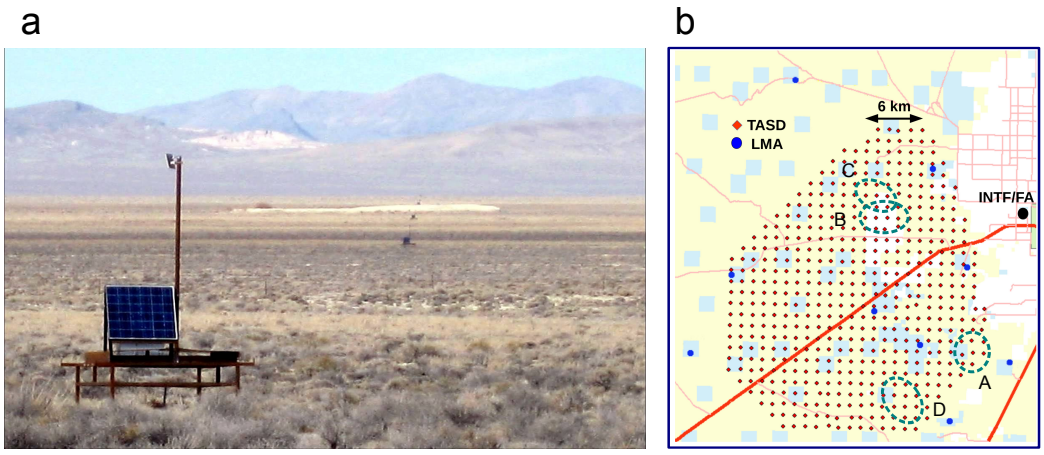

Figure 1. Telescope Array Surface Detector. (**a**) View of a close and distant surface detector stations on the desert plain west of Delta, Utah. Each detector unit consists of two 3 m^2 by 1.2 cm thick scintillator planes separated by a 0.1 cm steel sheet (Abu-Zayyad et al., 2013). Photo by M. Fukushima. (**b**) Map of the TASD stations, showing the locations of TGFs A–D (dashed ellipses). A total of 512 surface detectors have been deployed over a 700 km^2 area on a 1.2 km grid since 2008. A nine-station 3-D lightning mapping array (LMA) has been operated at the TASD since 2013 (blue dots). In July 2018, a VHF interferometer (INTF) and fast electric field sferic sensor (FA) were deployed 6 km east of the TASD, only a few days prior to observing the TGFs reported here.

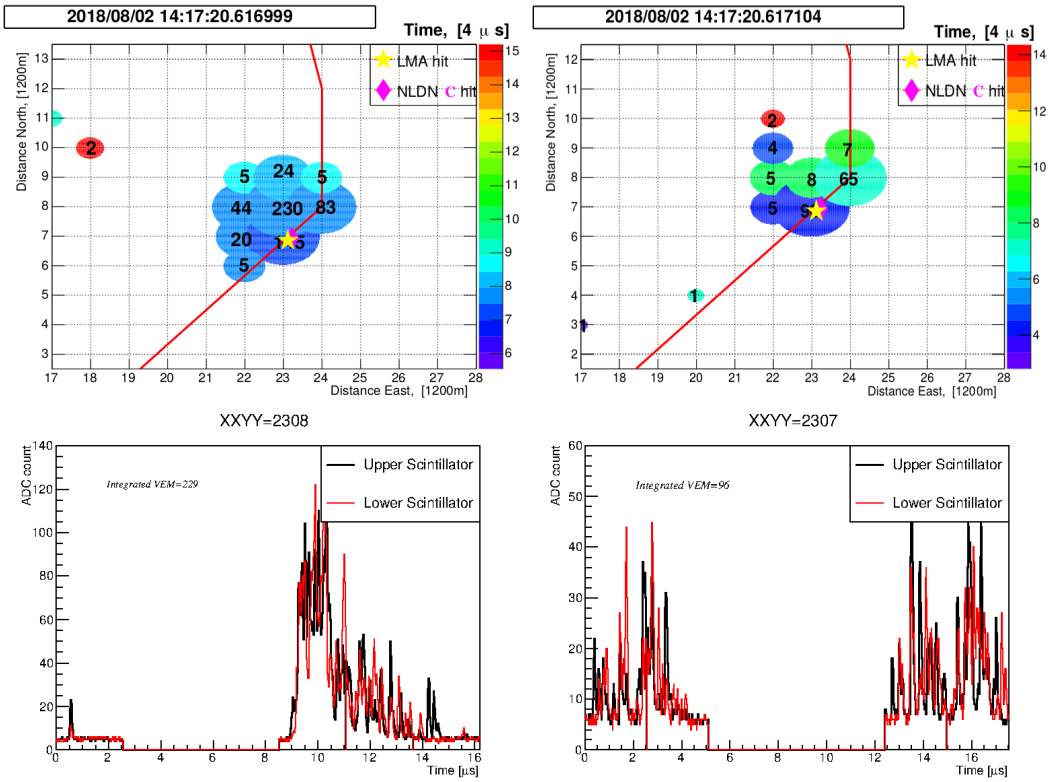

Figure 2. TASD observations of TGF A. *Top left and right*: Surface scintillator "footprints" for the three gamma-ray showers of TGF A. The grid spacing is in units of 1.2 km. The area of each circle is proportional to the logarithm of the energy deposit, and color indicates timing in 4 μs steps relative to the event trigger, corresponding to the approximate onset time of the gamma events at the ground. The yellow star shows the LMA-estimated plan location of the TGF, and is in close agreement with the location of its sferic by the National Lightning Detector Network (NLDN, underlying magenta diamond) making it difficult to distinguish between the two. The red lines denote the boundary of the TASD array, showing that a portion of both showers was likely undetected. *Bottom left and right*: Scintillator responses of the surface detector stations having the largest energy deposit during each of the gamma-ray showers. The upper scintillator is represented by black traces and the lower scintillator by red traces. A single Vertical Equivalent Muon (VEM), or about 2 MeV of energy deposit, corresponds roughly to a pulse 30 ADC counts above background with 100 ns FWHM on these plots. The horizontal time axes are relative to the detectors' individual triggers (different from the overall 'event' trigger, see Appendix A1).

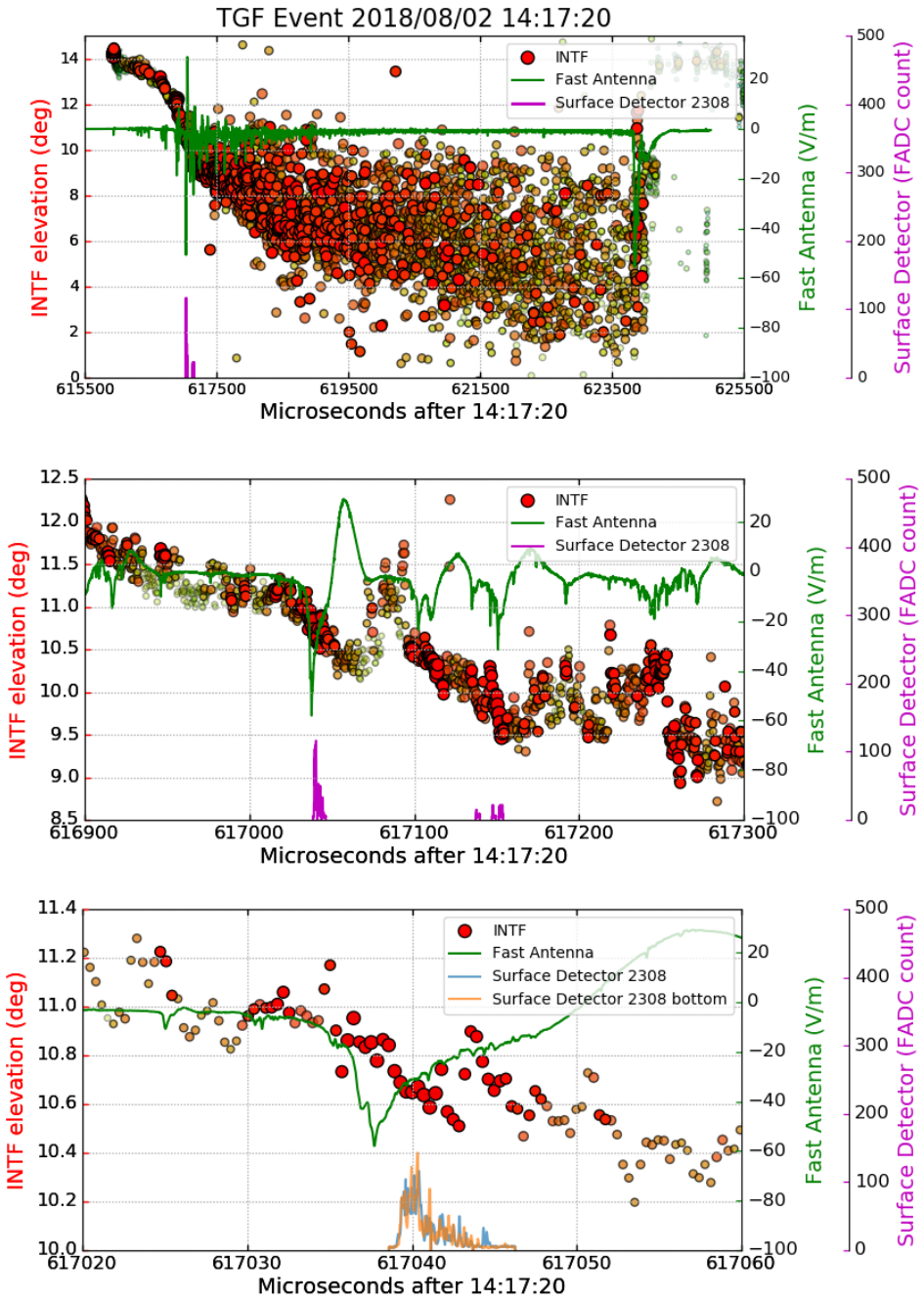

Figure 3. INTF and FA observations of TGF A. Panels show interferometer elevation versus time (circled dots, sized and colored by power), fast electric field sferic waveform (green waveform) and TASD particle surface detections (vertical purple bars). *Top:* Observations from initial breakdown through time of –38.3 kA initial cloud-to-ground stroke. Initial TGF detection occurred in coincidence with the strongest (–36.7 kA) sferic pulse, 326 μs after flash start (Supporting Table S1). *Middle:* 400 μs of observations around the time of the three gamma-ray showers of the flash, showing their correlation with the two largest amplitude initial breakdown pulses (IBPs) and episodes of fast downward negative breakdown (FNB). TASD footprints for the showers are shown in Figure 2. *Bottom:* Detailed 40 μs view of the upper and lower scintillator responses (blue and orange traces) relative to the IBP sferic and the downward FNB.

Figure 2 shows "footprints" of the TA surface detections for each of the two triggered events, along with the corresponding set of scintillator observations at a central SD station. The triggers occurred within ≃100 μs of each other, in the southeastern corner of the TASD. The observations are similar to those reported in our previous study (Abbasi et al., 2018), in that they consisted of gamma bursts typically 10 μs or less in duration and were detected at 9–12 adjacent SDs, over areas ≃3–4 km in diameter. The initial burst was the most energetic, depositing an integrated total of 230 Vertical Equivalent Muons (VEM) (471 MeV) in the nearby TASD station, and a total of 561 VEM (1,150 MeV) over all nine adjacent stations (see Supporting Table S1).

INTF and FA observations for the flash are presented in Figure 3, which shows how the bursts were related to the discharge processes. The top panel provides an overview of the first 10 ms of the flash, from the start of the downward negative leader through the initial stroke to ground. The gamma bursts (vertical purple bars) occurred early in the flash, ≃1.0 and 1.1 ms after the flash's initiation. Around this time, the FA data show a sequence of initial breakdown pulses (IBPs) of rapidly increasing and then decaying amplitude — typical of the beginning of –CG flashes.

The first 1,150 MeV burst was associated with a particularly strong (−38 kA) IBP sferic, comparable in magnitude to the sferic of the ensuing return stroke, which had an NLDN-detected peak current of −37 kA. The second TGF was less strong (192 total VEM, or 393 MeV) and was associated with the next-strongest IBP sferic (middle panel). Both gamma bursts were associated with episodes of accelerated downward negative breakdown.

The bottom panel of Figure 3 shows in detail how the initial gamma burst was related to the VHF radiation and sferic waveform, during a 40 μs window around the time of the burst. From the INTF elevation angles and the LMA-indicated 17 km plan distance to the source location, the VHF radiation sources descended ≃150 m in 10 μs, corresponding to an average propagation speed $v \simeq 1.5 \times 10^7$ m/s. By coincidence, this is the same as the extent and speed of the upward fast positive NBE breakdown at the beginning of the flash (also ≃150 m in 10 μs), and is indicative of the downward activity being caused by analogous fast negative breakdown (FNB) (Tilles et al., 2019). The gamma burst occurred partway through the fast downward breakdown, ≃1–2 μs after the peak of the negative sferic, and continued for about 5 μs before dying out shortly after the end of the FNB.

2.2 Source determination and time shifting

Figure 4 shows observations of the strongest gamma-ray event for each of the TGF-producing flashes, along with time-shifted scintillator detections for each participating TASD station. The vertical line for each flash serves as a reference time for comparing the different SD waveforms with each other and with the INTF/FA. As described below, it corresponds to the median onset time at the different SD stations. Similarly, the horizontal line indicates the elevation angle corresponding to the median source altitude immediately around that time.

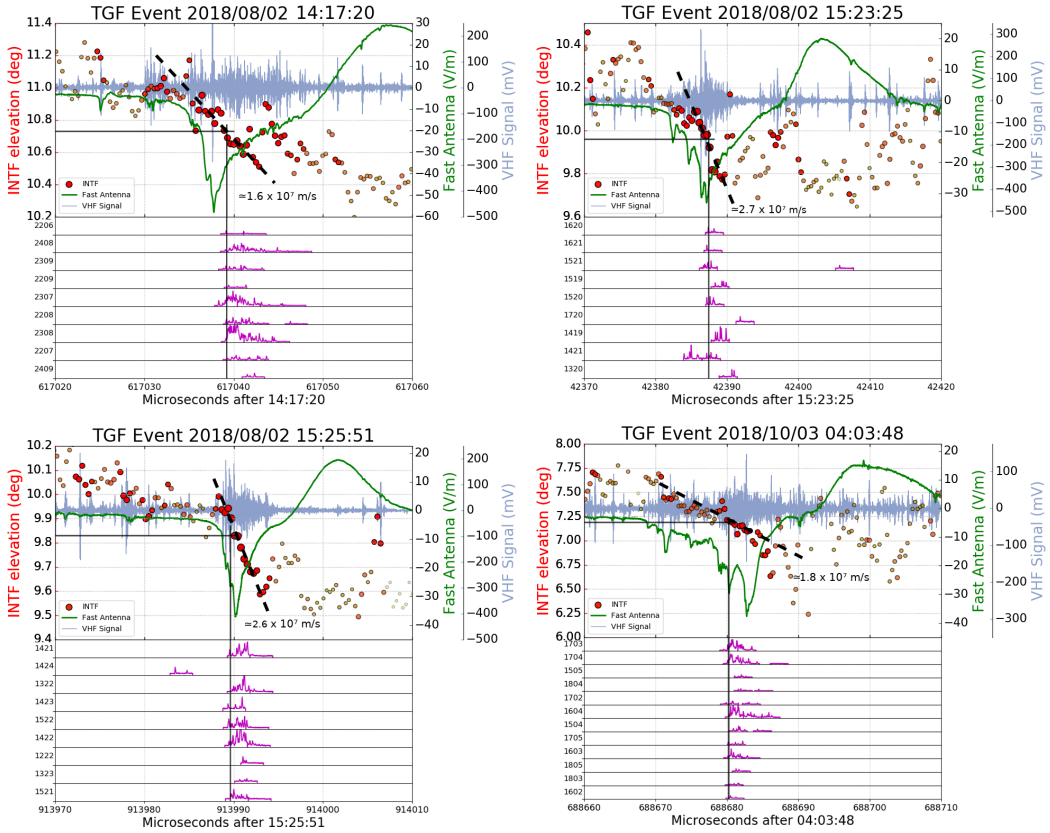

Figure 4. Detailed comparative observations. Time-shifted surface detector data for the primary gamma-ray event during each of the four TGF-producing flashes, showing how the TASD detections (lower axes) compare to each other, and their relation to the VHF radiation sources and fast electric field sferics (upper axis) of the developing discharges. Black vertical and horizontal lines in each panel show the median onset time of the gamma burst(s) during the downward FNB, obtained from analysis of the collective onset times t_b at the different TASD stations and the observed INTF elevation angle vs. time (see Section 2.2). Light blue traces show the VHF time series waveform observed by the INTF. Station numbers XXYY in the lower axes identify each TASD's easterly (XX) and northerly (YY) location within the array in 1.2 km grid spacing units. FNB propagation speeds are indicated by the dashed lines and associated values. Full-page versions of these plots are given as Figs. S15–S18. in the Supporting Information

The coordinate system for comparing the TASD observations with the INTF and FA data is shown in Figure A1a of the Appendix. It is a source-centric system in which the plan position on the ground beneath the TGF serves as the coordinate origin. To shift the scintillator detection times, we need to know the slant ranges r and R from the TGF source to the SD and from the source to the INTF. The x, y plan location of the source is obtained from the LMA observations within ± 1 ms of the TGF, which determines the plan distances D and d to the INTF and to each TASD station. The TGF is therefore at point $a = [0,0,z_a]$ in the coordinate system, where z_a is the altitude of the source above a reference plane of 1400 m MSL. A generic TASD station is at point b, typically within $\simeq$1–3 km plan distance of the TGF. The INTF/FA is at point c, typically 15–25 km plan distance from the TGFs. The net time shift Δt between the surface detector data at a given TASD station and the INTF is given by the difference in propagation delays. In particular, $\Delta t = (R/c) - (r/c) = (R - r)/c$. Because the plan distances are known, the slant ranges and hence time shifts Δt are functions only of z_a. Once z_a is determined, the time shifts are calculated for each TASD individually and used to compare the different TASD waveforms a) with each other, and b) with the FA sferic and the VHF source activity and centroid observations, as seen in Figure 4. For each TASD station, the onset time at the INTF is given by $t_c = t_b + \Delta_t$, where t_b is the onset time at the TASD in question. As mentioned above, the vertical line in Figure 4 corresponds to the median of the onset times at the different stations. At the same time it also serves as a reference point for identifying stations having onset times that differ from the median value.

Because the LMA typically mislocates non-impulsive, VHF-noisy sources, the TGF's altitude is determined from the INTF elevation angles θ_c. The difficulty with doing this is that the angle changes with time during the IBP, namely $\theta_c = \theta_c(t_c)$, making it unclear which time to pick. Even though the elevation change corresponds only to a $\simeq$100–200 m spread in the source altitude, it corresponds to the full 10–20 μs duration of the VHF and FA sferic observations. The ambiguity is resolved by recognizing that two independent measurements are necessary to determine the two unknowns, namely the source altitude z_a and time t_a. In addition to the INTF elevation angle θ_c, the second measurement comes from onset time t_b at the particular TASD in question. Although this provides enough information to obtain the solution, the different variables of the problem, namely [θ_c, t_c, z_a, t_a], wind up depending upon each other, requiring an iterative approach to obtain the solution.

Figure S14 shows a block diagram of the iteration process. For each TASD the onset time t_b is used along with an initial value of z_a to determine the corresponding onset time t_c at the INTF. The INTF data relating t_c and θ_c is then used to determine the corresponding source altitude z_a and time t_a. If the resulting z_a is different from the initially assumed value, the new value is used as the starting altitude for the next step. The iteration is stable and convergence is reached within a couple of steps. The process is repeated for each of the participating TASDs to obtain a set of z_a, t_a, t_c, and θ_c values, from which the median is determined. Table S2 lists the full set of solutions for each TASD of the different TGFs. The median t_c and θ_c values are shown in bold and correspond to the vertical and horizontal lines in Figure 4. For TGFs A, C and D, the participating TASDs all have similar onset times. The exception is TGF B, which has two or more onset times, as discussed in the next section. An analogous but somewhat different method of time-shifting and comparing the TASD and INTF/FA observations, developed independently during the course of the study, is described in Appendix A2 and shown in the Supporting Figures. The approach utilized measurements at two TASD stations having the strongest detections to determine the time shifts for the other TASDs and alignment with the INTF/FA observations, and provided an alternative way of investigating the observations.

2.3 Temporal comparisons

The above analyses provide accurately-determined estimates of i) each TGF's plan location x_a, y_a, altitude z_a, and time t_a, ii) the onset times t_c of the gamma events during the IBP, and iii) the INTF elevation angle θ_c corresponding to t_c and z_a. The t_c and θ_c values are shown by the vertical and horizontal lines in each of the panels of Figure 4. We re-emphasize the fact that the t_c values serve as reference times for comparing the different TASD detections with each other. For TGFs A, C, and D, most or all of the stations detected the onset at the same time. The onset times are well-identified by the analysis technique and are indicative of the TGFs in question all having a single onset. An important exception is TGF B, for which TASD 1421 had a noticeably earlier onset time. Three other stations (1519, 1419, and 1320) appeared to have slightly delayed onsets. As discussed below, the different apparent onsets are notable because the footprint of the stations involved were systematically displaced in a fully 360 degree circular pattern around a central hole. The observations are also illustrative of the comparisons being able to identify multiple onset times.

For each of the four flashes, the gamma bursts were associated with well-defined episodes of downward-propagating fast negative breakdown. The average propagation speeds during the episodes ranged from $\simeq$1.6 to 2.7 $\times 10^7$ m/s (slanted dashed lines in each panel of Figure 4). This is compared to average speeds of $\simeq$1.0 to 2.5$\times 10^6$ m/s for the breakdown immediately preceding the IBPs and TGFs (Figure 3 and Supporting Figures S7–S9). The sferics associated with the TGFs constituted the strongest initial breakdown pulses of the flashes. Whereas the onset time of the gamma burst of TGF A (Figure 4a) occurred slightly after the main peak of the IBP sferic, the bursts during other flashes occurred during or at various times prior to the peak. For TGF C, the onset was at or shortly after the beginning of the IBP and FNB, while for TGF B, the primary onset was closely correlated with the main IBP peak. For TGF D, the onset appeared to be exclusively correlated with a strong, leading-edge sub-pulse during the IBP's FNB. IBPs having such sub-pulses are called "classic" IBPs (Karunarathne et al., 2014; Marshall et al., 2013; Nag et al., 2009; D. Shi et al., 2019). The sub-pulse feature of the preliminary breakdown has long been recognized, beginning with Weidman and Krider (1979), but the cause both of IBPs and their sub-pulses has remained unknown. The present results show that the IBPs are produced by fast negative breakdown, and that the sub-pulses are capable of initiating gamma bursts.

For TGF A at 14:17:20 (Figures 4a and 5a), the scintillator detections in Figure 3 are from TASD 2308, corresponding to the station having the most energetic footprint. However, the estimated plan location of the burst from the LMA observations, as well as the NLDN location for the sferic associated with the burst, indicate the breakdown was almost directly above TASD 2307, 1.2 km to the south and 17 km southwest of the INTF (Supp. Figs. S1 and S10e). The energy deposit in TASD 2307 was slightly weaker than that in 2308 (145 vs. 230 VEM), indicating that the gamma burst was tilted slightly northward from vertical. A significant feature of the observations in Figure 4a is that the apparent onset time of the burst coincided with a step discontinuity in the VHF elevation centroid values. We later show (Figure A1b) that the discontinuity was due to a brief interval of enhanced propagation speed, in which the FNB descended $\simeq$50 m in 1.5 μs, corresponding to a speed $v \simeq 3 \times 10^7$ m/s, two times faster than the average speed of the IBP's FNB. Observations of the second set of gamma bursts during the flash shows them to be similarly associated with brief episodes of enhanced fast breakdown speeds ($\simeq 2.3 \times 10^7$ and 4.6×10^7 m/s; Supp. Fig. S10d,g).

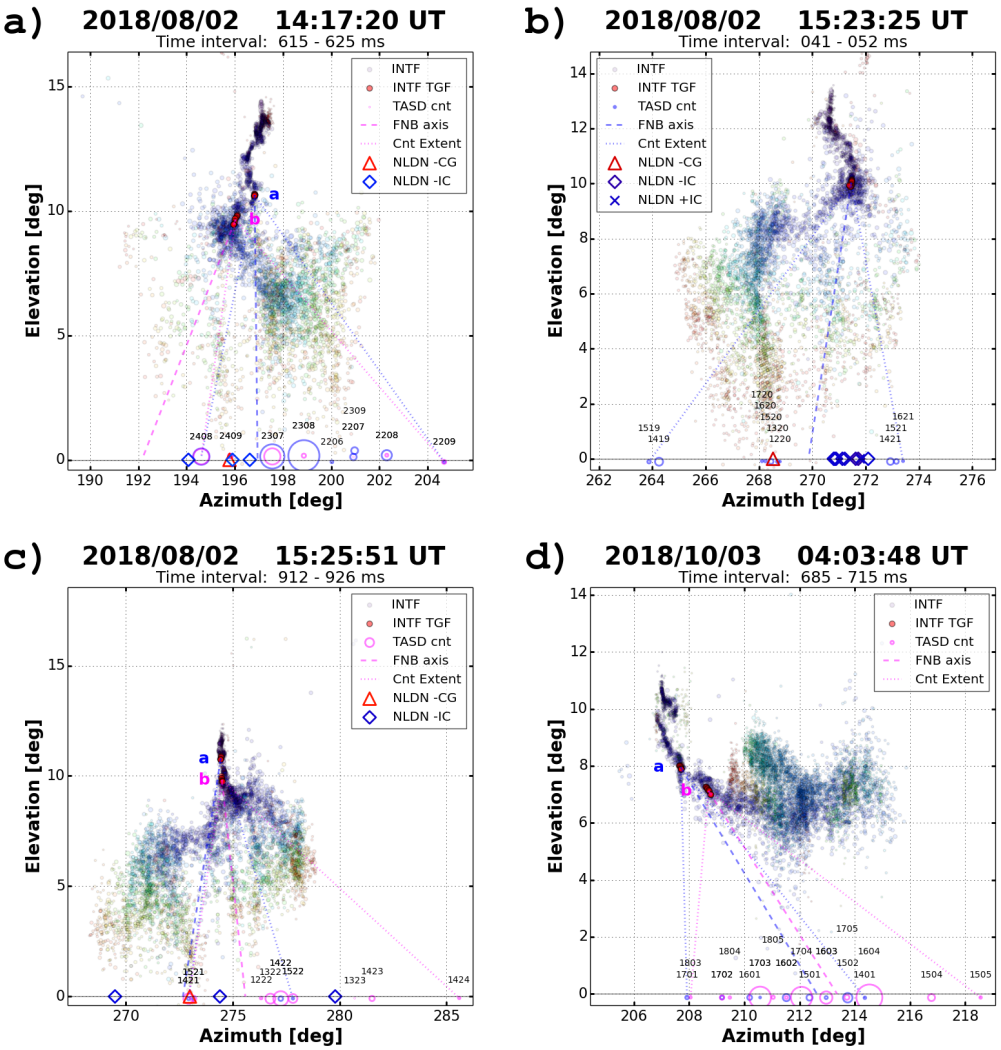

Figure 5. INTF observations of the TGF-producing flashes. Azimuth-elevation plots of INTF observations for the parent flashes of TGFs A–D, showing the initial downward development leading to the TGF occurrences (dark red sources and a,b labels, indicating the TGF altitudes). Continuation of VHF activity is shown up to the time of the initial stroke to ground for –CG flashes A,B,C, and for a comparable time during the low-altitude intracloud flash of TGF D. Dashed lines indicate the directions of the FNB associated with each TGF, and the inferred possible beaming direction. Baseline circles indicate detected TGF strength (VEM counts) and azimuthal directions of participating TASDs. Dotted line pairs indicate maximum angular spread (labelled 'Cnt Extent') of the SD detections, as viewed in the transverse plane from the INTF site. Vertical/horizontal aspect ratios are adjusted to show true angular extent. TGF B appeared to have multiple onset times at the different TASDs, and therefore narrower beaming than indicated by the overall angular extent. Baseline symbols show NLDN locations of CG and IC events. Full page versions of each panel are given in Figures S19-S22 of the Supporting Information

TGFs B and C (Figures 4b,c and 5b,c) occurred in a later storm over the north-central part of the TASD, but at the same plan distances (16–17 km) from the INTF. Both were relatively weak in comparison with TGF A, with total surface detections of 112 and 212 VEM, respectively (Supp. Table S1 and Figs. S2 and S3). The parent flash of TGF B was similar to that of TGF A in terms of its initiation altitude ($\simeq$3.9 km AGL, 5.3 km MSL) and average leader speed (1.5×10^6 m/s). The gamma bursts began 0.65 ms after flash start, again during the strongest initial breakdown pulse of the flash, whose peak current was as strong as that of TGF A (–30 kA). However, instead of the SD waveforms having a common onset time, as for TGF A, the onset times varied noticeably at different sets of TASDs. In addition, the overall footprint of the TGF was annular-shaped around a central hole (Supp. Fig. S2). The LMA and NLDN observations indicate the burst's source was over the western side of the footprint, adjacent to the hole. The initial burst was detected only at a single station, SD 1421 immediately northeast of the source. The primary onset occurred 2–3 μs later, and was detected at four adjacent stations 2–3 km to the east on the opposite side of the hole (SDs 1521, 1520, and 1621, 1620). This was followed by the two southern stations having an additionally delayed onset (SDs 1519 and 1419), and finally a fourth onset back at the western-most station, almost directly below the source (SD 1720).

Concerning the correlation with the INTF and FA data for TGF B, the early gamma-ray detection at TASD 1421 coincided with a prominent sub-pulse of the IBP, and represents a separate onset time. The sub-pulse occurred during an apparently brief interlude of upward rather than downward development of the VHF radiation sources. Subsequently, the gamma-ray activity occurred during downward fast negative breakdown having a propagation speed of 2.7×10^7 m/s, with the primary onset time coinciding with the main sferic peak. Less than a microsecond after the peak, the elevation centroids exhibited a 20–30 m step discontinuity similar to that seen during TGF A, which appeared to initiate the bursts detected at the southern TASDs.

The parent flash of TGF C occurred 2.5 minutes later in essentially the same location as TGF B, and produced two gamma bursts 117 μs apart in time, similar to TGF A. In contrast with TGF B, both bursts were relatively simple and provide canonical examples of the basic processes of TGF production. For each event the gamma radiation was downward-directed and detected immediately below and north of the source (Supp. Figs. S3 and S12). The first event was weaker and produced a total of 35 VEM (72 MeV) at four adjacent TASDs below the source. Figure 4c focuses on the second event, which was stronger and produced a total of 212 VEM (434 MeV) at nine adjacent stations below the source. As seen in Figures 4c and S12d, the parent IBP was temporally isolated from preceding and subsequent activity, and a sudden increase of the VHF radiation signaled the onset of downward negative breakdown and the IBP sferic. The breakdown descended $\simeq$120 m in 4.7 μs at a steady rate 2.6×10^7 m/s, indicative of FNB. In this simple case, the gamma radiation began immediately after the start of the FNB and continued with varying but generally increasing intensity through the entire descent until the breakdown ceased. In the process, several unresolved sub-pulses occurred, similar to the sub-pulses of TGF A. Also seen in other IBPs but more clearly shown in this flash, onset of the FNB was immediately preceded by brief upward-developing VHF sources, indicative of characteristic FPB breakdown that appeared to trigger the downward FNB.

TGF D (Figures 4d and 5d) occurred during a nocturnal storm on October 3 in a similar southward direction as TGF A, but further to the south at 24 km plan distance over the southeastern corner of the TASD (Supp. Fig. S4 and S13). Again, the flash produced two triggers, the first of which contained three weak gamma bursts that were partially outside the southern boundary. The second trigger and burst occurred 140 μs later, $\simeq$800 μs after the flash start. Its footprint was shifted about 2 km northward from that of the first burst, placing it entirely inside the TASD. The apparent source of the bursts was on the eastern part of the overlapping region between the two footprints (Supp. Fig.

S13e). The first burst was therefore beamed southwestward from its source and the second burst was beamed northwestward. The westward component of the beaming is clearly evident in the INTF observations of Figure 5, which showed an increasingly strong WNW-ward tilt of the azimuthal locations as the breakdown descended, with the tilt angle becoming as large as 45° from vertical by the time of the gamma burst. A total of 440 VEM (962 MeV) was detected at 12 stations during the second burst, compared to a partial total of 100 VEM (205 MeV) at 9 stations during the first burst.

Concerning the second trigger and main burst of TGF D, the IBP of the burst had a complex, relatively long-duration (15 μs) sferic waveform that was accompanied by steady downward development of the VHF radiation sources. Overall, the breakdown descended $\simeq$240 m in 13.4 μs at an average rate of 1.8×10^7 m/s. The gamma burst was initiated partway through the descent, coincident with a major sub-pulse and the onset of increased VHF radiation. The sequence of events is similar to that of TGF C in that the radiation increase and corresponding sub-pulse was preceded by a brief interval of fast upward positive breakdown. The ensuing fast downward activity exhibited a small step discontinuity in the VHF centroids that coincided with the onset of the gamma burst and sub-pulse. As in each of the other TGF flashes, the gamma radiation continued up until the approximate end of the FNB, shortly after the main negative peak of the IBP sferic.

3 Discussion

3.1 Observational Results

The results of this study demonstrate that TGFs are produced during strong initial breakdown pulses (IBPs) in the beginning stages of negative-polarity breakdown. This is shown with a high degree of temporal and spatial resolution provided by a unique combination of a state-of-the-art cosmic-ray facility, coupled with high-quality VHF and LF sferic observations of the parent lightning discharges. In addition to showing how TGFs are related to IBPs, the observations reveal how the initial breakdown pulses themselves are produced, which has remained unknown for over 50 years. In particular, IBPs are produced by a recently-identified type of discharge process called fast negative breakdown (FNB) (Tilles et al., 2019). FNB is the negative-polarity analog of fast positive breakdown that has been identified as the cause of high-power narrow bipolar events (NBEs), and which is instrumental in initiating lightning (Rison et al., 2016). Both polarities of fast breakdown propagate at speeds around 1/10 the speed of light, with FPB sometimes reaching $(1/3)c$. FPB is understood to be produced by a system of propagating positive streamers that, when occurring at the beginning of a flash, is initiated by corona from ice hydrometeors in a locally strong electric field region inside storms (Rison et al. (2016); Attanasio et al. (2019)).

Although the nature of fast negative breakdown is uncertain (Tilles et al., 2019), its similarities with FPB strongly suggest that FNB is also streamer-based, except for being of negative polarity. Independent of polarity or direction, both positive and negative fast streamer systems would significantly enhance the ambient electric field ahead of their advancing front (Attanasio et al., 2019), facilitating the development of high energy electron avalanches necessary for gamma-ray production.

Owing to its simplicity, TGF C provides a canonical example of the basic processes involved during an IBP. In particular, the IBP of TGF C was initiated by a brief (1–2 μs) interval of fast upward positive breakdown, immediately followed by a sudden increase in the VHF radiation and the onset of oppositely-directed downward FNB (Figures 4c and S8). The positive breakdown began slightly beyond the lowest extent of the preceding negative breakdown and propagated weakly but rapidly back into preceding activity, whereupon it initiated oppositely-directed and VHF-strong FNB back down and beyond the path of the upward FPB, extending the negative breakdown to lower altitude

(see also Fig. S12d,g). Similar sequences of upward positive/downward negative breakdown were associated with TGF-producing IBPs of the other flashes, including a preceding, weaker gamma-ray event of TGF C (Fig. S12c,f).

The TGF observations show that the onset of the electron avalanching and gamma-ray production occurred at various stages during the IBPs. For TGF A, the onset occurred after the sferic peak, but during still-continuing FNB. TGF C occurred at or shortly after the beginning of its IBP and FNB onset. For the more complex discharges of TGFs B and D, the onset was often associated with leading-edge sub-pulses that are a characteristic feature of classic IBPs (Weidman & Krider, 1979; Nag et al., 2009; Karunarathne et al., 2014). Like IBPs, the nature and cause of sub-pulses has continued to be a mystery (e.g., da Silva and Pasko (2015); Stolzenburg et al. (2016)). The results of the present study show that the main driving force of the IBPs is fast negative breakdown, which has the sub-pulses as embedded components. Basically, the sub-pulses are indicative of repeated breakdown events within the developing IBP discharge. The observation that TGFs are often associated with sub-pulses, and that this occurs during fast negative streamer breakdown, provides a possible explanation for the sub-pulses' occurrence. Namely, that they are produced by spark-like transient conducting events (TCEs) embedded within the negative streamer system. That the events are spark-like is indicated by the pointed, cusp-like nature of their sferics, evidence of a sudden current onset and rapid turnoff, and also by the sub-pulses repeating several times as the IBP progresses. It should be noted that the final peak of the overall IBP sferic is also cusp-like, indicating that it too is produced by a spark-like sub-pulse.

Once initiated, the gamma radiation typically lasts $\simeq$3 to 5 μs for the flashes of this study. GEANT4 simulations presented in Figure S24 of the Supporting Information show that multipath Compton scattering does not artificially extend the duration, as 95% of detectable particles produced by 10 MeV (100 MeV) photons at 3 km AGL will arrive within 20 ns (60 ns). The total energy available for deposit after the first 100 ns is small enough to be indistinguishable from background levels, thus the observed durations reflect the intrinsic duration of the sources. An important implication of this result is that relativistic avalanching lasting 3–5 μs would propagate a distance of $\simeq$1–1.5 km, substantially beyond the 100–200 m extent of the FNB and IBP. This would provide the electron avalanches with additional amounts of electric potential energy until the ambient electric field drops below the threshold for avalanche propagation ($\simeq 2\times10^5$ V/m) (Dwyer, 2003).

Before proceeding, we emphasize the fact that the TASD is detecting multi-MeV gamma radiation from the lightning discharges, and not lower energy x-radiation. We repeat here the simple arguments for this, presented by Abbasi et al. (2018) and based on the well-understood physics of Compton electron production and the well-calibrated TASD response to minimum-ionizing charged particles. In particular, TASD responses for the events of the present and earlier studies (e.g. Supplemental Figure S3) can clearly be resolved into individual minimum-ionizing Compton electrons that result in the deposit of approximately 2.4 MeV into either the upper or lower scintillator plane, or in correlated deposits into both planes. A property of particles above the minimum-ionization threshold is that higher-energy particles would still deposit only 2.4 MeV per plane (Zyla et al., 2020). Thus, the TASD cannot determine the maximum energy of Compton electrons, but it can place a lower limit on the energy values. Compton electrons that deposit 2.4 MeV into one plane are produced by a photon with no less than 2.6 MeV (Supplemental Figure S9 of Abbasi 2018). Electrons that deposit 2.4 MeV into both planes, and also traverse the 1 mm steel separating sheet, have a total energy loss of 6.2 MeV and must be produced by photons with a minimum energy of 6.4 MeV.

The above inferred photon energies should be interpreted as minimal values, as they assume that the Compton electrons are produced by head-on collisions in which the gamma ray is backscattered and transfers the maximum amount of energy to the electron. The

likely contributions of grazing incidence collisions to our signal would imply the actual photon energies are several times higher, depending on the grazing angle (Supplemental Figure S10 of Abbasi et al. (2018)). Even for single-scintillator layer detections, these are comparable to the average 7–8 MeV energy of relativistic runaway spectra detected by satellites. In any case, there is no question that the TASDs are detecting multi-MeV gamma-rays.

3.2 Extension to intracloud flashes

Although obtained for downward negative breakdown at the beginning of –CG and low-altitude IC flashes, the results apply equally well to upward negative breakdown at the beginning of normal-polarity IC flashes at higher altitudes in storms. Figure 6 compares INTF and FA observations of the –CG flash of TGF C with those of an IC flash that was the next lightning discharge in the storm (see Figs. S27–S29 for additional observations of the flashes). The top two panels show 2 ms of data for the two flashes with time scales of 500 μs/division. The bottom panel shows an expanded view of the large-amplitude classic IBP near the end of the IC interval. Taken together, the plots illustrate the differences and similarities of the initial breakdown processes of IC and –CG flashes. In particular, and as has long been known (e.g., Kitagawa and Brook, 1960; Weidman and Krider, 1979), the downward negative breakdown of –CG flashes intensifies more rapidly and continuously than the negative breakdown of upward IC flashes. The difference is clearly seen in the top two panels and is due to a combination of effects: first, the IC flashes needing to propagate through a relatively large vertical extent of quasi-neutral charge before reaching upper positive storm charge, compared with little or no spacing of the lower positive charge during –CG flashes (e.g., Fig. 1 of Krehbiel et al. (2008), and Fig. 3 of da Silva and Pasko (2015)), and secondly the IC discharges occurring at reduced pressure. The overall result is that IC flashes develop more intermittently and with longer stepping lengths than –CG flashes (e.g., Edens, 2014).

Despite the intensification differences, individual initial breakdown pulses of IC flashes exhibit the same features as those of –CG flashes. In both instances, classic IBP sferics consist of an initial strong electric field change having embedded sub-pulses, followed by a characteristically large and relatively slow opposite-polarity field change. The similarity is illustrated by comparing an expanded plot (bottom panel of Figure 6) of the large-amplitude IBP at the end of the middle panel with that of TGF B seen in Figures 4b and S16, which occurred in the same storm $\simeq$4 min earlier, three flashes before the IC flash. Except for polarity, the sferics are virtually identical. More importantly, the INTF data shows both are produced in the same manner, namely by fast negative breakdown. Owing to the increased stepping distance, IC IBPs tend to have longer durations than those of –CGs; lasting $\simeq$70 μs for the IC IBP vs. $\simeq$35 μs for the IBP of TGF B. The fast negative breakdown component of the IC IBPs is also similarly longer, being $\simeq$20 μs for the IC vs. $\simeq$10 μs for TGF B. The factor of two overall duration difference agrees with the study by Smith et al. (2018) of median durations of large IBP sferics in Florida storms. Another example of a similar classic IC IBP sferic is seen in Fig. 4 of the study of Florida IBPs by Marshall et al. (2013), which had a duration of $\simeq$100 μs and was considered to be a 'candidate' TGF flash. At this point it should be noted that in many instances the durations of IC and CG IBPs are the same for both types of flashes. This is seen in the scatter diagram of Figure 5 of Smith et al. (2018), and is shown in detail by the comprehensive observations of Tilles (2020). Figures 9.3 and 9.4 of the latter study, conducted in Florida with the same INTF and FA instrumentation as in the present Utah study, show that (except for polarity) the IC and –CG IBPs were essentially indistinguishable both in terms of their sferics and durations.

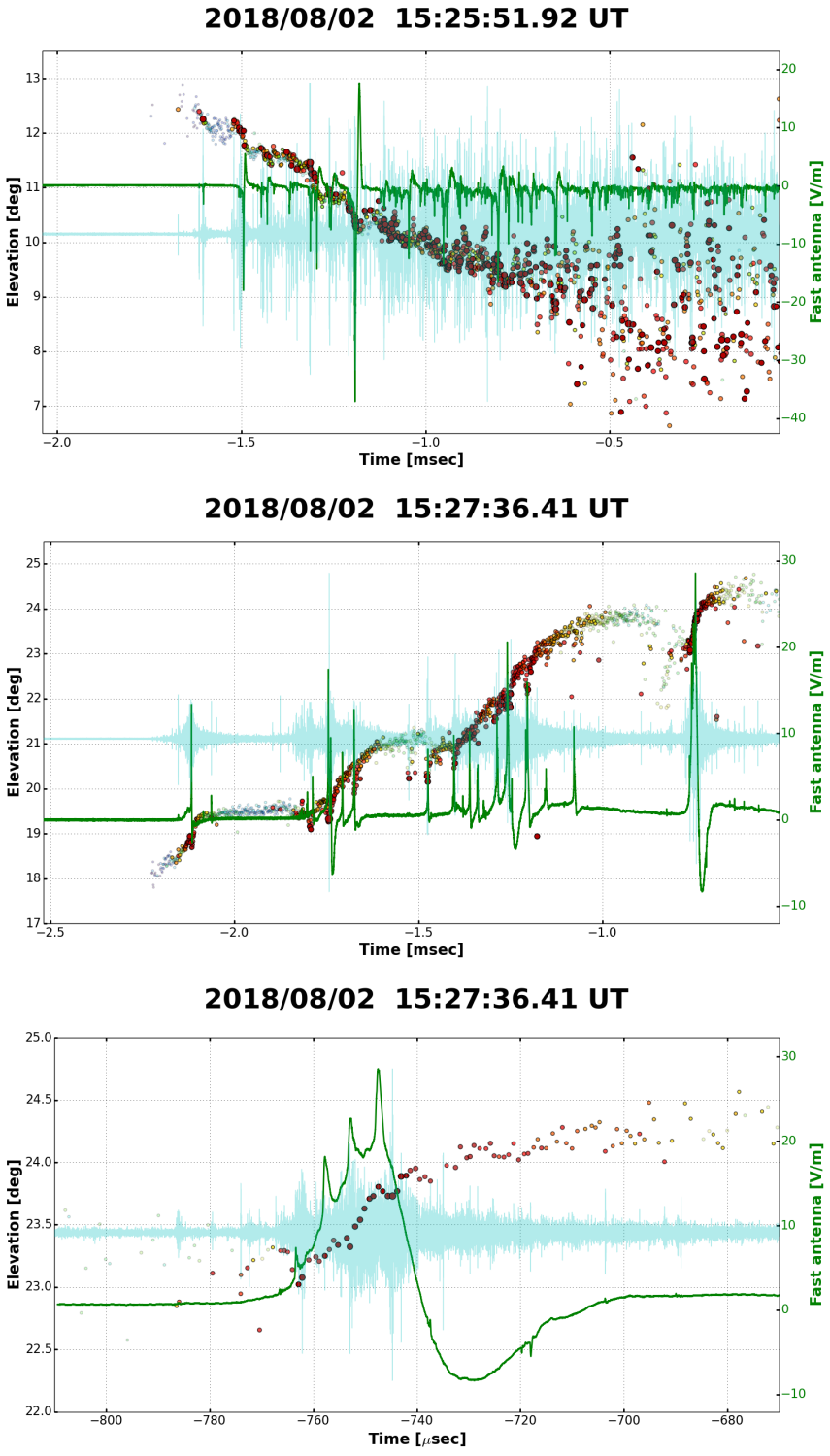

Figure 6. Comparison of the –CG flash that produced TGF C with the IC flash that was the next flash in the storm, illustrating the differences and similarities between the two types of flashes. Top two panels show 2 ms of observations for the downward –CG and upward IC. Bottom panel shows an expanded view of the large IBP near the end of the IC interval which, except for polarity and overall duration, is basically identical to the IBP that produced TGF B three flashes earlier in the storm. The propagation speed of the upward FNB is also similar, being $\simeq 1.5 \times 10^7$ m/s.

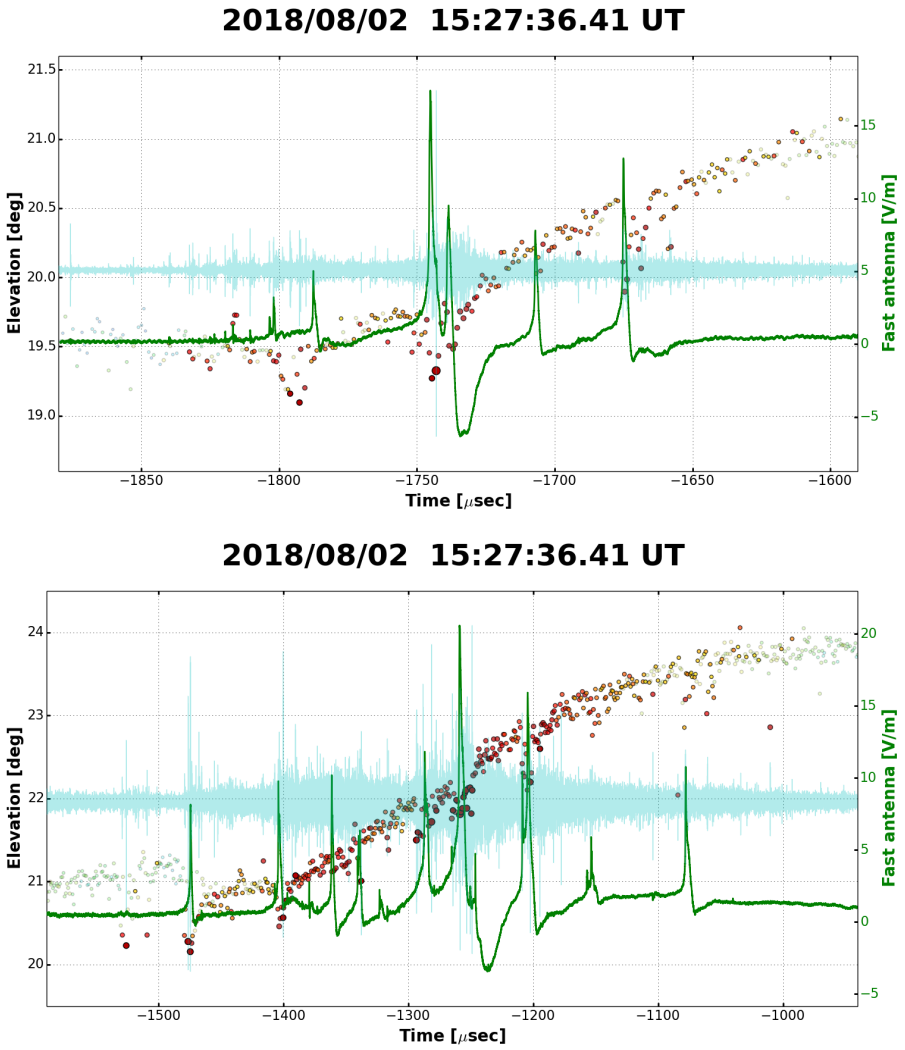

Figure 7. Expanded views of the complex IBP clusters of the IC flash of Figure 6, showing the increased number and highly-impulsive nature of the sub-pulses. The FNB breakdown of the IBPs and the sub-pulses are each embedded in continuous upward negative streamer breakdown having a propagation speed of $\simeq$2–3$\times10^6$ m/s, showing that negative streamer breakdown doesn't have to travel at speeds of 10^7 m/s to produce the sub-pulse sparks. The durations of the two clusters were $\simeq$130 and 400 μs, respectively, with the sferic of the first cluster resembling that of the TGF-producing IBP of Figs. 2 of Lyu et al. (2018); Pu et al. (2019), and the second cluster resembling the sferic of another complex TGF-producing sferic of Pu et al.

Due to the TGF-producing storms having low flashing rates (typically 1–2 min between flashes in the present study), the electrification is allowed to build up to large values, causing both the –CG and IC flashes to be highly energetic when they finally occur. For the IC flash of Figure 6, this is reflected not only in the amplitude and duration of the classic IBP, but also by the preceding activity being produced by two complex sequences (clusters) of IBPs and sub-pulses, seen in the middle panel. Each of the clusters is linked together by continuous, upward-developing high power negative breakdown, producing long-duration complex steps. The overall durations of the two clusters were ≃130 and 400 μs, respectively. Expanded views of the complex IBPs are seen in Figure 7, which show the sferics were dominated by increasing numbers of sub-pulses that assisted in continuing the negative breakdown and extending the cluster durations. In addition to their increased numbers, the sub-pulses are dramatically more impulsive and stronger in amplitude than those of the –CG flashes. The IC sub-pulses had amplitudes of ≃10–20 V/m, compared to ≃5–10 V/m for the sub-pulses (at essentially the same distances) of the TGF-producing IBPs of Figure 4 (seen in larger scale in Supporting Figs. S15–S18). Given that the simpler IBPs of the –CG flashes produced TGFs, the IC flash would likely have been equally or more capable of generating upward TGFs. Due to relativistic avalanching being a strong function of the potential difference being shorted out by the spark-like sub-pulses (Celestin et al., 2015), as well as the sub-pulses being more dynamic (Celestin et al., 2012) and repetitively impulsive, the resulting avalanching and TGFs would be more energetic, as well as longer lasting. Similar observations were obtained for an IC flash that occurred between TGFs B and C, which are compared with TGF B in Figs. S24–S26.

3.3 Implications for TGF production mechanisms

As summarized in the recent modeling study of TGFs by Mailyan et al. (2019), there are two classes of models for TGF production: First, what is termed the relativistic runaway electron avalanche (RREA) or relativistic feedback (RFD) model, in which electron avalanches develop in km-scale regions of strong electric fields in storms (Dwyer, 2003). In this model, the avalanching is enhanced by relativistic feedback that increases the avalanche currents by several orders of magnitude (Dwyer, 2012). The second class is broadly termed the 'leader' model, in which the relativistic avalanches are initiated in the highly concentrated electric field produced at the negative tip of a conducting leader channel. The electric field at the tip is extremely strong as a result of the leader having kilometer-scale extents and shorting out tens to a few hundred MV of potential difference in the storm. Whereas the RREA process by itself requires cosmic ray-produced or other seed relativistic electrons to get started, the leader process begins with low energy thermal electrons, and requires exceedingly large electric fields ($\simeq 3 \times 10^7$ V/m — an order of magnitude larger than the breakdown strength of air) to be accelerated into the runaway electron regime, where their number and energy increases exponentially with time and distance (e.g., Dwyer (2004)). Electric fields of this strength are produced only at the tips of conducting leader-type channels, and then only transiently during rapid channel development. Thermal electrons are accelerated into the relativistic regime as a result of transient negative streamers within the strong E region (the so-called 'negative corona flash'), as described by Moss et al. (2006), Celestin and Pasko (2011), and Celestin et al. (2015). Once the leader/streamer-initiated avalanches are started they would be able to initiate the relativistic feedback process.

While relativistic feedback can explain the large currents and fluxes of highly energetic satellite-detected events, it does not appear to be playing a role in initiating the smaller-scale observations of the present study. Instead, the inference that IBP sub-pulses are caused by spark-like transient discharges embedded within the fast negative streamer system points to the leader/streamer model as playing an important and possibly dominant role in generating runaway avalanches and TGFs. Once initiated, the runaway elec-

trons would additionally increase in energy while propagating through the enhanced field region ahead of and beyond the relatively broad streamer front (Attanasio et al., 2019).

An important question is whether the conducting channels of the sub-pulses (which we refer to as transient conducting events, or TCEs) are isolated within the negative streamer system and from each other, or if they are connected back into, or originate from, the conducting channel of the incoming negative leader. If so connected, the potential drop beyond the negative tip of the sub-pulse channel would be comparable to the amount shorted out by the km-long or longer leader, envisioned to be as large as 60 to 200 MV or more (e.g., Celestin et al. (2015); Mailyan et al. (2019)). Such a leader is termed a 'high potential' leader, which by itself can produce the large ($\simeq 10^{16}$–10^{18}) gamma photon fluxes inferred by satellite observations (Celestin et al., 2015).

To address the question of the sub-pulse connectivity, we note that the sub-pulses continue to occur until one suddenly causes the IBP sferic to begin transitioning to an opposite-polarity field change during the final part of the IBP. Although the flash current does not change direction, the electric field waveform becomes dominated by the electrostatic and induction components, which are inverted in polarity from the radiation component due to the flash being beyond the reversal distance d for vertical dipolar discharges, where $d = \sqrt{2}\,h$ and h is the discharge height above ground level (e.g., MacGorman et al. (1998)). At the same time, the fast negative breakdown continues to propagate for several microseconds before finally dying out. From the large amplitude and relatively long duration of the opposite-polarity field change, one can infer that the current is not constrained to the IBP itself but develops retrogressively back through the negative breakdown leading to the IBP, converting a potentially weak streamer-leader channel to a hot conducting leader and completing the step. That the current during a negative leader step develops in a retrograde manner back along the incoming breakdown channel has been shown by in-situ balloon-borne observations of negative leader stepping during an IC flash by Winn et al. (2011), and by high speed video observations around the time of IBPs of –CG flashes by Stolzenburg et al. (2013), as discussed later. Because sub-pulses previous to the final sub-pulse do not initiate the opposite polarity field change, one can infer they are not connected to the incoming leader breakdown, but instead are isolated from the leader and from each other. The question then becomes whether the sub-pulse sparks short out enough potential difference to account for the observed TGFs.

In terms of the space stem/space leader model of negative leader stepping (e.g., Petersen et al. (2008); Biagi et al. (2010)), the sub-pulse sparks would correspond to conducting space leaders that occur in the negative streamer region ahead of the developing leader. Continuing the space leader interpretation, the final sub-pulse develops back into the incoming leader, at which point the leader's potential rapidly advances to the opposite end of the space leader, producing the negative corona flash that launches the relativistic electrons. This scenario could explain TGF A, which was initiated a few microseconds after the final, sharply-pointed negative peak of the sferic (Figs. 4a and S15). TGF A also produced the most surface-detected energy of the different TGFs (561 VEM total, or 1150 MeV; Table S1). Because the TGF occurred just above the TASD boundary (Figs. 2 and S1), the detected energy could have been up to 50% larger had it been entirely captured. Similarly, the scenario could also explain the main onset of TGF B, which occurred at the same time as the final sub-pulse peak (solid vertical line in Figs. 4b and S16).

For TGFs C and D, however, and for the early initial detection of TGF B, the TGF onsets were associated with sub-pulses that did not initiate a retrograde current (Figs. 4, S17, S18, and the left-most vertical dotted line in Fig. S16). These and the other early sub-pulses of the IBPs would be characterized as attempted space leaders, and may have somehow paved the way for the final sub-pulse, but otherwise appeared to be independent of each other and not connected back to an incoming leader. The gamma events of TGFs C and D had total surface detections of 212 and 440 VEM (434 and 902 MeV),

respectively, with TGF D being the second strongest TGF after TGF A. At the same time, the total activity of TGF B, which was most closely associated with the IBP's final sub-pulse and presumably the best candidate for being connected to the incoming leader, had the weakest total surface detection of all, 112 VEM (229 MeV).

Storm-to-storm variability, as well as that from flash to flash in the same storm, coupled with the small sample size makes it difficult to compare the different observations. However, the fact that three TGF events (C, D, and the initial lone detection of TGF B) were initiated by sub-pulses that did not connect back into the incoming breakdown of the IBP, and the subsequent activity of TGF B producing a weak TGF despite its sub-pulse eventually connecting back into the incoming breakdown, indicates that the occurrence and strength of the gamma bursts are determined more by the amplitude and impulsiveness of the initiating sub-pulse rather than by the incoming breakdown consisting of a hot conducting leader.

From the above results, as well as the IBPs being produced by fast negative streamer breakdown, the sub-pulses are analogous to the space leader in negative leader stepping in that they occur within negative streamers ahead of the leader. Instead of being produced by a relatively slow-developing thermal space stem, the sub-pulses are impulsive sparks caused by sudden instabilities in extended-length streamer channels associated with fast propagation speed of streamers. And instead of the impulsivity of the step being produced by the space leader suddenly contacting a conducting leader channel and rapidly propagating the leader potential forward to the head of the space leader, the impulsiveness and negative corona burst is produced by the spark itself. The succession of sub-pulse sparks eventually causes one to develop back into a somewhat diffuse leader, giving rise to the backward-developing current that further establishes and converts the incoming breakdown into a well-defined hot conducting channel. This scenario agrees with high-speed video observations by Stolzenburg et al. (2013, 2014), indicating that the 'unusual' steps of IBPs occur ahead of a weakly-conducting nascent leader rather than a continuously hot, conducting channel (see later discussion).

If the space stem/space leader process is what initially advances the conducting leader channel, a legitimate question concerns how such a hot leader is produced in propagating from the end of the preceding IBP (or from the flash start) to the beginning of the IBP in question, in the absence of discernible space stem/space leader activity. At some point the leader becomes self-propagating (e.g., da Silva et al. (2019)), but apparently this does not occur in the early stages of the breakdown, as evidenced by the increasing need for and strength of IBPs in the initial few milliseconds of negative breakdown. Up until then, the advancing negative breakdown between IBPs appears to be a system of relatively weakly conducting negative streamers, which can self-propagate more readily.

From the INTF observations, the average speed of the downward negative breakdown at the beginning of the TGF-producing flashes is $\simeq$1.0–2.5 $\times 10^6$ m/s (e.g., Figure 3a and Supporting Figures S7–S13), an order of magnitude or so faster than other estimates of developing leader speeds (e.g., Behnke et al. (2005)). Similarly fast progression speeds were reported during the upward development of TGF-producing IC discharges by Cummer et al. (2015), who used ionospheric reflections to determine the altitude and hence the upward progression speed of successive radio pulses of TGF-producing IC flashes. For three different flashes, the speeds were noted to be remarkably similar and fast, ranging from 0.8–1.0$\times 10^6$ m/s. As in the present study, the TGFs were produced partway along the vertical development (in their case upward), when the leader was $\simeq$1–2 km in extent. The fact that TGFs were not also produced by subsequent pulses at higher altitude during the vertical development led them to ask why this did not happen, in view of the leader lengths being proportionally longer. A similar question would apply to the present, downward-directed observations at the beginning of the –CGs.

Taken together, the results suggest a scenario in which a 'step' consists of a) intermediate-speed negative streamer breakdown being launched at the end of the previous step's IBP, which progresses in a forward direction until b) initiating accelerated-speed FNB and an IBP having embedded sub-pulses, one of which c) initiates a strong current that develops retrogressively backward through the IBP and its preceding negative breakdown, thermalizing and extending the negative leader. The IBP then reverts back to intermediate or slower-speed negative streamer breakdown, beginning the next step. Whether a TGF is produced during the IBP is largely decoupled from the preceding negative breakdown, explaining the independence of TGF production on the extent of the negative breakdown up to that point. Where the preceding extent plays a role is in enhancing the electric field ahead of its developing front, to the point that the FNB is initiated. The field enhancement is due to the cumulative dipolar charge transfer of the negative breakdown during each step (e.g., Krehbiel (2018); Attanasio et al. (2019); Cummer (2020)), causing successive IBPs to become stronger with time. The TGFs of this study were produced by the strongest IBP of the flash, but in 3 of the 4 flashes one or two additional bursts occurred that were associated with separate episodes of FNB and sub-pulse activity (see Figs. S10d,g, S12c,f and S13c,f). The additional gamma events occurred during less strong IBPs within $\simeq$100–150 μs either before or after the main gamma events, and represent sparsified examples of the TGF activity that would be expected during the kind of complex IC IBP events seen in Figures 6 and 7.

The above scenario for the stepping provides an explanation for the optical observations of Stolzenburg et al. (2013), in which partially-obscured luminosity in the first 1–2 ms of a –CG flash advanced downward with a series of surges associated with bright optical emissions at the times of successive IBPs. The observations were obtained from high speed video recordings having 20 μs time resolution. Each bright surge lasted about 80–100 μs and was preceded by dim, linearly downward extension of the channel, with the brightest frame "immediately followed by backward lighting of the entire tail" that preceded the bright surge. The sequence then started over again with renewed dim downward extension of the channel to a lower elevation angle, with the process repeating for up to five surges. In terms of the above scenario, a) the linear downward channel extensions would correspond to the intermediate-speed, inter-IBP negative streamer activity, b) the succeeding bright optical emissions would have been produced by the spark-like sub-pulses of the IBP, and c) the immediately following upward propagating light would be produced by the retrograde current traveling back up along the path of the pre-IBP activity, converting it into a hot conducting leader. As noted earlier, Winn et al. (2011) observed similar backward propagating current events following individual steps of an already-developed negative leader toward the end an IC flash, using close balloon-borne electric field change observations of the flash. The correlation of bright optical pulses with –CG IBPs was extended by Stolzenburg et al. (2016) to be produced by IC-type IBPs at the beginning of hybrid –CG flashes. Similar to Marshall et al. (2013), the IBPs were considered to be candidate producers of TGFs, on the basis of the IBPs being complex and having strong sub-pulses.

The mechanism for producing the spark-like sub-pulses and TCEs within the fast negative breakdown would be essentially the same as that which causes the FPB and FNB to be the producer of high-power VHF radiation, described as being the strongest natural source of VHF radiation on Earth (LeVine, 1980). Due to their fast propagation speed, both polarities of streamers would have extended partially-conducting tails that would become unstable in the strong ambient fields (F. Shi et al., 2016; Malagon-Romero & Luque, 2019). The resulting rapid current cutoff, coupled with meters-long extents and large numbers, make both polarities of streamer systems potent radiators at VHF (Rison et al., 2016). The negative polarity streamers of FNB would have more robust and extensive tails than positive streamers, that could occasionally extend over longer distances, with the resulting instabilities and currents producing hot, spark-like conducting channels of the sub-pulse TCEs. In addition to explaining the optical emissions associated

with IBPs, the sudden occurrence of a dynamically impulsive conducting channel would provide the means for initiating relativistic electron avalanches (Moss et al., 2006; Celestin & Pasko, 2012; Celestin et al., 2015).

It is interesting to note that, in addition to being produced by sub-pulses, it may also be possible for relativistic electron avalanches to be initiated by individual negative streamers themselves. This is suggested by the modeling study of Moss et al. (2006), who showed that the extremely strong electric fields sufficient to accelerate electrons into the runaway regime will occur briefly immediately prior to branching of the streamers. Electrons produced in association with branching can reach kinetic energies as large as 2–8 keV or larger, well into the runaway electron regime. Although determined to occur in the corona flash and streamer zone at the tip of a conducting leader, the process might also occur at the tips of streamers having relatively long conducting tails. The branching process was noted to strongly favor negative streamers over positive, due to positive streamers requiring photoionization to sustain their propagation. If it occurs, the branching mechanism would be a powerful adjunct to TCEs, since large numbers of individual streamers exist within a propagating system that are spread over a much larger cross-sectional area than an individual conducting leader or TCE channel, and are continually branching.

Other issues of note concerning the observations are a) that the TGFs are broadly rather than narrowly beamed, favoring a tip-based conducting channel model (Mailyan et al., 2019), and b) are commonly tilted at substantial angles from vertical. From the TASD footprints and source altitudes, the half angular width of the beaming is on the order of 35° or so (≃2.4 km radial plan spread for a 3.3 km source altitude). From the INTF observations of Figure 5 (repeated in larger scale in Supporting Figs. S19–S23), the tilting can be 45° or more, depending on the 3-dimensional development of the discharge. Finally, successive sub-pulses can be oriented in different directions, as indicated by successive onsets occurring in different directions for TGF B (Figs. S16 and S20).

We note that the simulations of our previous study (Abbasi et al., 2018) implied TGF fluences on the order of 10^{12}–10^{14} relativistically-generated gamma photons, several orders of magnitude less than satellite-inferred fluences of $\simeq 10^{16}$–10^{18} photons. From Celestin et al. (2015) (Table 1), total fluences of 10^{12}–10^{14} photons correspond to potential drops of ≃10 to 50 MV or so at the conducting channel tips, while fluences of $\simeq 10^{16}$–10^{18} photons correspond to larger potential drops of 160–300 MV. That the observed fluences are relatively weak would be consistent with the inference that the TGFs are produced by isolated conducting sparks that short out lesser amounts of potential difference. However, if km-long conducting leaders are not involved, the question is whether sufficient potential difference is available for producing the relativistic electrons and the observed gamma radiation. For example, from Celestin et al. (2015) (Fig. 3), 5–10 MV potential drops would not produce relativistic electrons greater than ≃1–2 MeV. On the other hand, 60 MV (160 MV) of potential drop would produce relativistic electrons up to 9 MeV (20 MeV). From the modeling, then, at least 50 MV of potential drop would be required to produce the expected gamma energies observed in this study. The predicted fluences corresponding to 60 MV (160 MV) potential drop, however, is $\simeq 6 \times 10^{14}$ ($\simeq 4 \times 10^{16}$) photons, two orders of magnitude greater than the inferred fluences of these TGFs. Thus the observations are inconsistent with the leader-streamer modeling, in that the fluences corresponding even to the minimum likely detected photon energy produced by 60 MV potential drop would be at the upper end of the implied fluence values of Abbasi et al. (2018).

The question of available potential energy can be addressed by considering the electric field required for streamer propagation, called the stability field E_{st}. From da Silva and Pasko (2013), at one atmosphere of pressure $E_{st} \simeq 5{\times}10^5$ V/m for positive streamers, but $\simeq 12.5{\times}10^5$ V/m for negative streamers in virgin air. The fields scale according to pressure, so at 5 km altitude (0.5 atm) $E_{st}^- \simeq 6 \times 10^5$ V/m. Thus FNB propagating over the 100–240 m long extents of the TGF IBPs (Table S3) would experience

total potential differences of ≃60 to 150 MV, with 60 MV being consistent with observed photon energies up to ≃9 MeV. Some or all of the potential difference that is not shorted out by the sparking would be available for additional avalanche growth down to the propagation threshold of 2×10^5 V/m, which is not accounted for in the Celestin et al. (2015) calculations. Also not accounted for are dynamical effects in initiating the relativistic electrons that are associated with the sparking being impulsive, which are significant for pulsed discharges (Section 5.4.3 of Nijdam et al. (2020)). Finally, using the stability field values doesn't account for the field intensification ahead of the advancing streamer front, which can be as much as 50% above the ambient E_{st} value (e.g., Attanasio et al. (2019); da Silva et al. (2019)). For IC flashes at higher altitudes, E_{st} would be reduced by about another factor of two, but this would be offset by the IC events typically being longer by a factor of two or more, leaving the total potential differences about the same. Finally, we note that vertical profiles of the electric potential in electrified storms similar to those being studied show the total potential differences available for IC and –CG flashes are both on the order of 200 MV (e.g., Fig. 1 of Krehbiel et al. (2008); Fig. 3 of da Silva and Pasko (2015)).

In short, while the details remain to be understood, taken together, sufficient potential difference is available to produce gamma radiation into the 10–20 MeV range or potentially higher, consistent with the observations and the physics of the Surface Detector responses. The main issue is the fluence values. A possible explanation for the fluence inconsistency that allows both the observational data and the modeling to be correct would be that the gamma photons are produced by ≃10 to 50 MV of potential drop, which from Fig. 3 and Table 1 of Celestin et al. (2015) would produce relativistic electron energies in the range of ≃2–9 MeV and fluences in the observed range of 10^{12}–10^{14} photons. Once initiated, the electron energies would be further accelerated up to ≃10–20 MeV by the enhanced field ahead of the streamer front and any ambient field beyond greater than the threshold field of 2×10^5 V/m. Because the extent of the field ahead of the streamer system would be less than an e-folding avalanche length, the fluences would not change significantly while the electron energies increase.

To the extent that satellite-detected TGFs from IC flashes have substantially larger fluences, the implication is either a) that the satellite detected events emanate from the tips of fully-formed, kilometer-length or longer conducting leaders, in which case fluences of 10^{16}–10^{18} photons are achieved directly from the negative corona flash produced by potential drops as large as several hundred MV, or b) that the fluences of lesser potential drops are enhanced by the relativistic feedback process. The above-mentioned observations by Cummer et al. (2015) raise the important question about the leader hypothesis of why TGFs are not produced later in the development of upward, kilometer or multi-km conducting leaders. Instead, and as additionally discussed below, the observational data supports the idea that the much greater satellite-detected fluences are due to the relativistic feedback mechanism, which was initially developed to explain this very issue (Dwyer, 2012).

Another substantial difference between the present observations and those obtained by satellites concerns the durations of the TGFs, being 5–10 μs for the downward –CG TGFs, versus ≃20–200 μs for the upward, IC-generated TGFs (e.g., Mailyan et al. (2016, 2018); Østgaard et al. (2019)). The difference can be at least partially explained by observations that IC flashes can often have long-duration, complex sferics, consisting of multiple sub-pulses and IBPs, each of which would be capable of producing TGFs. Examples of such sferics are seen in Figures 6 and 7. Of particular note are the observations of three TGF events by Lyu et al. (2018), in which complex dB/dt events produced Fermi-detected TGFs having continuous durations of ≃50, 100, and 120 μs. In the latter two cases, gamma detections occurred intermittently for an additional 60 and 100 μs both before and/or after the main activity, extending their overall durations to ≃160 and 220 μs, respectively. For each of the three events, the TGFs were produced during the occur-

rence of a slow, smooth component of the sferic, indicative of being caused by electron avalanching that produced the TGFs. Complex, lengthy sferics were also produced by the other two events of the same Lyu et al. study.

Of particular interest, and the best-studied example, was the first event of 4 September 2015 (Fig. 2 of Lyu et al. (2018)), which occurred over west-central Florida. Its sferic closely resembled that of the first complex IBP of the Utah IC, seen in the top panel of Figure 7. In both cases, the sferic lasted for ≃250 μs and consisted of several highly impulsive sub-pulses before and after a central event. For the Utah IC the central event was itself a large-amplitude IBP, while for the Florida IC it was the large-amplitude slow field change of the electron avalanche. The comparison, along with the other Lyu et al. examples illustrates the fact that a) long-duration TGFs can be produced by IC flashes having complex sferics, and b) that the only difference between the Utah and Florida ICs is that the latter initiated strong runaway avalanching, while the former did not, but based on the sferic similarities, could well have done so. The second complex IBP of the Utah IC, seen in the bottom panel of Figure 7, would have been even more capable of generating a long-duration TGF based on its greater duration and VHF signal strength.

Pu et al. (2019) extended Lyu et al.'s study to include five additional examples of continuously and intermittently long-duration TGFs being produced by other IC flashes having complex IBP sferics. Finally, we call attention to the study by Tilles et al. (2020) of a high peak current (247 kA) energetic in-cloud pulse (EIP) that was observed in Florida with the same physical INTF and FA instrumentation of the present study. The EIP was produced by a complex sequence of repeated IBP-type fast breakdown activity, but its sferic was completely dominated by a sequence of three successive slow, smooth relativistic avalanches indicative of being produced by relativistic feedback. No gamma-detecting satellite happened to be in view of the EIP, but the flash undoubtedly produced an upward TGF (Lyu et al., 2016; Cummer et al., 2017) and is an example of how IC flashes are capable of producing extremely strong avalanching as a result of complex IBP-type activity.

3.4 Summary

The results can be summarized as follows:

1. Downward TGFs occur during strong, "classic" initial breakdown pulses (IBPs) of downward negative CG and IC flashes. In turn, the IBPs are produced by streamer-based fast negative breakdown (FNB).
2. The TGFs consist of short, ≃5–10 μs duration bursts of gamma rays initiated by sub-pulses during the IBPs, and apparently also by brief episodes of enhanced speed FNB.
3. The correspondence of TGFs with sub-pulses is indicative of the sub-pulses being produced by spark-like transient conducting events (TCEs), consistent with their sferics being impulsive or cusp-like and explaining the bright optical activity observed during IBPs of –CG and IC flashes.
4. In turn, the TCEs are considered to result from instabilities in occasionally long streamer tails or partially conducting channels embedded within the FNB of the IBP, and to be isolated from each other and from the incoming breakdown preceding the IBP.
5. Based solely on the well-understood physics of surface detector responses and Compton electron production, individual electrons detected by the TASD surface stations correspond to photon energies no less than 2.6 MeV if detected in a single scintillator layer and 6.2 MeV if detected in both layers.
6. From the electric field required to propagate negative streamers in virgin air at –CG altitudes, the electric potential difference experienced by the FNB over the 100-m to 240 m extents of TGF-producing IBPs is ≃60 to 150 MV.

7. Instead of the breakdown leading up to an IBP being a long conducting leader, it appears to be due to weakly-conducting negative streamer breakdown that gets accelerated to produce the IBP.
8. The observational data indicate that the streamer to leader transition of successive steps is caused by current generated during the characteristic opposite-polarity field change in the final stage of the step's IBP.
9. The initial upward negative breakdown of IC flashes is shown to be produced in the same basic manner as the initial downward breakdown of –CG discharges, but generally lasting longer and having longer step sizes.
10. The long durations of satellite-detected TGFs can be explained by IC flashes producing complex clusters of sub-pulses and IBPs, which enable the development of continuous and intermittent electron avalanching. Sparse versions of this are seen during successive IBPs of –CG flashes.

While the present study has been underway, the TASD has been in the process of expanding by a factor of four in its coverage area, and the TGF and lightning observations are continuing. The LMA network is being similarly expanded, and an additional VHF interferometer instrument is to be added in the current year. Detailed analyses of additional observations are the subject of continued study.

Appendix A Methods

A1 Instruments

Telescope Array Surface Detector. The TASD consists of 507 scintillator detectors arranged on a 1.2 km square grid. The array is situated on a relatively high, 1400 m altitude desert plain in west-central Utah, and covers an area of $\simeq$700 km^2. Each detector has two scintillator planes, each 3 m^2×1.2 cm thick, separated by a 1 mm thick steel sheet and housed inside an RF-sealed and light-tight stainless steel enclosure. The TASD is designed to detect the charged components — primarily electrons, positrons, and muons — of the cosmic ray-induced Extensive Air Shower (EAS). An event trigger is recorded when three adjacent SDs observe a signal greater than that of 3 Minimum Ionizing Particles (MIPs) ($\simeq$150 FADC counts) within 8 μs. When an event trigger occurs, the signals from all individually-triggered SDs within $\pm$ 32 μs are recorded (Abu-Zayyad et al., 2013). An individual SD trigger occurs upon observing a signal of amplitude greater than 0.3 MIP ($\simeq$15 FADC counts) within 8 μs.

The TASD is an inefficient detector of gamma radiation, relying on the production of high-energy electrons through the Compton scattering mechanism in either the thin scintillator, steel housing, or air above the detector units. Detailed simulations of this process have been described in the authors' previous study (Abbasi et al., 2018). Incident gamma-ray photons with energy above 10 MeV will on average deposit about 20% (30%) of the energy of a MIP in the upper (lower) scintillator. The majority of photons will not interact in the detector at all; those that do will primarily create Compton recoil electrons with kinetic energies at or below the photon energy level. The Compton electrons can then deposit energy up to a MIP (2.4 MeV) in each plane of the scintillator, though the amount deposited in each plane will depend on where the Compton scatter occurs.

Lightning Mapping Array. As shown in Figure 1, the LMA consisted of nine stations located within and around the TASD, and determines accurate 3-D observations of peak VHF radiation events above threshold in 80 μs time intervals. (Rison et al., 1999; Thomas et al., 2004) In addition to showing the large scale structure and development of flashes and the lightning flashing rate, its observations were used to determine the plan distance to the TGF events and also to finely calibrate the INTF azimuth and elevation

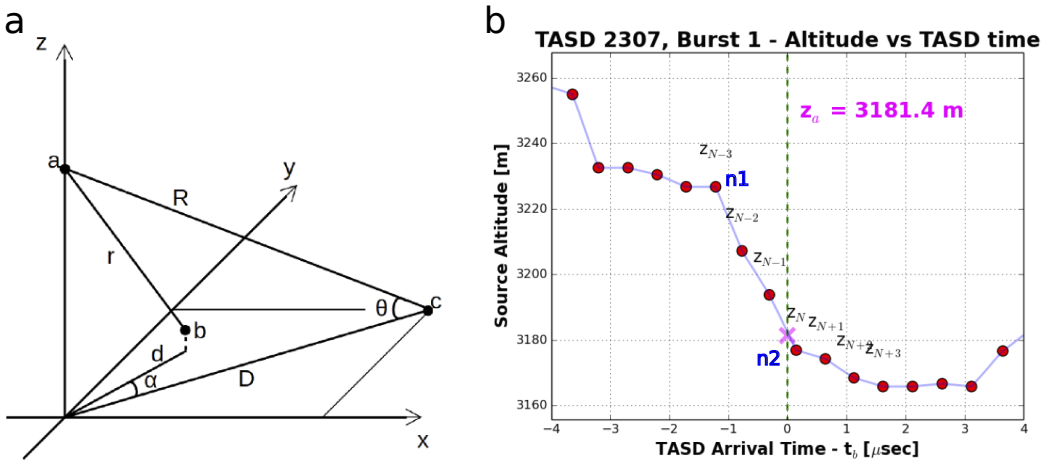

Figure A1. Methods information. (**a**) Source-centric coordinate system for temporal correlations. The TGF source is at (x_a, y_a, z_a), with the plan x, y location serving as the coordinate origin. The TASD station is at location b relative to the origin and the reference altitude, and the INTF/FA is at the more distant location c. (**b**) Iteration at 0.5 μs time steps used in the alternative approach for determining the source altitude (TGF A in this case), showing the occurrence of enhanced-speed downward FNB immediately before the TGF onset (red 'x').

values. The angular calibration was done separately on a flash-by-flash basis for each TGF event.

VHF lightning interferometer (INTF) and fast electric field change antenna (FA). The INTF records broadband (20–80 MHz) waveforms at 180 MHz from three flat-plate receiving antennas, and determines the two-dimensional azimuth and elevation arrival directions of the VHF radiation with sub-microsecond resolution (Stock et al., 2014). This is done on a post-processed basis, and determines the radiation centroid in overlapping 0.7 or 1.4 μs windows. Triangular baselines of 106–121 m were used to maximize the angular resolution over the TASD. The elevation angles were used to determine the source altitude of the TGFs, based on the LMA-determined plan distance to the source, and the amplitude of the received signals was used to determine the VHF power of the centroids. The fast electric field change antenna (FA) provided high resolution (180 MHz) measurements of the low frequency (LF/ELF) discharge sferics that are key to interpreting the INTF and LMA observations.

A2 Analysis procedures

Figure A1a shows the coordinate system used for analyzing the INTF and TASD observations. For simplicity, this is done in a Cartesian coordinate system centered at the x_a, y_a plan location of the TGF's source. The plan location is determined from the mean values of the latitude and longitude of LMA sources within ±1 ms of the TGF's occurrence, seen in Supporting Figs. 10e–13e. The altitude values are determined relative to a 1400 m reference plane, which is within 2 m of the GPS altitude of the VHF receiving antenna used as the INTF's GPS time base. The plan locations and altitudes of the TASD stations are precisely known and fully accounted for in the calculations, with trigger times of each TASD's data accurate to 40 ns. Similarly, the INTF source directions were carefully calibrated to within 0.08 degrees in azimuth and 0.26 degrees in elevation, obtained by comparing accurately-located LMA sources with corresponding INTF source directions separately for each flash.

Given the LMA-estimated values of x_a and y_a, two additional measurements are needed to determine the TGF's onset altitude z_a and time t_a. The source altitude can be estimated from the LMA observations, but has insufficient accuracy and temporal resolution to resolve the fast downward breakdown that occurs during the parent IBP (typically 100–150 m in 5–10 μs). Instead, the altitude is more accurately determined from the INTF elevation angle θ_c vs. time, which is obtained with sub-microsecond resolution. In particular, $z_a = D \tan\theta(t_c) = z_a(t_c)$, where $D = \sqrt{x_c^2 + y_c^2}$ is the plan distance between the INTF and TGF. For an event at altitude z_a and time t_a, the arrival times at TASD i and the INTF are given by

$$t_b = t_a + r_b/c \tag{A1}$$

$$t_c = t_a + R/c\,, \tag{A2}$$

where $r_b = [x_i^2 + y_i^2 + (z_a - z_i)^2]$ and $R = [x_c^2 + y_c^2 + z_a^2]$ are the slant ranges from the TGF source. Because the plan locations are considered to be known, $r_b = r_b(z_a)$ and $R = R(z_a)$, so the time-of-arrival equations represent two equations and two unknowns, t_a and z_a. The unknowns are determined from two measurements, in particular the arrival time t_b at a given TASD station, and the INTF elevation measurements, $\theta_c(t_c)$. Since θ_c varies with time during the IBPs, it is not known in advance which time value t_c to use for determining z_a. This results from z_a depending on itself in a manner that is not amenable to analytical inversion. But the equations are readily solved by iterating over the range of values for z_a, or equivalently over the possible θ_c or t_c values.

Two semi-independent approaches were used to determine the solutions. Both used an alternative form of (A2) obtained by eliminating t_a to obtain

$$t_c = t_b + \frac{(R - r_b)}{c} = t_b + \Delta t_b\,, \tag{A3}$$

where $\Delta t_b = (R/c) - (r_b/c)$ corresponds to the time shift for comparing a given TASD's observations with the INTF/FA observations. For an assumed source altitude z_a, the time shift between the onset time t_b at a given TASD station and its arrival time t_c at the INTF is readily calculated from the difference of the slant ranges R and r_b of the source relative to the INTF and the TASD in question. In turn, the t_c value can be used to determine $\theta_c(t_c)$ and hence z_a. Comparing the assumed and inferred z_a values forms the basis for a closed loop iteration procedure, in which the assumed z_a is simply replaced by the new z_a value (Supp. Fig. S14). Consistency is reached in just a few steps. At the same time, the corresponding INTF elevation angle θ_c and arrival time t_c at the INTF is also determined.

The above is the method used by the first approach, as described in Section 2.2. For each of the primary TGFs shown in Figure 4, the source altitudes inferred from the

onset times at the different TASDs were in good agreement, having uncertainties of 30 m, 16 m, 10 m, and 40 m for TGFs A, B, C and D, respectively (see Supporting Table S2). To guard against outliers, median values were used for determining the final z_a and t_a values at onset, as well as θ_c and t_c. The final t_c values provide a reference time for evaluating the onset times of each gamma-ray event. As can be seen from the TASD plots in Figure 4, in most cases the waveforms begin within a microsecond or so of the indicated t_c onset time. Detections that begin in advance of or after the indicated onset, as for TGF B, are indicative of different onset times.

Instead of using a closed-loop iteration process, as above, the second approach worked backward from the INTF observations of the elevation angle θ_c vs. t_c to determine z_a and Δt in reverse. This was used to predict the arrival times at two of the TASD stations that detected the TGF most strongly, and involved stepping through the t_c times and corresponding θ_c values in 0.5 μs increments and determining the time when the difference between the predicted and observed t_b values passed through zero. The common reference time t_b was defined to be when the TASD signal first ascended to half of its eventual peak amplitude on the 2 stations with the strongest signals (short vertical dotted lines in the TASD waveforms of Supp. Figs. S10-S13c,d), which were averaged to obtain the final estimate of the time alignment.

Figure A1b shows the results of the stepping procedure for TASD 2307 of TGF A. The plot shows the difference between the observed and trial t_b times of the main gamma-ray event, with the interpolated step value where Δt_b goes through zero determining the value of t_c (red 'x' in the figure). For this (and the iterative) procedure to work, the INTF data was processed with higher time resolution and increased overlap to make $\theta_c(t_c)$ more continuous. This is a standard procedure for analyzing INTF observations (Stock et al., 2014), and allows more detail to be seen in θ_c vs. time. For these analyses, the higher resolution data was downsampled to 0.5 μs intervals by using the median of the higher frequency processing over a ± 4 μs interval around each 0.5 μs point (unfilled gray circles in panels c and d of Supp. Figs. S10-S13).

What is informative and notable about the example of Figure A1b is that the onset time of the strong gamma burst of TGF A coincided with the end of a brief interlude of rapid descent in the source altitude, denoted by the vertical dashed line in the figure. The speed of the descent is determined from the spacing between the dots, which occur at 0.5 μs intervals. In 1.5 μs (three step intervals), the source descended about 50 m, corresponding to a downward speed of 3.3×10^7 m/s. This enhanced-speed interlude was unresolved by the normal processing, and instead caused the step discontinuity seen in Figure 4a during the fast negative breakdown. The stepping method of determining the onset time agreed well with the result of the iterative approach, which showed the gamma-ray onset to be at the end of the discontinuity (bold vertical line in Figure 4a). The agreement is not surprising, given that the same basic data was used in the two analysis approaches. But the correspondence with different approaches indicates good precision in the procedures, and reinforces the observation that the gamma bursts occur in association with intervals of enhanced speed breakdown.

A3 Measurement uncertainties

Whereas the INTF and FA data are well-synchronized timewise by being simultaneously digitized at a high rate, the main question is how accurately the TASD waveforms from the different TASDs are synchronized with the INTF/FA data. As discussed above, this can be qualitatively determined by examining the waveforms from the different SDs relative to the inferred onset time (vertical line) for each of the TGF events in Figure 4. In most cases, the observed onsets are within a microsecond or less of the inferred time, with important exceptions in TGFs B and C.

A quantitative result can only be obtained from propagating the measurements' standard errors through calculations in the previous section, using the general form of

$$\delta f = \sqrt{(\frac{\partial f}{\partial x_1}\delta x_1)^2 + ... + (\frac{\partial f}{\partial x_n}\delta x_n)^2} \tag{A4}$$

where $f = f(x_1, ..., x_n)$. Detector locations are known to centimeter accuracy and have negligible contributions. Similarly, gamma-ray detection trigger times are known on the order of sampling rate (10s of ns). Both are taken into account, but have very little effect on final uncertainties. Primary error sources, then, come from the two instances of taking averages described the previous section; TGF source plan locations are taken as the mean GPS location of LMA sources within 1 ms of particle detections, and its uncertainty is the standard error. TGF source elevations are done the same way — a mean is taken of all INTF sources within 4 μs of the TGFs inferred arrival at the interferometer (from Equation A3), and its uncertainty is the standard error.

All subsequent calculations can then be shadowed by their error counterparts using Equation A4 and are presented in Tables S2 and S3. Typically, altitude measurements are much less precise for this type of study, but here altitude determination comes from the higher-sampled INTF data whereas plan location data is supplied by only a few LMA points. As a result, altitude uncertainties are 30, 20, 10, and 40 meters for TGFs A, B, C, and D respectively, compared to horizontal location errors of 150, 80, 40, and 300 meters. Timing uncertainties follow the same trend, with 0.7, 0.4, 0.2, and 1.4 μs for each respective TGF. Standard errors for all other calculations are shown in Tables S2 and S3.

Notice that elevation errors are nearly equal (Table S2), but poor grouping of LMA data at the time of TGF D means a larger error in the plan location. As the error is propagated through each calculation, quantities for TGF D continue to be the least reliable among the four, showing that the low LMA sampling rate and possible mislocations during fast breakdown are the main contributors to all further uncertainty.

Acknowledgments
The lightning instrumentation, operation and analyses of this study have been supported by NSF grants AGS-1205727, AGS-1613260, AGS-1720600 and AGS-1844306. The Telescope Array experiment is supported by the Japan Society for the Promotion of Science through Grants-in-Aids for Scientific Research on Specially Promoted Research (15H05693) and for Scientific Research (S) (15H05741), and the Inter-University Research Program of the Institute for Cosmic Ray Research; by the U.S. National Science Foundation awards PHY-0307098, PHY-0601915, PHY-0649681, PHY-0703893, PHY-0758342, PHY-0848320, PHY-1069280, PHY-1069286,PHY-1404495, PHY-1404502 and PHY-1607727; by the National Research Foundation of Korea (2015R1A2A1A01006870, 2015R1A2A1A15055344, 2016R1A5A1013277, 2007-0093860, 2016R1A2B4014967, 2017K1A4A3015188); by the Russian Academy of Sciences, RFBR grant 16-02-00962a (INR), IISN project No. 4.4502.13, and Belgian Science Policy under IUAP VII/37 (ULB). The foundations of Dr. Ezekiel R. and Edna Wattis Dumke, Willard L. Eccles, and George S. and Dolores Doré Eccles all helped with generous donations. The State of Utah supported the project through its Economic Development Board, and the University of Utah through the Office of the Vice President for Research. The experimental site became available through the cooperation of the Utah School and Institutional Trust Lands Administration (SITLA), U.S. Bureau of Land Management (BLM), and the U.S. Air Force. We appreciate the assistance of the State of Utah and Fillmore offices of the BLM in crafting the Plan of Development for the site. We also wish to thank the people and the officials of Millard County, Utah for their steadfast and warm support. We gratefully acknowledge the contributions from the technical staffs of our home institutions. An allocation of computer time from the Center for High Performance Computing at the University of Utah is gratefully acknowledged. We thank Ryan Said and W. A. Brooks of Vaisala Inc. for providing high-

quality NLDN data lightning discharges over and around the TASD under their academic research use policy as well as several anonymous reviewers for their requests and comments, the responses to which significantly improved the paper. Data that support the conclusions presented in the manuscript are provided in the figures of the paper. Additional information can be found in the supporting material and is available on the Open Science Framework (DOI: 10.17605/OSF.IO/Z3XDA).

References

Abbasi, R., et al. (2017). The bursts of high energy events observed by the telescope array surface detector. *Physics Letters A*, *381*(32), 2565 - 2572. doi: 10.1016/j.physleta.2017.06.022

Abbasi, R., et al. (2018). Gamma ray showers observed at ground level in coincidence with downward lightning leaders. *Journal of Geophysical Research: Atmospheres*, *123*(13), 6864-6879. doi: 10.1029/2017JD027931

Abu-Zayyad, T., et al. (2013). The surface detector array of the Telescope Array experiment. *Nuclear Instrumentation and Methods in Physics Research*, *A689*, 87-97. doi: 10.1016/j.nima.2012.05.079

Attanasio, A., Krehbiel, P., & da Silva, C. (2019). Griffiths and phelps lightning initiation model, revisited. *Journal of Geophysical Research: Atmospheres*, *124*(14). doi: 10.1029/2019JD030399

Behnke, S. A., Thomas, R. J., Krehbiel, P. R., & Rison, W. (2005). Initial leader velocities during intracloud lightning: Possible evidence for a runaway breakdown effect. *Journal of Geophysical Research: Atmospheres*, *110*(D10). doi: 10.1029/2004JD005312

Biagi, C. J., Uman, M. A., Hill, J. D., Jordan, D. M., Rakov, V. A., & Dwyer, J. (2010). Observations of stepping mechanisms in a rocket-and-wire triggered lightning flash. *Journal of Geophysical Research: Atmospheres*, *115*(D23). doi: 10.1029/2010JD014616

Briggs, M. S., et al. (2010). First results on terrestrial gamma ray flashes from the Fermi gamma-ray burst monitor. *Journal of Geophysical Research: Space Physics*, *115*(A7). doi: 10.1029/2009JA015242

Briggs, M. S., et al. (2013). Terrestrial gamma-ray flashes in the Fermi era: Improved observations and analysis methods. *Journal of Geophysical Research: Space Physics*, *118*(6), 3805-3830. doi: 10.1002/jgra.50205

Carlson, B. E., Lehtinen, N. G., & Inan, U. S. (2007). Constraints on terrestrial gamma ray flash production from satellite observation. *Geophysical Research Letters*, *34*(8). doi: 10.1029/2006GL029229

Celestin, S., & Pasko, V. (2011). Energy and fluxes of thermal runaway electrons produced by exponential growth of streamers during the stepping of lightning leaders and in transient luminous events. *Journal of Geophysical Research: Space Physics*, *116*(A3). doi: 10.1029/2010JA016260

Celestin, S., & Pasko, V. (2012). Compton scattering effects on the duration of terrestrial gamma-ray flashes. *Geophysical Research Letters*, *39*(2). doi: 10.1029/2011GL050342

Celestin, S., Xu, W., & Pasko, V. (2012). Terrestrial gamma ray flashes with energies up to 100 MeV produced by nonequilibrium acceleration of electrons in lightning. *Journal of Geophysical Research: Space Physics*, *117*(A5). doi: 10.1029/2012JA017535

Celestin, S., Xu, W., & Pasko, V. (2015). Variability in fluence and spectrum of high-energy photon bursts produced by lightning leaders. *Journal of Geophysical Research: Space Physics*, *120*, 10712-10723. doi: 10.1002/2015JA021410

Cummer, S. A. (2020). Indirectly measured ambient electric fields for lightning initiation in fast breakdown regions. *Geophysical Research Letters*, *47*(4). doi: 10.1029/2019GL086089

Cummer, S. A., et al. (2011). The lightning-TGF relationship on microsecond timescales. *Geophysical Research Letters*, *38*, L14810. doi: 10.1029/2011GL048099

Cummer, S. A., et al. (2015). Lightning leader altitude progression in terrestrial gamma-ray flashes. *Geophysical Research Letters*, *42*, 7792–7798. doi: 10.1002/2015GL065228

Cummer, S. A., et al. (2017, December). The connection between terrestrial gamma-ray flashes and energetic in-cloud lightning pulses. In *American Geophysical Union Fall Meeting 2017 Abstracts.* (AE33B-2547)

da Silva, C., & Pasko, V. (2013). Dynamics of streamer-to-leader transition at reduced air densities and its implications for propagation of lightning leaders and gigantic jets. *Journal of Geophysical Research: Atmospheres*, *118*(24), 13,561-13,590. doi: 10.1002/2013JD020618

da Silva, C., & Pasko, V. (2015). Physical mechanism of initial breakdown pulses and narrow bipolar events in lightning discharges. *Journal of Geophysical Research: Atmospheres*, *120*, 4989-5009. doi: 10.1002/2015JD023209

da Silva, C., Sonnenfeld, R. G., Edens, H. E., Krehbiel, P. R., Quick, M. G., & Koshak, W. J. (2019). The plasma nature of lightning channels and the resulting nonlinear resistance. *Journal of Geophysical Research: Atmospheres*, *124*(16), 9442-9463. doi: 10.1029/2019JD030693

Dwyer, J. (2003). A fundamental limit on electric fields in air. *Geophysical Research Letters*, *30*(20). doi: 10.1029/2003GL017781

Dwyer, J. (2004). Implications of x-ray emission from lightning. *Geophysical Research Letters*, *31*, L12102. doi: 10.1029/2004GL019795

Dwyer, J. (2012). The relativistic feedback discharge model of terrestrial gamma ray flashes. *Journal of Geophysical Research: Space Physics*, *117*(A2). doi: 10.1029/2011JA017160

Dwyer, J., et al. (2012). Observation of a gamma-ray flash at ground level in association with a cloud-to-ground lightning return stroke. *Journal of Geophysical Research*, *117*(A10303). doi: 10.1029/2012JA017810

Fishman, G. J., et al. (1994). Discovery of intense gamma-ray flashes of atmospheric origin. *Science*, *264*(5163), 1313–1316. doi: 10.1126/science.264.5163.1313

Foley, S., et al. (2014). Pulse properties of terrestrial gamma-ray flashes detected by the Fermi Gamma-Ray Burst Monitor. *Journal of Geophysical Research: Space Physics*, *119*, 5931-5942. doi: 10.1002/2014JA019805

Gjesteland, T., et al. (2012). A new method reveals more TGFs in the RHESSI data. *Geophysical Research Letters*, *39*(5). doi: 10.1029/2012GL050899

Grefenstette, B. W., Smith, D. M., Hazelton, B. J., & Lopez, L. I. (2009). First RHESSI terrestrial gamma ray flash catalog. *Journal of Geophysical Research: Space Physics*, *114*(A2). doi: 10.1029/2008JA013721

Hare, B., et al. (2016). Ground-level observation of a terrestrial gamma-ray flash initiated by triggered lightning. *Journal of Geophysical Research: Atmospheres*, *121*, 6511. doi: 10.1002/2015JD024426

Karunarathne, N., Karunarathne, S., Marshall, T., & Stolzenburg, M. (2014). Modeling initial breakdown pulses of CG lightning flashes. *Journal of Geophysical Research: Atmospheres*, *119*, 9003. doi: 10.1002/2014JD021553

Krehbiel, P. (2018). The initial development of intracloud flashes. In *American Geophysical Union Fall Meeting 2018.* (AE11A-01)

Krehbiel, P., et al. (2008). Upward electrical discharges from thunderstorms. *Nature Geoscience*, *1*. doi: 10.1038/ngeo162

LeVine, D. (1980). Sources of the strongest RF radiation from lightning. *Journal of Geophysical Research*, *85*(C7), 4091-4095. doi: 10.1029/JC085iC07p04091

Lu, G., Cummer, S. A., Li, J., Han, F., Smith, D. M., & Grefenstette, B. W. (2011). Characteristics of broadband lightning emissions associated with terrestrial gamma ray flashes. *Journal of Geophysical Research: Space Physics*, *116*(A3).

Lu, G., et al. (2010). Lightning mapping observation of a terrestrial gamma ray flash. *Geophysical Research Letters*, *37*, L11806. doi: 10.1029/2010GL043494

Lyu, F., Cummer, S. A., & McTague, L. (2015). Insights into high peak current in-cloud lightning events during thunderstorms. *Geophysical Research Letters*, *42*(16), 6836-6843. doi: 10.1002/2015GL065047

Lyu, F., et al. (2016). Ground detection of terrestrial gamma ray flashes from distant radio signals. *Geophysical Research Letters*, *43*(16), 8728-8734. doi: 10 .1002/2016GL070154

Lyu, F., et al. (2018). Very high frequency radio emissions associated with the production of terrestrial gamma-ray flashes. *Geophysical Research Letters*, *45*(4), 2097-2105. doi: 10.1002/2018GL077102

MacGorman, D. R., MacGorman, R., Rust, W. D., & Rust, W. (1998). *The electrical nature of storms*. Oxford University Press. Retrieved from `https://books.google.com/books?id=\_NbHNj7KJecC`

Mailyan, B. G., et al. (2016). The spectroscopy of individual terrestrial gamma-ray flashes: Constraining the source properties. *Journal of Geophysical Research: Space Physics*, *121*(11), 11,346-11,363. doi: 10.1002/2016JA022702

Mailyan, B. G., et al. (2018). Characteristics of radio emissions associated with terrestrial gamma-ray flashes. *Journal of Geophysical Research: Space Physics*, *123*(7), 5933-5948. doi: 10.1029/2018JA025450

Mailyan, B. G., et al. (2019). Analysis of individual terrestrial gamma-ray flashes with lightning leader models and fermi gamma-ray burst monitor data. *Journal of Geophysical Research: Atmospheres*, *124*(8), 7170-7183. doi: 10.1029/2019JA026912

Malagon-Romero, A., & Luque, A. (2019). Spontaneous emergence of space stems ahead of negative leaders in lightning and long sparks. *Geophysical Research Letters*, *46*(7), 4029-4038. doi: 10.1029/2019GL082063

Marisaldi, M., et al. (2014). Properties of terrestrial gamma ray flashes detected by AGILE MCAL below 30 MeV. *Journal of Geophysical Research: Space Physics*, *119*(2), 1337-1355. doi: 10.1002/2013JA019301

Marshall, T., et al. (2013). Initial breakdown pulses in intracloud lightning flashes and their relation to terrestrial gamma ray flashes. *Journal of Geophysical Research: Atmospheres*, *118*(19), 10,907-10,925. doi: 10.1002/jgrd.50866

Moss, G., Pasko, V., Liu, N., & Veronis, G. (2006). Monte carlo model for analysis of thermal runaway electrons in streamer tips in transient luminous events and streamer zones of lightning leaders. *Journal of Geophysical Research*, *111*(A02307). doi: 10.1029/2005JA011350

Nag, A., DeCarlo, B., & Rakov, V. (2009). Analysis of microsecond- and submicrosecond-scale electric field pulses produced by cloud and ground lightning discharges. *Atmospheric Research*, *91*, 316. doi: 10.1016/j.atmosres.2008.01.014

Nijdam, S., Teunissen, J., & Ebert, U. (2020). The physics of streamer discharge phenomena. *Plasma Sources Science and Technology*. doi: 10.1088/1361-6595/abaa05

Østgaard, N., et al. (2019). First 10 months of TGF observations by ASIM. *Journal of Geophysical Research: Atmospheres*, *124*(24), 14024-14036. doi: 10.1029/2019JD031214

Petersen, D., Bailey, M., Beasley, W., & Hallett, J. (2008). A brief review of the problem of lightning initiation and a hypothesis of initial lightning leader formation. *Journal of Geophysical Research: Atmospheres*, *113*(D17). doi: 10.1029/2007JD009036

Pu, Y., et al. (2019). Low frequency radio pulses produced by terrestrial gamma ray flashes. *Geophysical Research Letters*, *46*, 6990-6997. doi: 10.1029/2019GL082743

Ringuette, R., et al. (2013). TETRA observation of gamma-rays at ground level

associated with nearby thunderstorms. *Journal of Geophysical Research: Space Physics*, *118*, 7841. doi: 10.1002/jgra.50712

Rison, W., et al. (2016). Observations of narrow bipolar events reveal how lightning is initiated in thunderstorms. *Nature Communications*, *7*. doi: 10.1038/ncomms10721

Rison, W., Thomas, R., Krehbiel, P., Hamlin, T., & Harlin, J. (1999). A GPS-based three-dimensional lightning mapping system: Initial observations in central New Mexico. *Geophysical Research Letters*, *26*(23), 3573-3576. doi: 10.1029/1999GL010856

Roberts, O., et al. (2017). Terrestrial gamma ray flashes due to particle acceleration in tropical storm systems. *Journal of Geophysical Research: Atmospheres*, *122*, 3374-3395. doi: 10.1002/2016JD025799

Shao, X., Hamlin, T., & Smith, D. (2010). A closer examination of terrestrial gamma ray flash related lightning processes. *Journal of Geophysical Research: Space Physics*, *115*, A00E30. doi: 10.1029/2009JA014835

Shi, D., Wang, D., Wu, T., & Takagi, N. (2019). Temporal and spatial characteristics of preliminary breakdown pulses in intracloud lightning flashes. *Journal of Geophysical Research: Atmospheres*, *124*(23), 12901-12914. doi: 10.1029/2019JD031130

Shi, F., Liu, N., & Rassoul, H. K. (2016). Properties of relatively long streamers initiated from an isolated hydrometeor. *Journal of Geophysical Research: Atmospheres*, *121*, 7284-7295. doi: 10.1002/2015JD024580

Smith, D. M., et al. (2018). Characterizing upward lightning with and without a terrestrial gamma ray flash. *Journal of Geophysical Research: Atmospheres*, *123*(20). doi: 10.1029/2018JD029105

Stanley, M. A., et al. (2006). A link between terrestrial gamma-ray flashes and intracloud lightning discharges. *Geophysical Research Letters*, *33*(6). (L06803) doi: 10.1029/2005GL025537

Stock, M. G., et al. (2014). Continuous broadband digital interferometry of lightning using a generalized cross-correlation algorithm. *Journal of Geophysical Research: Atmospheres*, *119*(6), 3134-3165. doi: 10.1002/2013JD020217

Stolzenburg, M., Marshall, T. C., Karunarathne, S., & Orville, R. E. (2016). Luminosity with intracloud-type lightning initial breakdown pulses and terrestrial gamma-ray flash candidates. *Journal of Geophysical Research: Atmospheres*, *121*, 10919-10936. doi: 10.1002/2016JD025202

Stolzenburg, M., et al. (2013). Luminosity of initial breakdown in lightning. *Journal of Geophysical Research*, *118*, 2918-2937. doi: 10.1002/jgrd.50276

Stolzenburg, M., et al. (2014). Leader observations during the initial breakdown stage of a lightning flash. *Journal of Geophysical Research: Atmospheres*, *119*(21), 12,198-12,221. doi: 10.1002/2014JD021994

Thomas, R. J., et al. (2004). Accuracy of the Lightning Mapping Array. *Journal of Geophysical Research: Atmospheres*, *109*(D14). doi: 10.1029/2004JD004549

Tilles, J. (2020). *Broadband radio mapping and imaging of lightning processes.* PhD thesis, University of New Hampshire.

Tilles, J., et al. (2019). Fast negative breakdown in thunderstorms. *Nature Communications*, *10*, 1648. doi: 10.1038/s41467-019-09621-z

Tilles, J., et al. (2020). Radio interferometer observations of an energetic in-cloud pulse reveal large currents generated by relativistic discharges. *Journal of Geophysical Research: Atmospheres*. doi: 10.1029/2020JD032603

Tran, M., et al. (2015). A terrestrial gamma-ray flash recorded at the lightning observatory in Gainsville, Florida. *Journal of Atmospheric and Solar-Terrestrial Physics*, *136*, 86. doi: 10.1016/j.jastp.2015.10.010

Wada, Y., et al. (2019). Gamma-ray glow preceding downward terrestrial gamma-ray flash. *Physics Communications*, *2*(67). doi: 10.1038/s42005-019-0168-y

Weidman, C. D., & Krider, E. P. (1979). The radiation field waveforms produced by

intracloud lightning discharge processes. *Journal of Geophysical Research*, *84*, 3159. doi: 10.1029/JC084iC06p03159

Winn, W. P., et al. (2011). Lightning leader stepping, K changes, and other observations near an intracloud flash. *Journal of Geophysical Research: Atmospheres*, *116*(D23). doi: 10.1029/2011JD015998

Zyla, P., et al. (2020). Particle data group. *Progress of Theoretical and Experimental Physics*(083C01 (2020)). Retrieved from `http://pdg.lbl.gov/2020/reviews/rpp2020-rev-passage-particles-matter.pdf`

Supporting Information for "Observations of the Origin of Downward Terrestrial Gamma-Ray Flashes"

J.W. Belz[1], P.R. Krehbiel[2], J. Remington[1], M.A. Stanley[2], R.U. Abbasi[3], R. LeVon[1], W. Rison[2], D. Rodeheffer[2]

and the Telescope Array Scientific Collaboration

T. Abu-Zayyad[1], M. Allen[1], E. Barcikowski[1], D.R. Bergman[1], S.A. Blake[1], M. Byrne[1], R. Cady[1], B.G. Cheon[6], M. Chikawa[8], A. di Matteo[9*], T. Fujii[10], K. Fujita[11], R. Fujiwara[11], M. Fukushima[12,13], G. Furlich[1], W. Hanlon[1], M. Hayashi[14], Y. Hayashi[11], N. Hayashida[15], K. Hibino[15], K. Honda[16], D. Ikeda[17], T. Inadomi[18], N. Inoue[4], T. Ishii[16], H. Ito[19], D. Ivanov[1], H. Iwakura[18], H.M. Jeong[20], S. Jeong[20], C.C.H. Jui[1], K. Kadota[21], F. Kakimoto[5], O. Kalashev[22], K.Kasahara[23], S. Kasami[24], H. Kawai[25], S. Kawakami[11], K. Kawata[12], E. Kido[12], H.B. Kim[6], J.H. Kim[1], J.H. Kim[11], V. Kuzmin[22†], M. Kuznetsov[9,22], Y.J. Kwon[26], K.H. Lee[20], B. Lubsandorzhiev[22], J.P. Lundquist[1], K. Machida[16], H. Matsumiya[11], J.N. Matthews[1], T. Matuyama[11], R. Mayta[11], M. Minamino[11], K. Mukai[16], I. Myers[1], S. Nagataki[19], K. Nakai[11], R. Nakamura[18], T. Nakamura[27], Y. Nakamura[18], T. Nonaka[12], H. Oda[11], S. Ogio[11,28], M.Ohnishi[12], H. Ohoka[12], Y. Oku[24], T. Okuda[29], Y. Omura[11], M. Ono[19], A. Oshima[36], S. Ozawa[23], I.H. Park[20],M. Potts[1], M.S. Pshirkov[22,30], D.C. Rodriguez[1], G. Rubtsov[22], D. Ryu[31], H. Sagawa[12], R. Sahara[11], K. Saito[12], Y. Saito[18], N. Sakaki[12], T. Sako[12], N. Sakurai[11], K. Sano[18], T. Seki[18], K. Sekino[12], F. Shibata[16], T. Shibata[12], H. Shimodaira[12], B.K. Shin[11], H.S. Shin[12], J.D. Smith[1], P. Sokolsky[1], N. Sone[18], B.T. Stokes[1], T.A. Stroman[1], Y. Takagi[11], Y. Takahashi[11], M. Takeda[12], R. Takeishi[20], A. Taketa[17], M. Takita[12], Y. Tameda[24], K. Tanaka[32], M. Tanaka[33], Y. Tanoue[11], S.B. Thomas[1], G.B. Thomson[1], P. Tinyakov[9,22], I. Tkachev[22], H. Tokuno[5], T. Tomida[18], S. Troitsky[22], Y. Tsunesada[11,28], Y. Uchihori[34], S. Udo[15], T. Uehama[18],

F. Urban[35], T. Wong[1], M. Yamamoto[18], H. Yamaoka[33], K. Yamazaki[36], K. Yashiro[7], M. Yosei[24], H. Yoshii[37], Y. Zhezher[12,22], Z. Zundel[1]

[1]Department of Physics and Astronomy, University of Utah, Salt Lake City, Utah, USA

[2]Langmuir Laboratory for Atmospheric Research, New Mexico Institute of Mining and Technology, Socorro, NM, USA

[3]Department of Physics, Loyola University Chicago, Chicago, Illinois, USA

[4]The Graduate School of Science and Engineering, Saitama University, Saitama, Saitama, Japan

[5]Graduate School of Science and Engineering, Tokyo Institute of Technology, Meguro, Tokyo, Japan

[6]Department of Physics and The Research Institute of Natural Science, Hanyang University, Seongdong-gu, Seoul, Korea

[7]Department of Physics, Tokyo University of Science, Noda, Chiba, Japan

[8]Department of Physics, Kindai University, Higashi Osaka, Osaka, Japan

[9]Service de Physique Théorique, Université Libre de Bruxelles, Brussels, Belgium

[10]The Hakubi Center for Advanced Research, Kyoto University, Kitashirakawa-Oiwakecho, Sakyo-ku, Kyoto, Japan

[11]Graduate School of Science, Osaka City University, Osaka, Osaka, Japan

[12]Institute for Cosmic Ray Research, University of Tokyo, Kashiwa, Chiba, Japan

[13]Kavli Institute for the Physics and Mathematics of the Universe (WPI), University of Tokyo, Kashiwa, Chiba, Japan

[14]Information Engineering Graduate School of Science and Technology, Shinshu University, Nagano, Nagano, Japan

[15]Faculty of Engineering, Kanagawa University, Yokohama, Kanagawa, Japan

[16]Interdisciplinary Graduate School of Medicine and Engineering, University of Yamanashi, Kofu, Yamanashi, Japan

[17]Earthquake Research Institute, University of Tokyo, Bunkyo-ku, Tokyo, Japan

[18]Academic Assembly School of Science and Technology Institute of Engineering, Shinshu University, Nagano, Nagano, Japan

[19]Astrophysical Big Bang Laboratory, RIKEN, Wako, Saitama, Japan

[20]Department of Physics, Sungkyunkwan University, Jang-an-gu, Suwon, Korea

[21]Department of Physics, Tokyo City University, Setagaya-ku, Tokyo, Japan

[22]Institute for Nuclear Research of the Russian Academy of Sciences, Moscow, Russia

[23]Advanced Research Institute for Science and Engineering, Waseda University, Shinjuku-ku, Tokyo, Japan

[24]Department of Engineering Science, Faculty of Engineering, Osaka Electro-Communication University, Neyagawa-shi, Osaka, Japan

[25]Department of Physics, Chiba University, Chiba, Chiba, Japan

[26]Department of Physics, Yonsei University, Seodaemun-gu, Seoul, Korea

[27]Faculty of Science, Kochi University, Kochi, Kochi, Japan

[28]Nambu Yoichiro Institute of Theoretical and Experimental Physics, Osaka City University, Osaka, Osaka, Japan

[29]Department of Physical Sciences, Ritsumeikan University, Kusatsu, Shiga, Japan

[30]Sternberg Astronomical Institute, Moscow M.V. Lomonosov State University, Moscow, Russia

[31]Department of Physics, Ulsan National Institute of Science and Technology, UNIST-gil, Ulsan, Korea

[32]Graduate School of Information Sciences, Hiroshima City University, Hiroshima, Hiroshima, Japan

[33]Institute of Particle and Nuclear Studies, KEK, Tsukuba, Ibaraki, Japan

[34]National Institute of Radiological Science, Chiba, Chiba, Japan

[35]CEICO, Institute of Physics, Czech Academy of Sciences, Prague, Czech Republic

[36]Department of Physics and Institute for the Early Universe, Ewha Womans University, Seodaaemun-gu, Seoul, Korea

[37]Department of Physics, Ehime University, Matsuyama, Ehime, Japan

[†]deceased

[*]Currently at INFN, sezione di Torino, Turin, Italy, T. Fujii

Contents of this file

1. Figures S1 to S31

2. Tables S1 to S3

Introduction

The tables and figures in this supporting document provide further detail on the Terrestrial Gamma-Ray Flash (TGF) observations by the Telescope Array Surface Detector (TASD), Lightning Mapping Array (LMA), fast electric field change antenna (FA), and VHF interferometer (INTF).

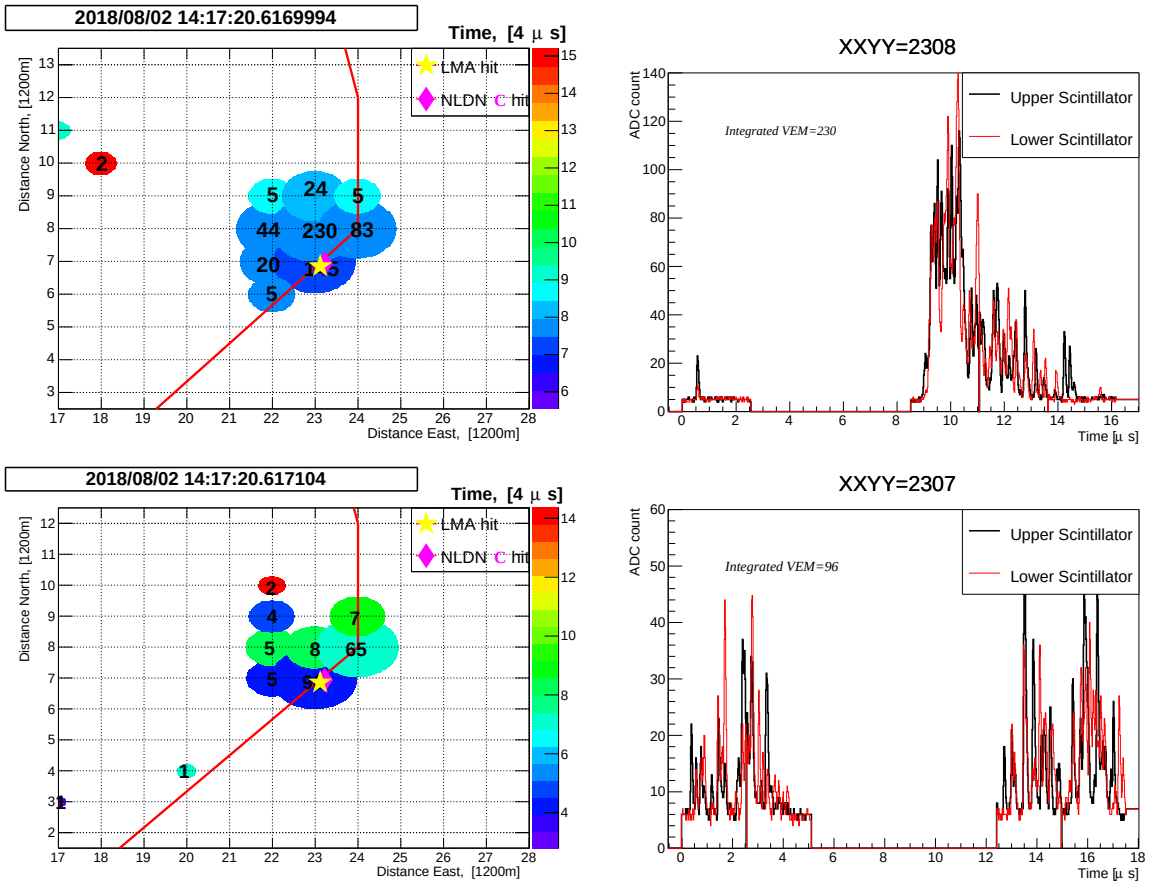

Figure S1. TASD observations for TGF A. Footprints for the two triggers of TGF A and the waveforms at the TASD recording the strongest energy deposit. Numbers in the footprint circles indicate the VEM energy deposit, and color indicates the relative onset times (4 μs intervals). The yellow star indicates the median plan location of the LMA sources within $\pm$1 ms of the gamma burst. The magenta diamond indicates the NLDN event corresponding the TGF sferic or the one closest in time prior to the TGF (see Table S1). Both events occurred over the edge of southeastern TASD boundary (red line).

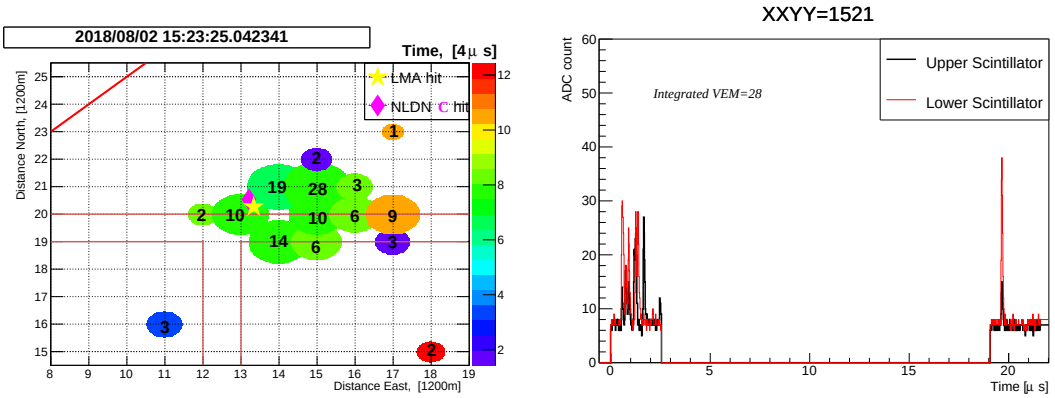

Figure S2. TASD observations for TGF B. Same as Figure S1, except for the single trigger of TGF B. The TGF was detected at four different TASDs or sets of TASDs at different onset times, beginning with TASD 1421 immediately NE of the LMA- and NLDN-indicated source location, and continuing in a rapid succession around a central annular hole to the eastern, southern, and finally western station, finishing up almost directly around the TGF's source. TASD 1420 associated with the annular hole did not record a trigger, indicating the gamma bursts were relatively well-beamed (the station was fully operational throughout the storm and was active for a cosmic ray event later in the day).

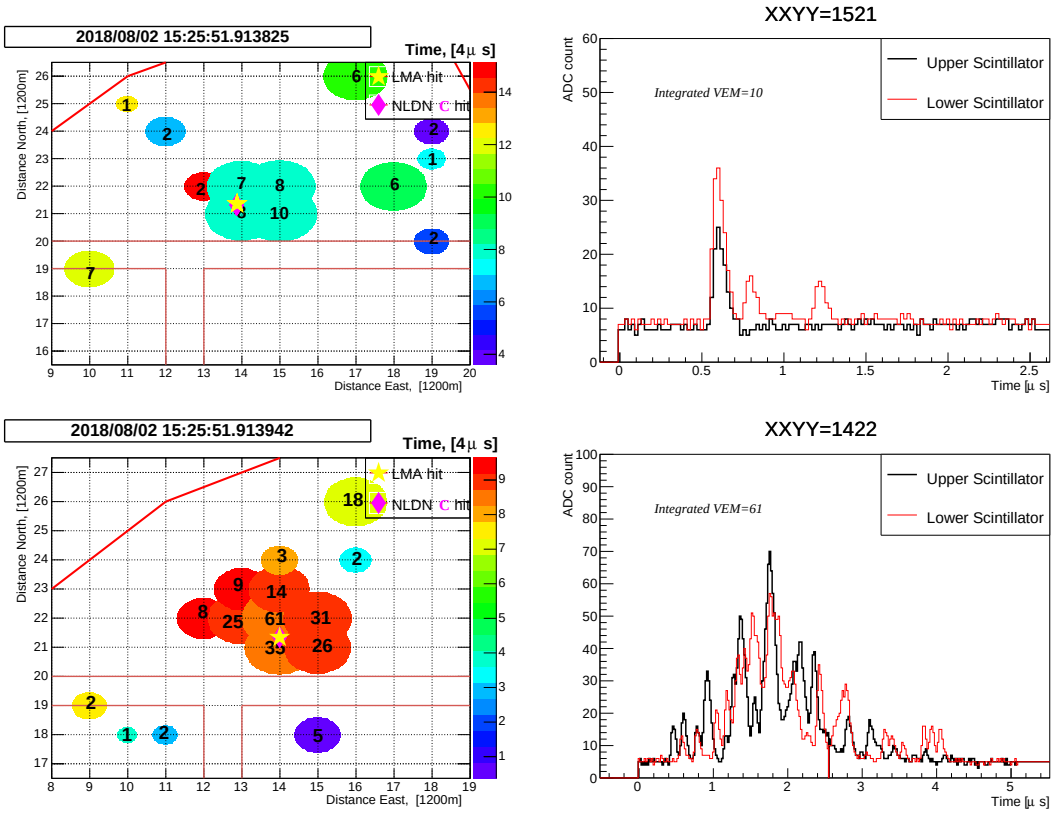

Figure S3. TASD observations for TGF C. Same as Figure S1, except for two gamma bursts/triggers of TGF C. Both events were canonical examples of the basic processes involved in TGF production (see text at end of Section 3.3). The zoomed-in views of the TASD signals in the right-hand panels illustrate the fact that the SDs are sensing individual Compton electrons, with first event of the top right panel corresponding to an electron that penetrated both the upper and lower layers, and therefore was produced by a gamma photon having a minimum energy of 6.4 MeV for rebounding collisions and a most likely energy up to three times that for grazing collisions (text at end of Section 3.1). The bottom right panel further illustrates the individual nature of detections and their quantization both in time and amplitude.The non-diagonal red lines of these footprints and the footprint of TGF B denote internal boundaries of different sub-sectors of the TASD.

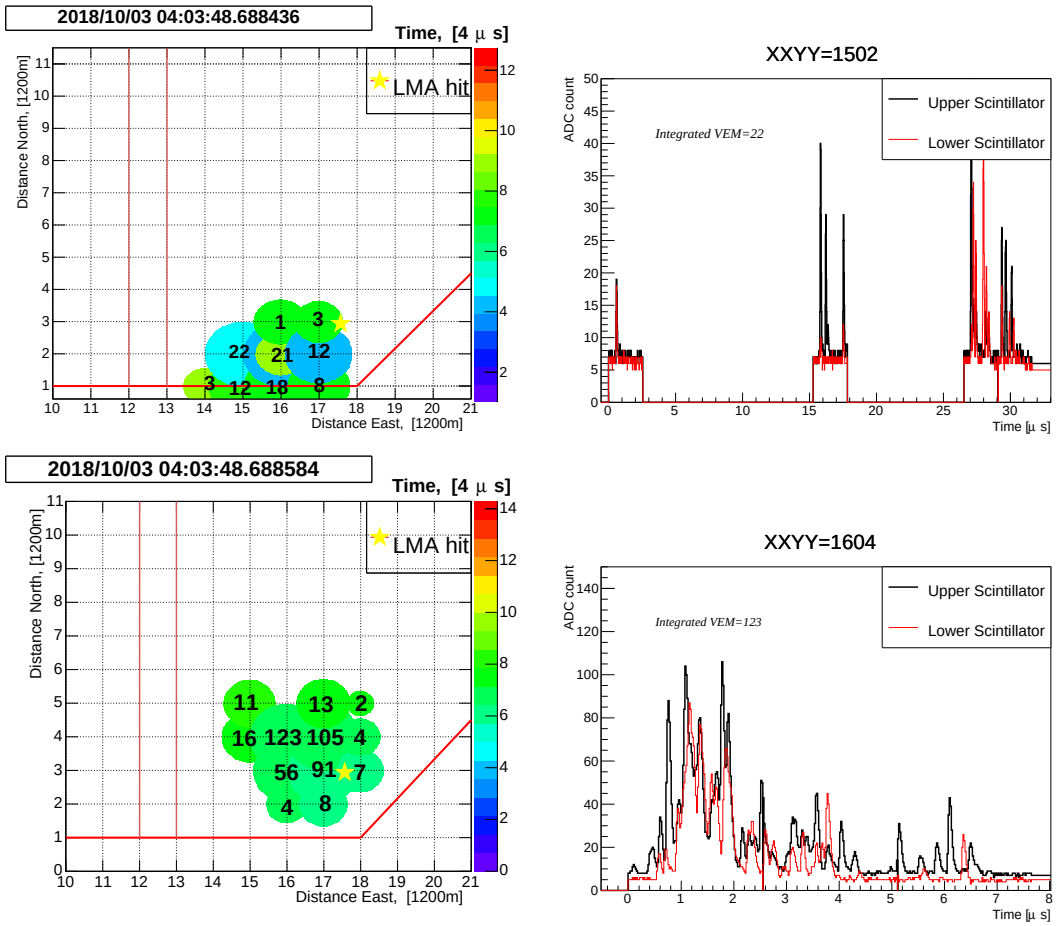

Figure S4. TASD observations for TGF D. Same as Figure S1, except for two trigger events of TGF D. This event occurred two months later in the season (Oct. 3) in a nighttime storm over the southern-most eastern corner of the TASD, and was less-well located by the LMA. It was a low-altitude IC flash whose downward development was strongly tilted from vertical (Figure S22 and Figure 5d of the main text). Rather than going to ground, the discharge terminated in a strong lower positive charge region of the storm, which was displaced to the northwest of the flash initiation point. The tilted development was also reflected in the TGF footprints, with the initial burst being southwest of the estimated source of the gamma bursts (and partially outside the TASD boundary). The second burst was tilted to the northwest, concomitant with the north-westward tilt of the flash's development in the INTF and LMA observations. The parent IBP of the main, second burst was the most extensive of the four TGFs, lasting $\simeq$15 μs and propagating over a distance of 240 m (Table S3).

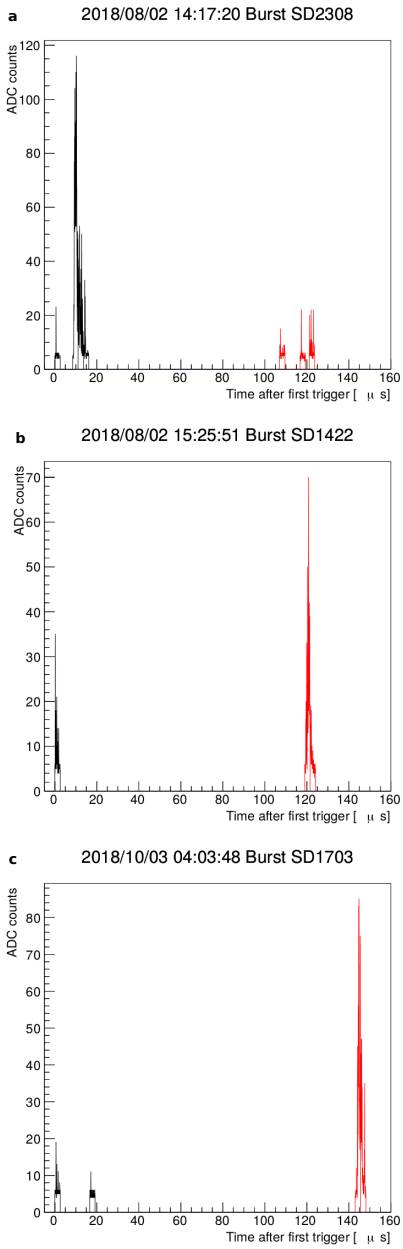

Figure S5. Composite TASD waveforms. Stitched-together waveforms for each of the TGFs that produced multiple triggers (TGFs A,C,D), showing their relative amplitudes and temporal separations. Triggers 1 and 2 are colored in black and red, respectively. The waveforms show the activity to be temporally resolved into discrete few-microsecond long bursts over a time period of $\simeq$100–150 μs. Three bursts occurred for TGF A, two for TGF C, three for TGF D, and one for TGF B (not shown). The multiple sporadic nature of the bursting is similar to that seen in the previous study by Abbasi et al., 2018.

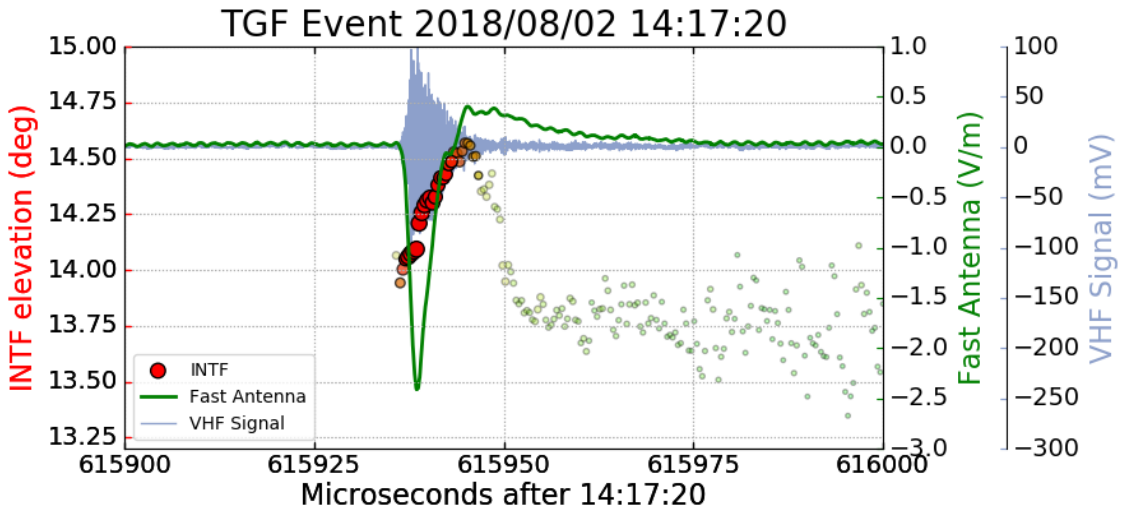

Figure S6. Initiating NBE of TGF A flash. Classic example of a narrow bipolar event produced by fast positive breakdown that initiated the flash of TGF A. The FPB propagated upward over a distance of 150 m in 11 μs, corresponding to a speed of 1.3×10^7 m/s. While the peak source powers of the VHF radiation of the NBE and IBP were indistinguishable (+27.6 dBW vs. +27.7 dBW, respectively), the sferic amplitude was 24 times stronger for the IBP than for the NBE (58 V/m vs. 2.4 V/m), being barely noticeable in Figure 3a of the main text. As a result of this difference, the NLDN detected the IBP sferic as having a peak current of –36.7 kA, but did not detect the initiating NBE sferic, whose peak current would have been only $\simeq$2 kA.

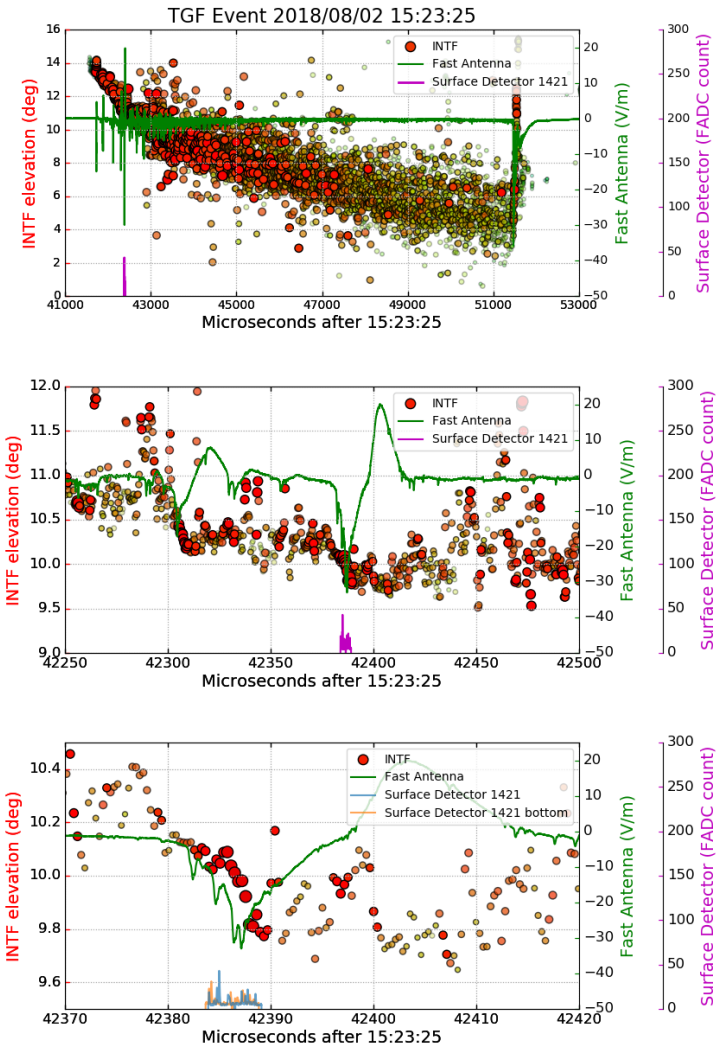

Figure S7. Observational data for TGF B. Observations of TGF B on 2018/08/02 at 15:23:25 UT. Panels show interferometer elevation versus time (circular dots), fast electric field sferic waveform (green curve) and TASD gamma detections (purple waveform). Top: Observations from initial breakdown through time of –26.5 kA initial cloud-to-ground stroke. Gamma ray detections occur in coincidence with strong (–30.1 kA) sferic pulse), 341 μs after flash start (Table S1). Middle: 250 μs of observations around the time of the gamma burst, showing the TGF's correlation with the largest amplitude initial breakdown pulse (IBP) and episode of downward fast negative breakdown (FNB). Bottom: Expanded 50 μs view of the scintillator waveforms at TASD 1421, which detected the initial onset of the TGF, showing how the strong gamma peak was associated with the second leading-edge, strong sub-pulse of the IBP.

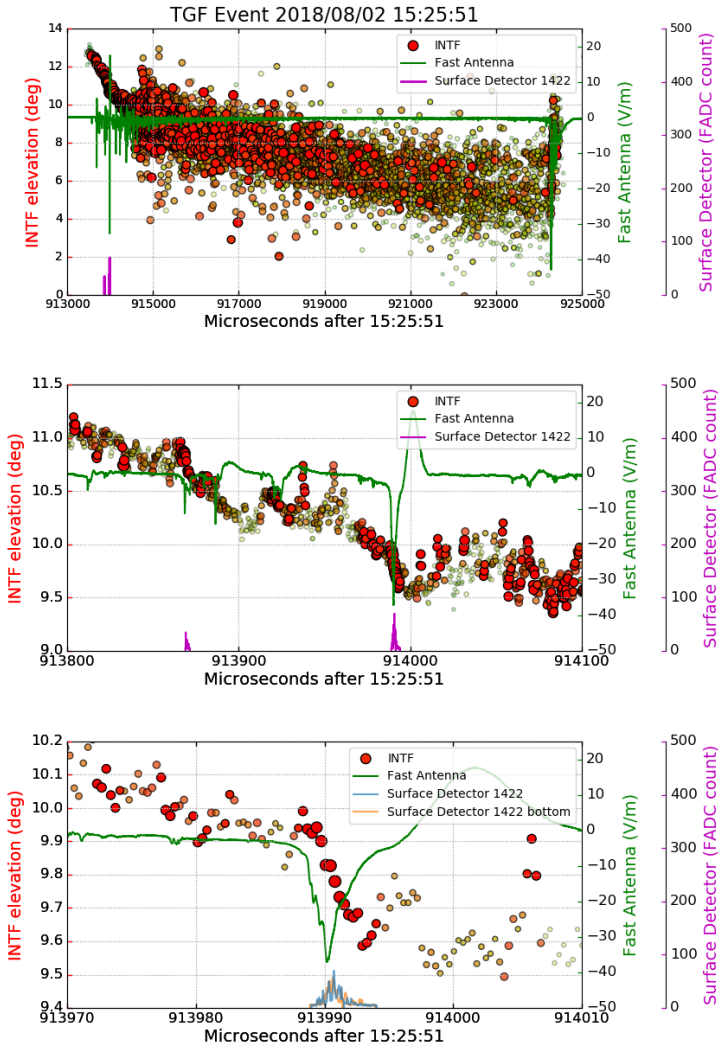

Figure S8. Observational data for TGF C. Same as Figure S7, except for TGF C on 2018/08/02 at 15:25:51 UT. In this case, two gamma bursts were produced 825 and 942 μs after flash start. While the main, second burst was associated with a –21.7 kA sferic, again comparable to the initial return stroke (–26.8 kA), the first burst was associated with a weaker sferic, but with a similarly embedded episode of enhanced-speed negative breakdown (Figure S12f). The correlation with FNB is seen in more detail in the bottom panel, which illustrates the FNB being initiated by upward positive VHF development at the beginning of the IBP—a characteristic feature of FNB —and the gamma detection steadily increasing during the FNB.

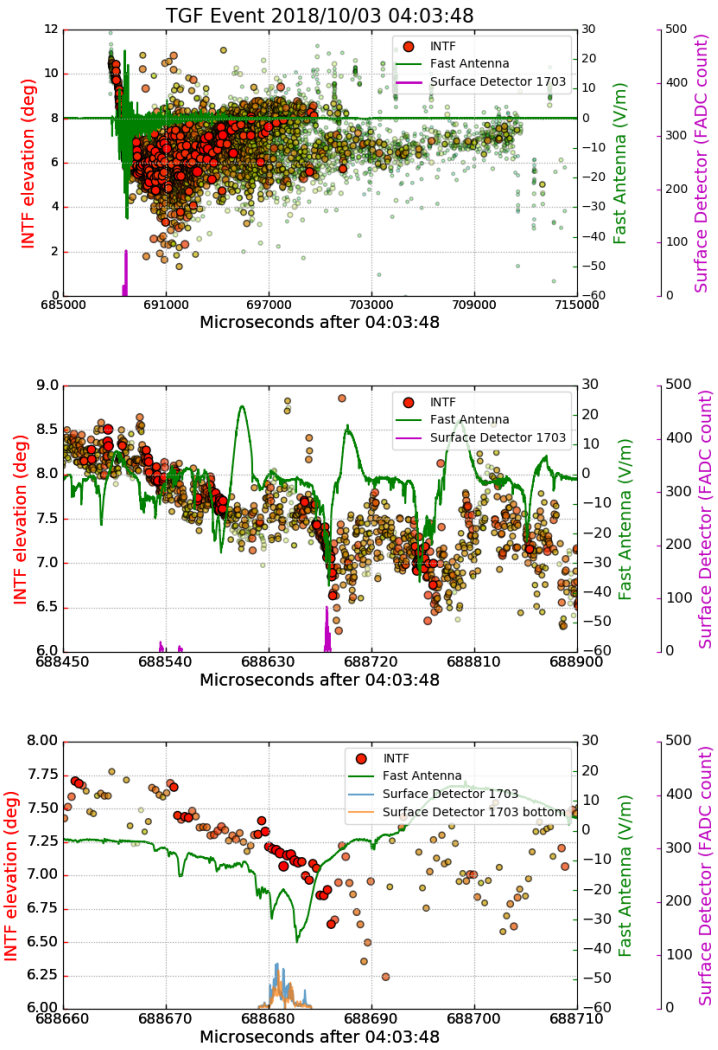

Figure S9. Observational data for TGF D. Same as Figure S7, except for TGF D on 2018/10/03 at 04:03:48 UT. As in TGF C, two weak gamma bursts occurred in connection with relatively weak IBP sferics (in this case, prior to the main burst, around 688,540 μs in middle panel), but not in stronger sferics both before and after the strongest sferic. The distinguishing characteristic appears to have been that the other IBPs did not have embedded episodes of enhanced-speed FNB. Again, the main gamma burst was associated with a strong sub-pulse on the leading edge of its IBP sferic (bottom panel).

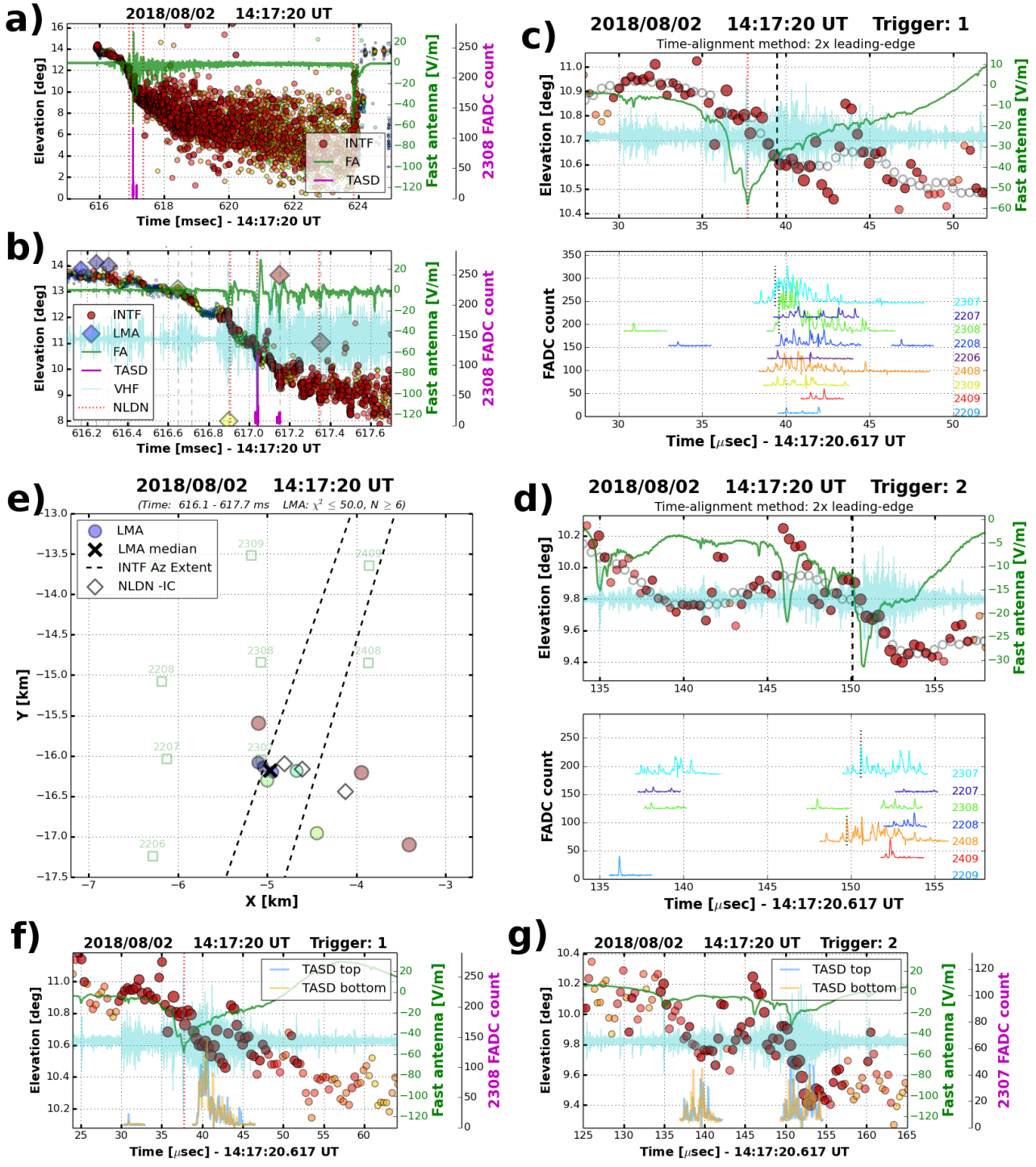

Figure S10. (Caption next page.)

Figure S10. (Previous page.) **Additional data for TGF A.** More complete summary results for TGF A, including observations for the two triggers and three gamma bursts of the TGF. **(a,b)** Overview plots similar to the top and middle panels of Figures S7–S9, except showing the times of NLDN detections (red dotted vertical lines) and (for panel b) times of LMA-located VHF sources (colored diamonds, when within the displayed range of elevation values), and the VHF time series waveform (cyan trace). **(c,d)** Correlation results from the alternative analysis process presented in the Methods section, illustrating time alignments obtained from the first point which exceeds half-maximum at the two TASD stations with the strongest signals (short vertical dotted lines in the TASD waveform panels), with the average of the two results shown in the top panel (dashed vertical line in the upper panel and in Figure A1b of the main paper). (e) Plan view of LMA sources within ±0.8 ms of the TGF (circular dots) and the median plan location of the sources used as the estimate for the TGF location (bold black 'x'). Plot illustrates the clustering of LMA sources and independently-determined NLDN locations (diamonds) around the median. Dashed lines indicate the 5–95% boundaries of INTF azimuth angles within ±0.8 ms of the TGF. Light green squares are participating TASD locations. **(f,g)** Detailed observations and correlations for the two TASD triggers, showing waveforms from top and bottom scintillators at the most active TASD station. (Note perfect correlation of time-shifted –36.7 kA NLDN event with sferic peak of initial trigger, and consistent correlation with downward FNB episodes even for weak IBPs of second trigger.)

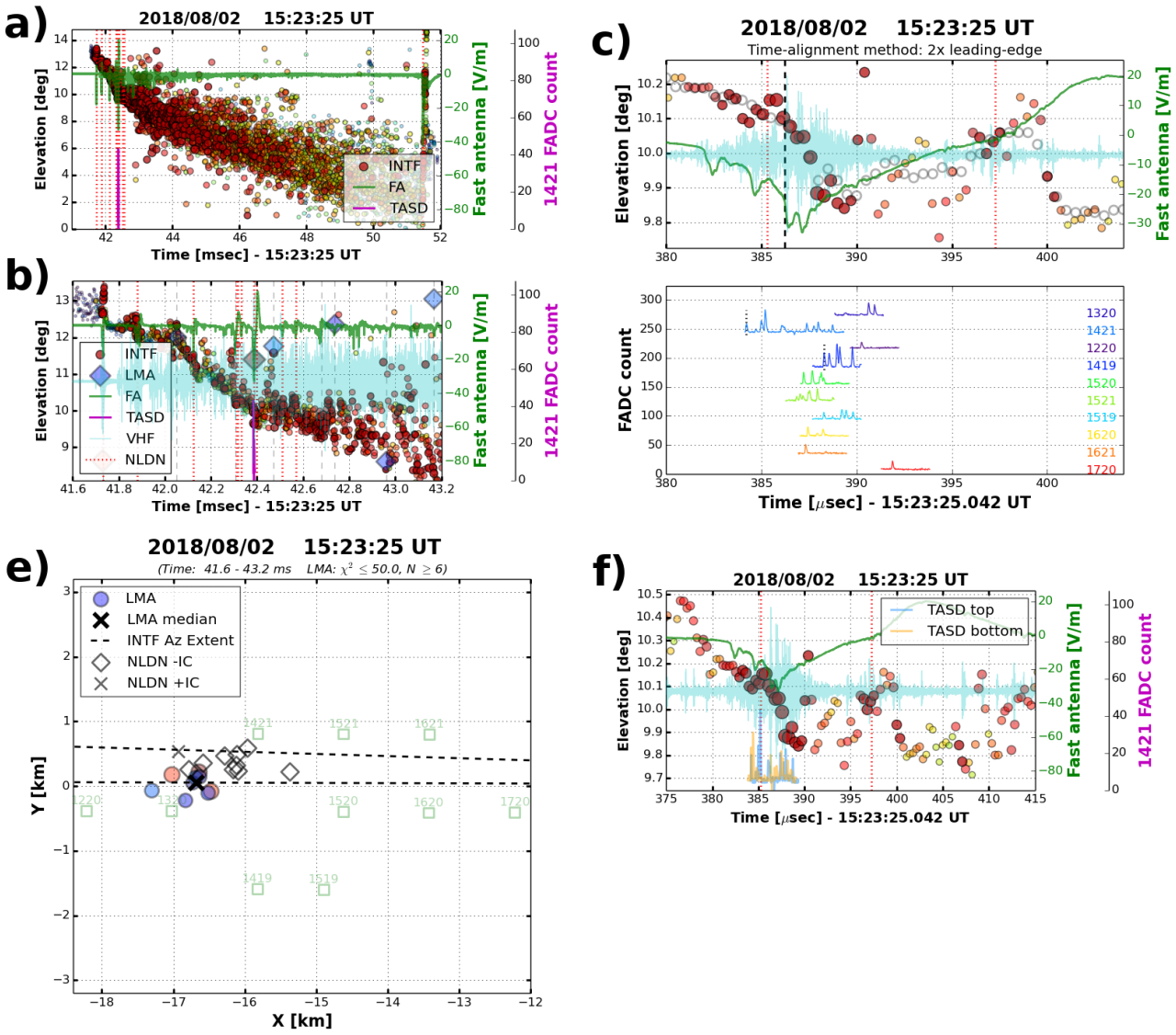

Figure S11. (Caption next page.)

Figure S11. (Previous page.) **Additional data for TGF B.** Same as Figure S10, except for the single trigger and burst of TGF B. Unfilled gray circles in panel c) indicate the 0.5 μs higher-time resolution observations of the INTF elevation angle observations used in both the iterative and alternative analysis procedures (see Methods Section A2). The TASD signals are sorted top to bottom according to increasing range from the source. Note the correlation in panel f) of the close 1421 TASD waveforms with the sferic sub-pulses and sequence of upward and downward FPB and FNB for the singular 1421-detected burst. The non-aligned TASD waveforms in panel c) reinforce multi-onset grouping seen in Figure 4d of the main text and the full-page version in Figure S16. Also note the large number of NLDN-located events in the first ms of the flash in panel a), and their excellent correlation with IBP sferics in panel b). The relatively large east-west variability of the NLDN events in panel e) is not reflected in the LMA observations and is presumably due to uncertainty in the NLDN location (caused by the particular NLDN stations used to locate the event). Otherwise, the LMA and NLDN sources are closely clustered around the LMA-indicated median source location.

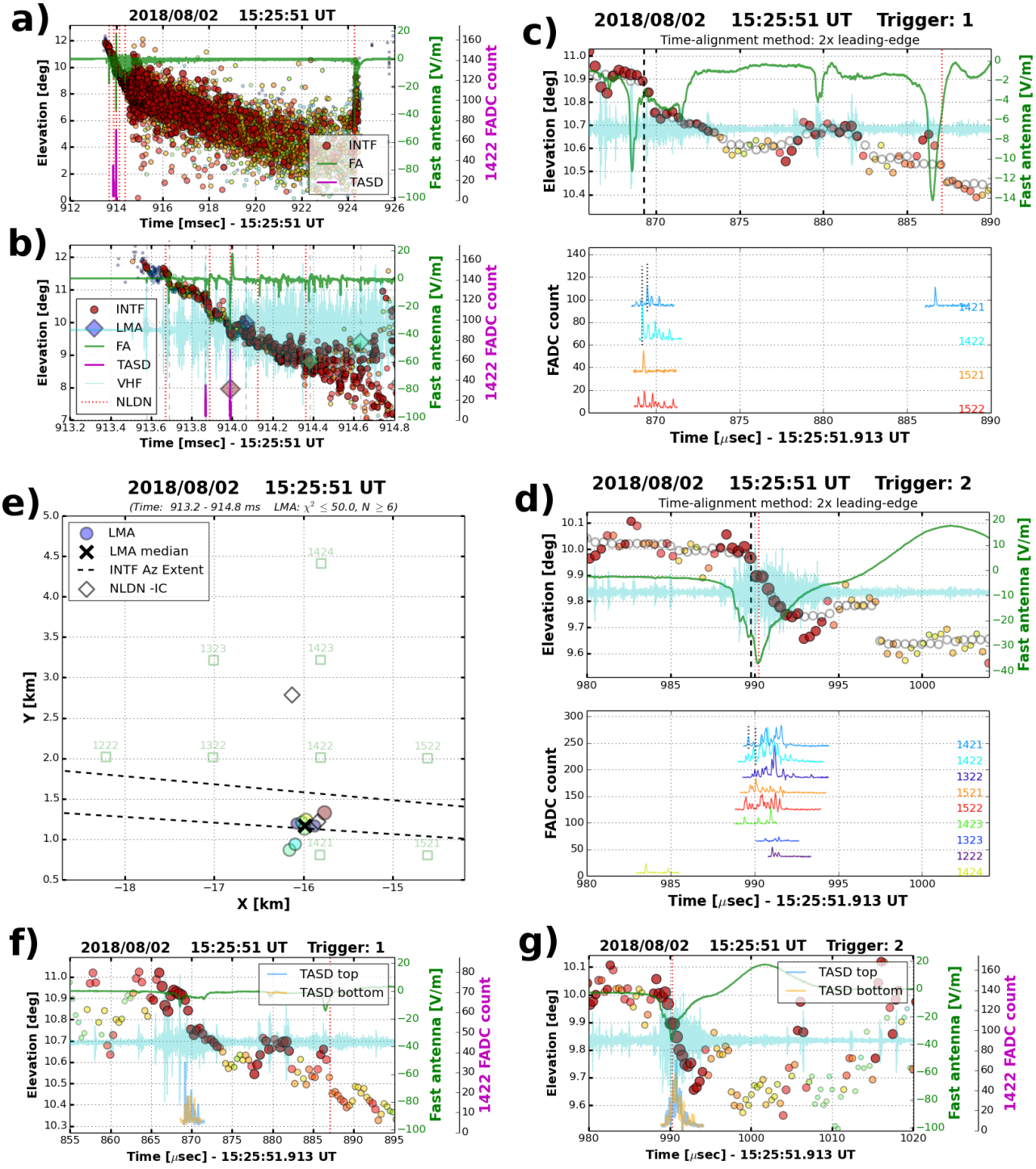

Figure S12. (Caption next page.)

Figure S12. (Previous page.) **Additional data for TGF C.** Same as Figure S10, except for the two triggers and bursts of TGF C. Again, the NLDN located a number of IBP events in the initial ms of the flash (panels a and b). One NLDN event was noticeably mislocated in an otherwise closely grouped set of LMA and NLDN events in the median plan location plot of panel (e). The main burst occurred during the second trigger and is notable for its simplicity of interpretation (see text). The alignment time is slightly delayed relative to the onset of the TASD 1422 signal by the use of a half-max threshold in the stepping analysis (multi-waveform part of panel d). The results are consistent with the iterative approach utilizing median result of all TASD stations(Figure 4c and associated main text) Accounting for the slight delay also better aligns the initial burst of the first trigger with its relatively weak sferic and associated VHF radiation (panel f).

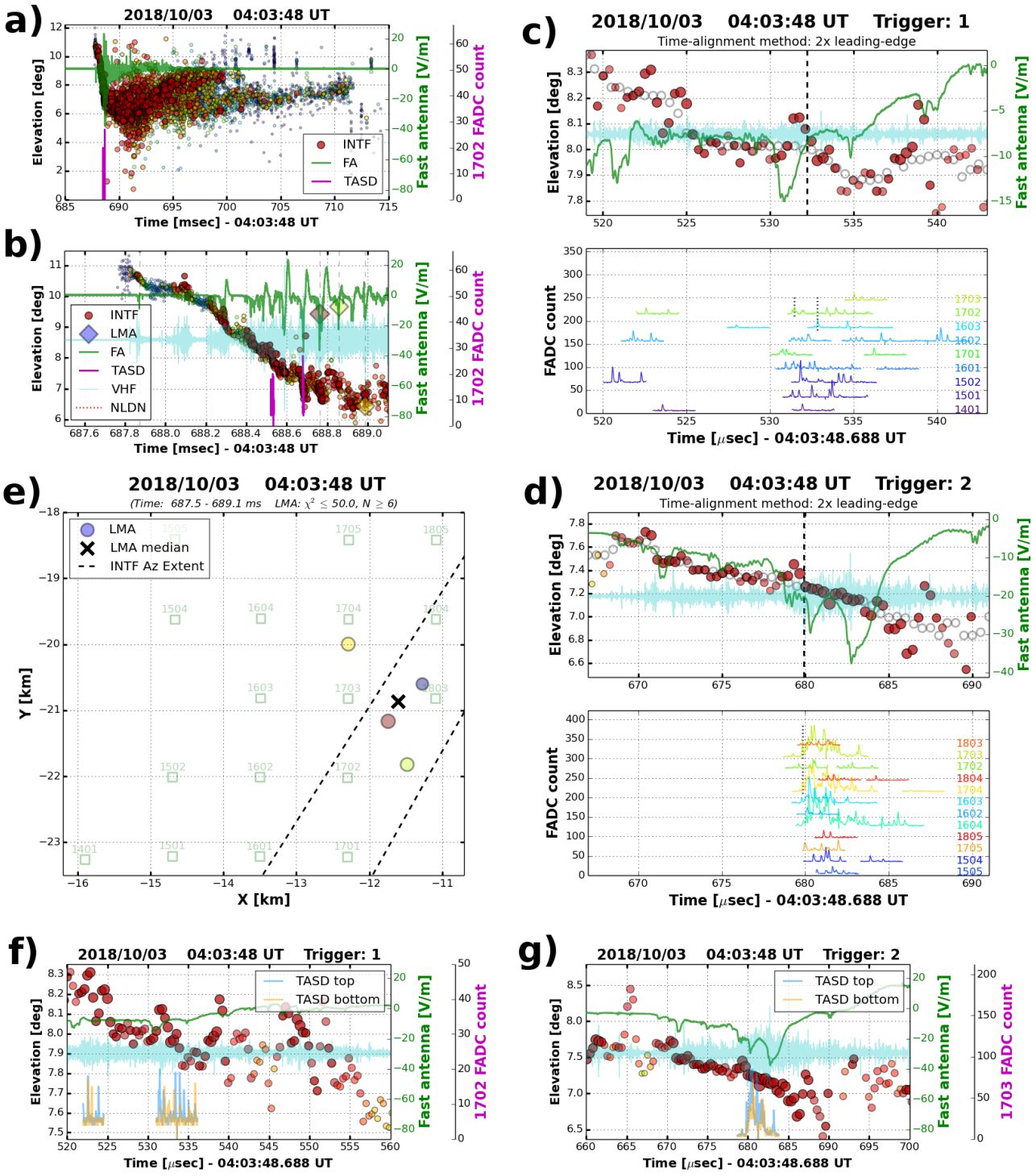

Figure S13. Caption next page.

Figure S13. (Previous Page.) **Additional data for TGF D.** Same as Figure S10, except for the two triggers and three bursts of TGF D. As discussed in connection with Figure S4, the flash did not go to ground and was not detected by the NLDN. Otherwise its initial breakdown was no different than that of a –CG discharge. Despite the increased uncertainty of the median plan location (panel e) and slightly greater plan distance from the INTF (24 km), both analysis methods gave essentially the same onset time for the main burst, which occurred during trigger 2 (panel d). In particular, the burst occurred in association with FNB associated with one or both sub-pulses of the IBP leading up to the main peak (panels d and g). The second of the two weaker bursts associated with the initial trigger was also associated with a slightly noisy but clear episode of downward FNB episode (and a weaker sferic) (panel f). The first burst was associated with even weaker and noisier activity, but was still capable of producing gamma radiation. In contrast, intermediate to strong IBPs between and after the two triggers did not produce detectable gamma bursts.

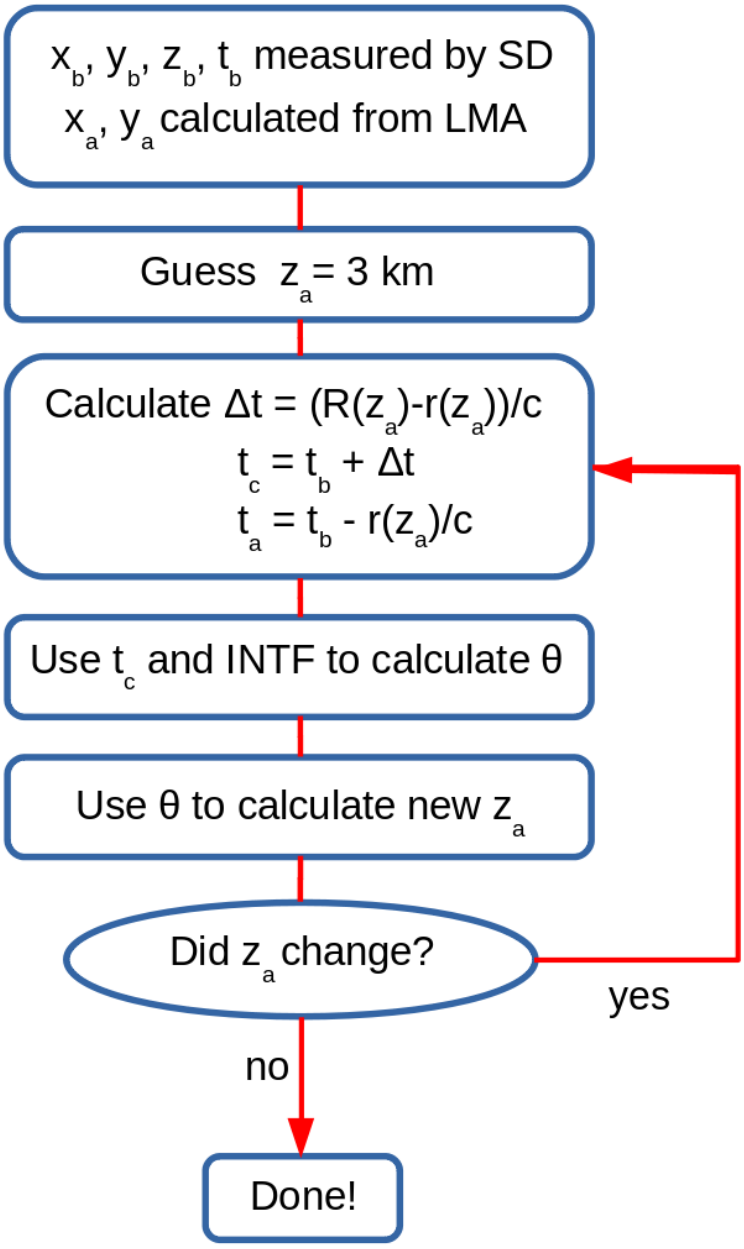

Figure S14. Source Reconstruction Flowchart. Iterative procedure for determining z_a and t_a, the altitude and time of the TGF source. Note that this is performed individually for each participating TASD station. See full description in Section 2.2 and in Methods Section A2.

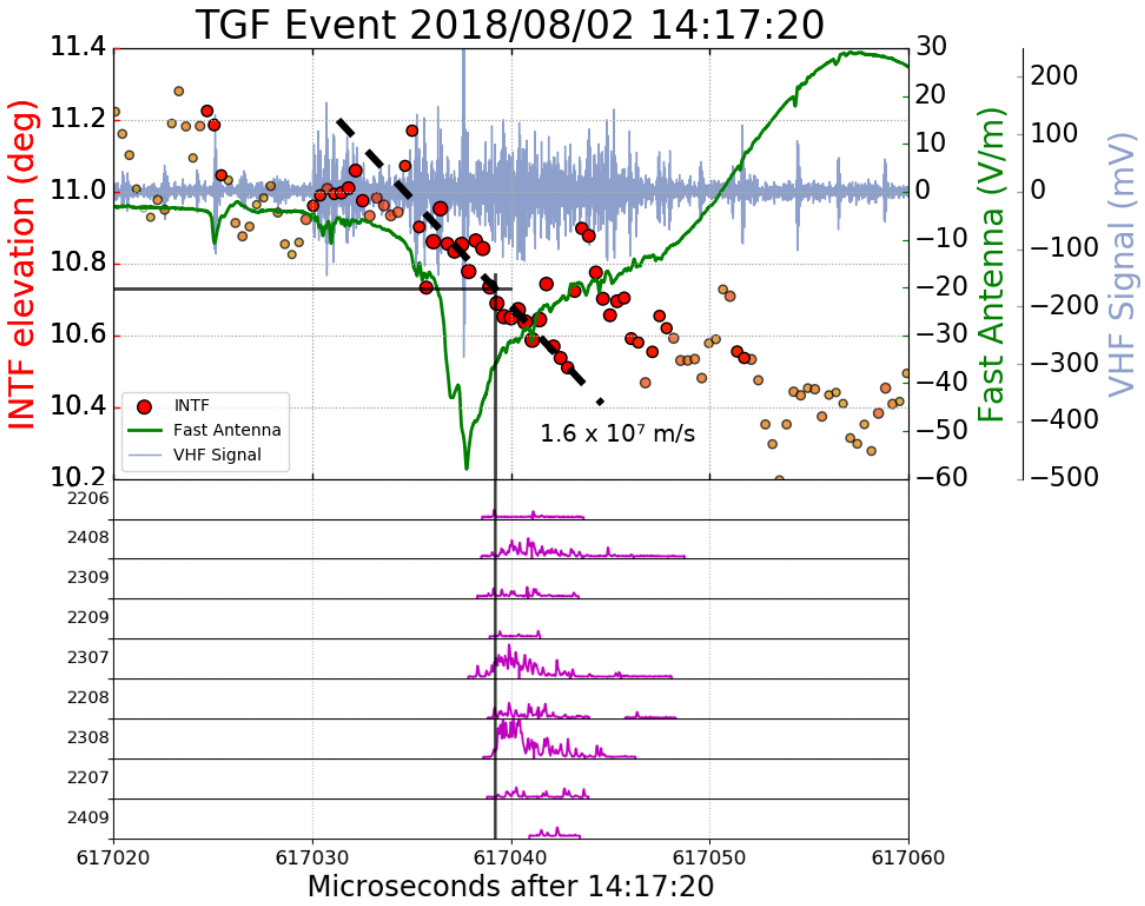

Figure S15. TASD correlations for TGF A. Enlarged view of panel a) of Figure 4 showing data from all participating detectors, time-shifted relative to the INTF. The black vertical line shows the median onset time of the TGF relative to the INTF and fast antenna data, and the black horizontal line shows the corresponding elevation angle. The light blue trace shows the VHF time series waveform observed by the INTF, and dots represent VHF radiation sources with color and size representing relative power. Purple traces in the lower panels are particle detector responses, with station numbers XXYY identifying their easterly (XX) and northerly (YY) locations within the array in 1.2 km grid spacing units. The detection times are in good agreement with one another as well as the median, indicating the onset time of the TGF during the sferic and the VHF radiation development.

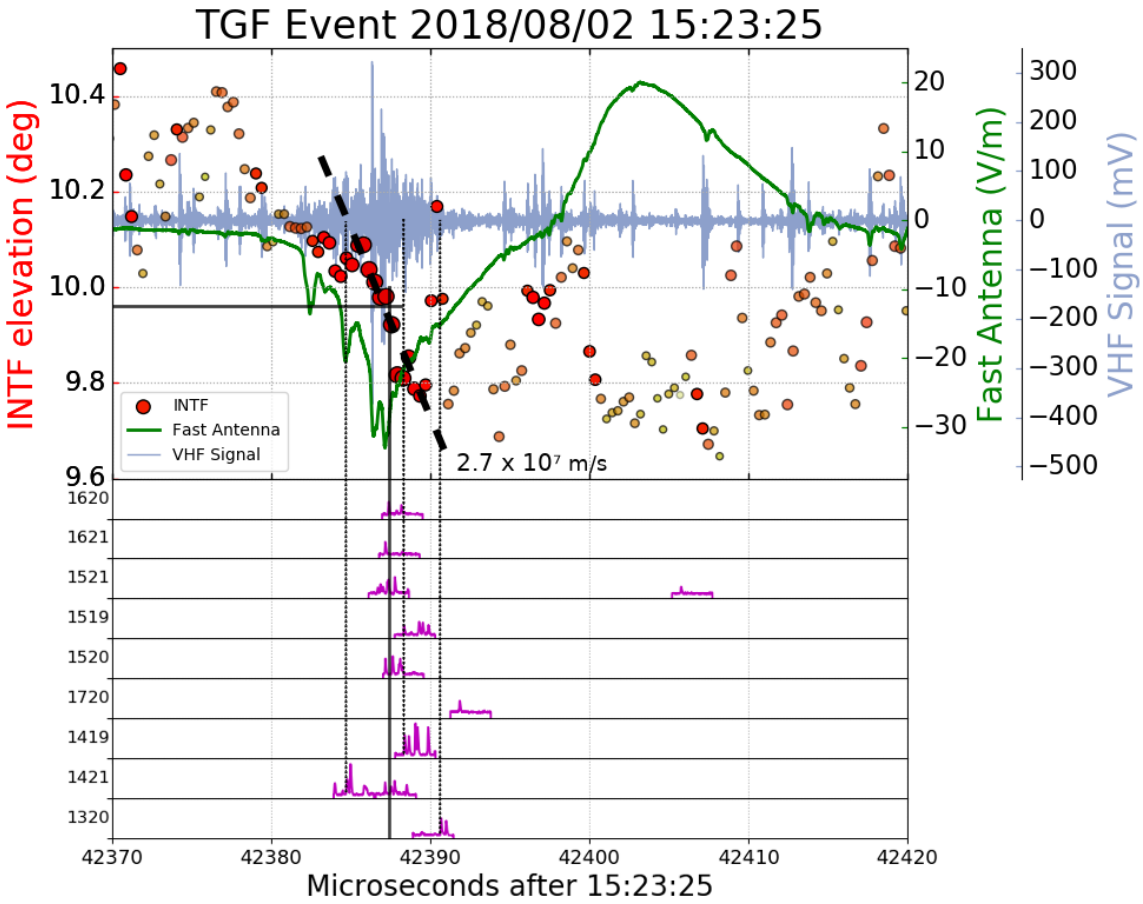

Figure S16. TASD correlations for TGF B. Same as Figure S15, except for panel b) of Figure 4. In contrast to the other TGFs, the TASD onset times are not all consistent with the median; TASD 1421 had a noticeably early onset time associated with the second strong sub-pulse, while the median onset was associated the peak of the IBP and with a step-discontinuity in the VHF radiation development. Slightly delayed TASD signals suggest additional onsets as discussed in Section 2.3.

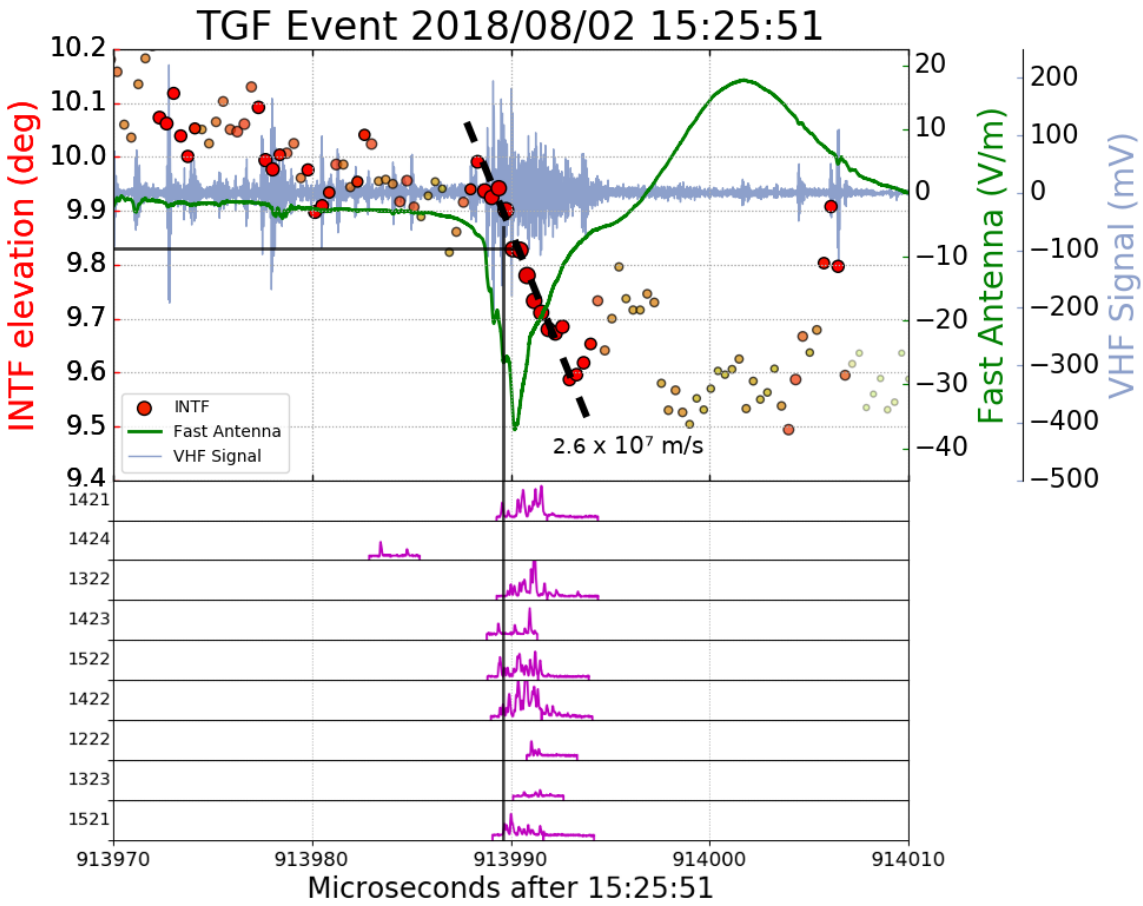

Figure S17. TASD correlations for TGF C. Same as Figure S15, except for panel c) of Figure 4. This event is an example of a simple, canonical IBP. Fast positive breakdown briefly propagates upward before turning into downward fast negative breakdown during the IBP. The TASD onsets are mostly in good agreement and are associated with a sub-pulse and a step-discontinuity in the VHF radiation development.

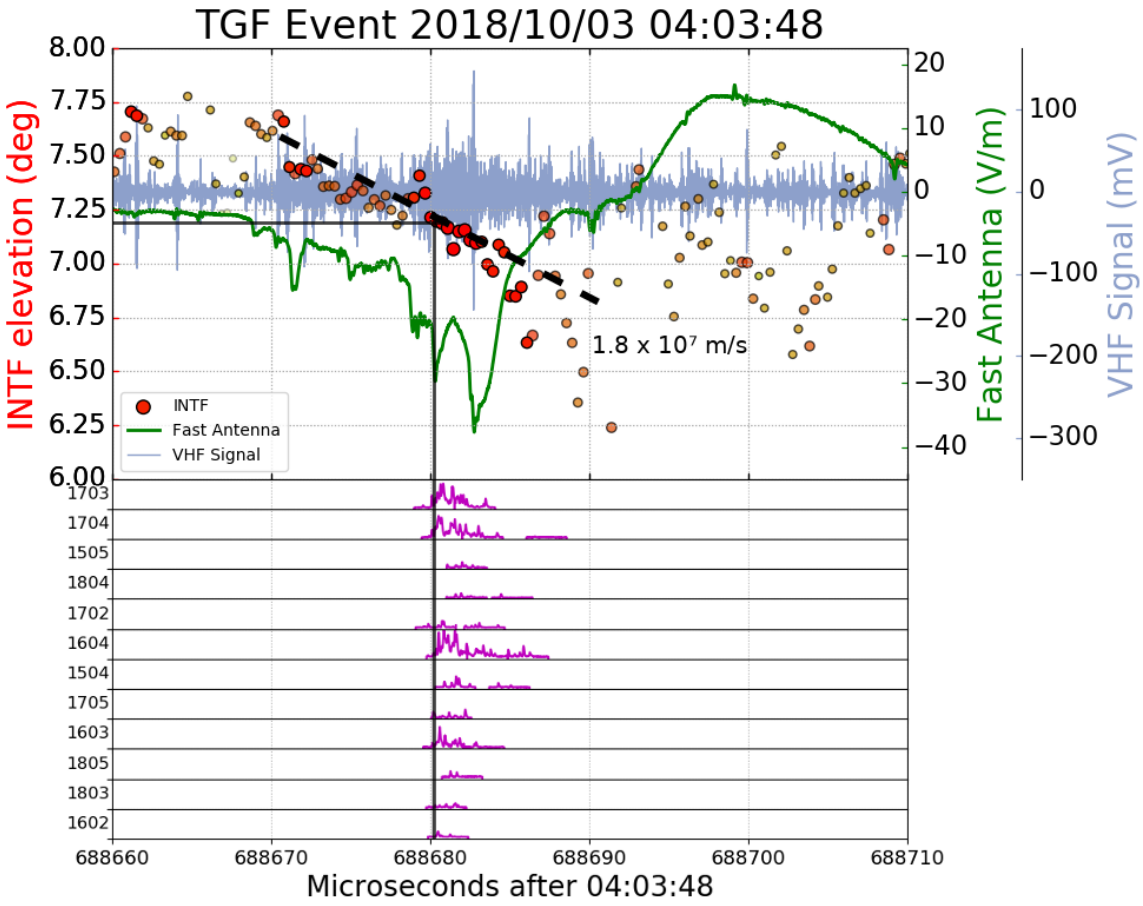

Figure S18. TASD correlations for TGF D. Same as Figure S15, except for panel d) of Figure 4. The sferic of this TGF is similar to that of TGF B, with a slower build-up and multiple embedded sub-pulses. The TASD onsets are closely correlated with one another and with a strong, impulsive sub-pulse before the main peak. The fast negative breakdown had a relatively long duration and extent (given in Table S3) with a step-discontinuity occurring immediately before the median TASD onset.

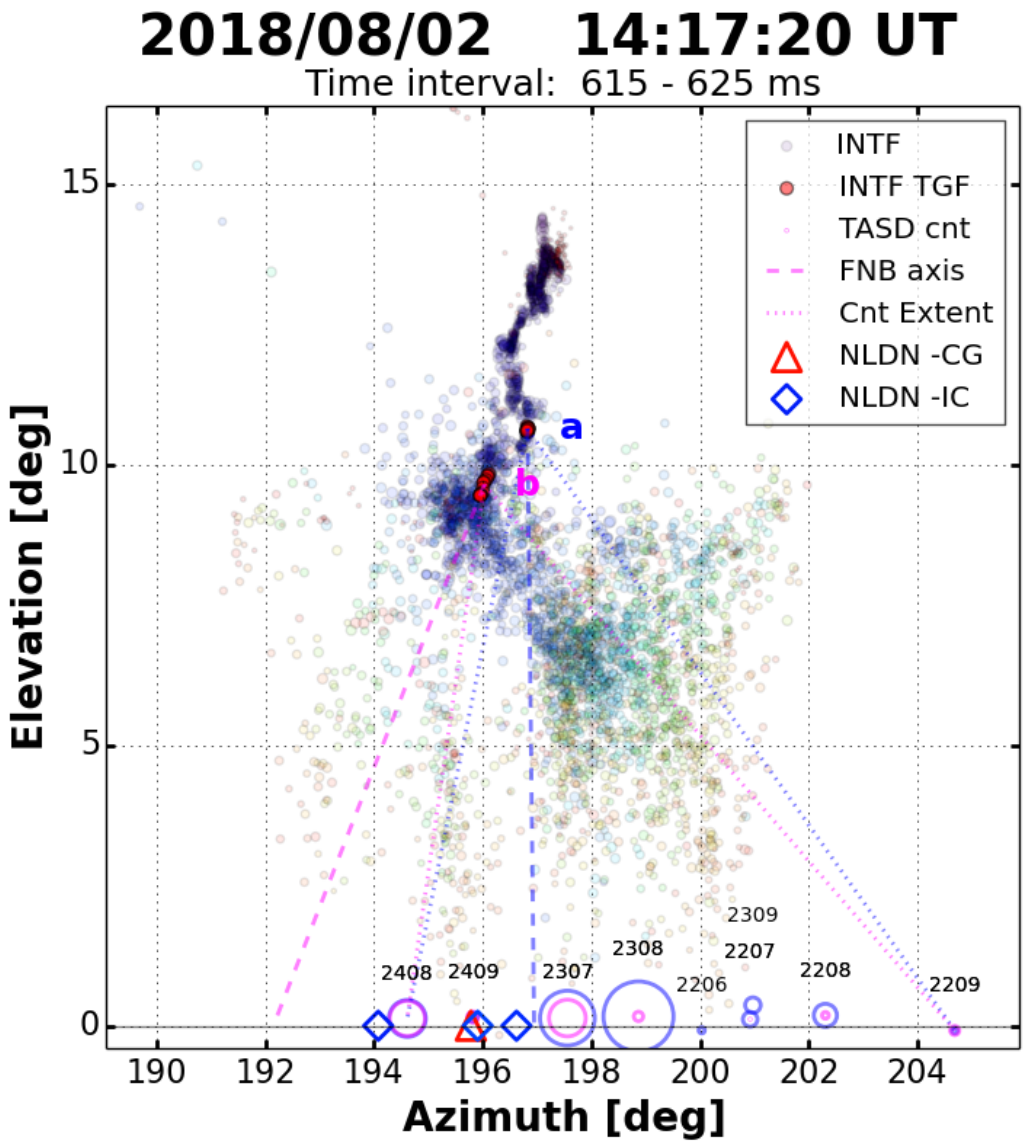

Figure S19. Azimuth-elevation plots for TGF A. Enlarged view of panel a) of Figure 5 showing the initial downward development leading up to and following the TGF occurrences. Red highlighted sources and *a*, *b* labels indicate the TGFs' calculated source locations. Dashed red and blue lines indicate the axes of the FNB associated with each TGF, while the finely dotted lines show the angular extent of the TASD surface detections. (The plot has a 1:1 aspect ratio so that the angular directions are faithfully replicated.) Baseline circles indicate size-scaled relative energy deposit in each Surface Detector; other baseline symbols indicate NLDN locations of CG and IC events, all as viewed from the INTF site.

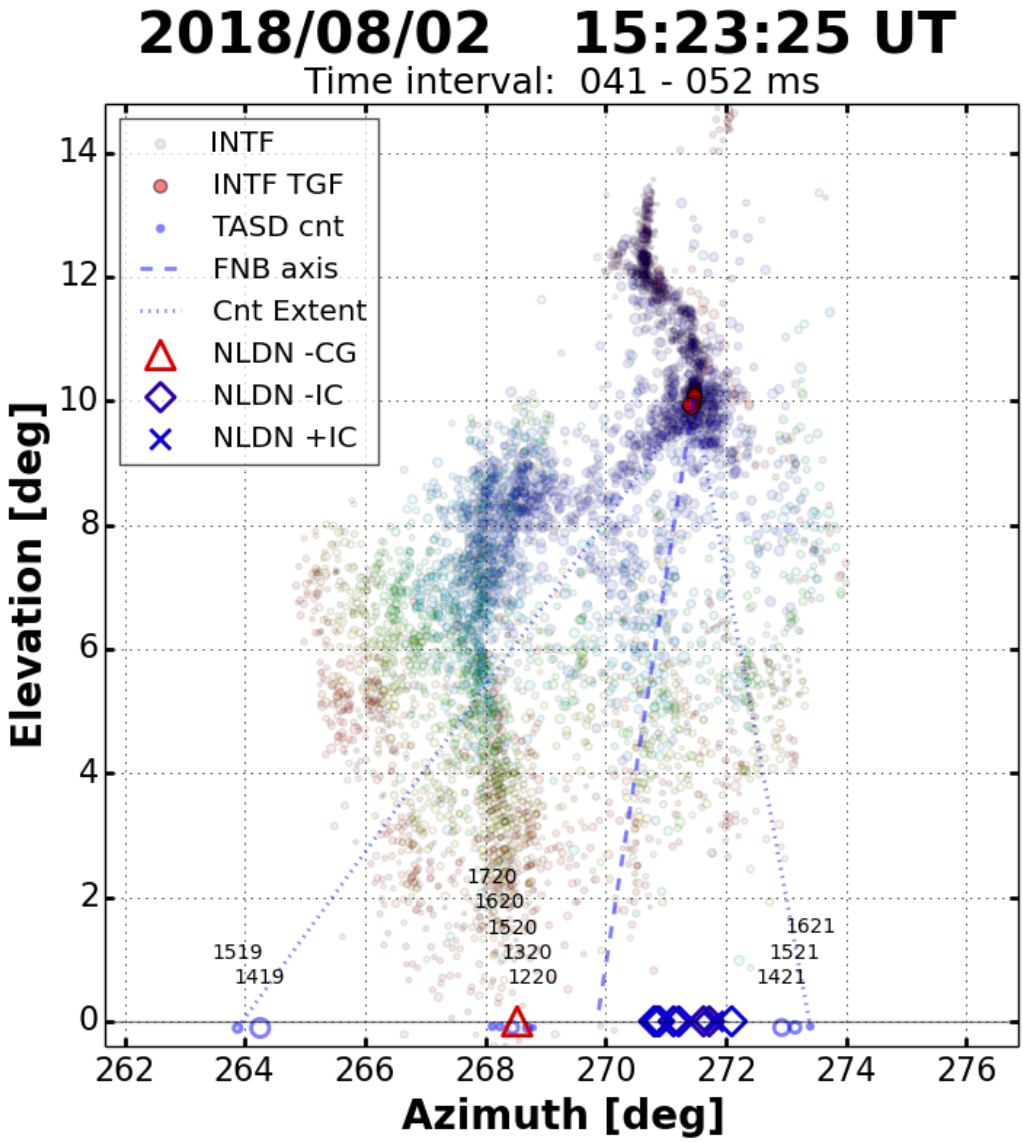

Figure S20. Azimuth-elevation plots for TGF B. Same as Fig. S19, except for TGF B of Figure 5b. This TGF had at least two onset times (and possibly one or two more) at different SDs and sets of SDs, and therefore narrower beaming than indicated by the overall angular extent (see Figure S16). This suggests successively different orientations of the sub-pulses and FNB activity, which would be consistent with INTF observations starting to broaden angular-wise at the IPBs location.

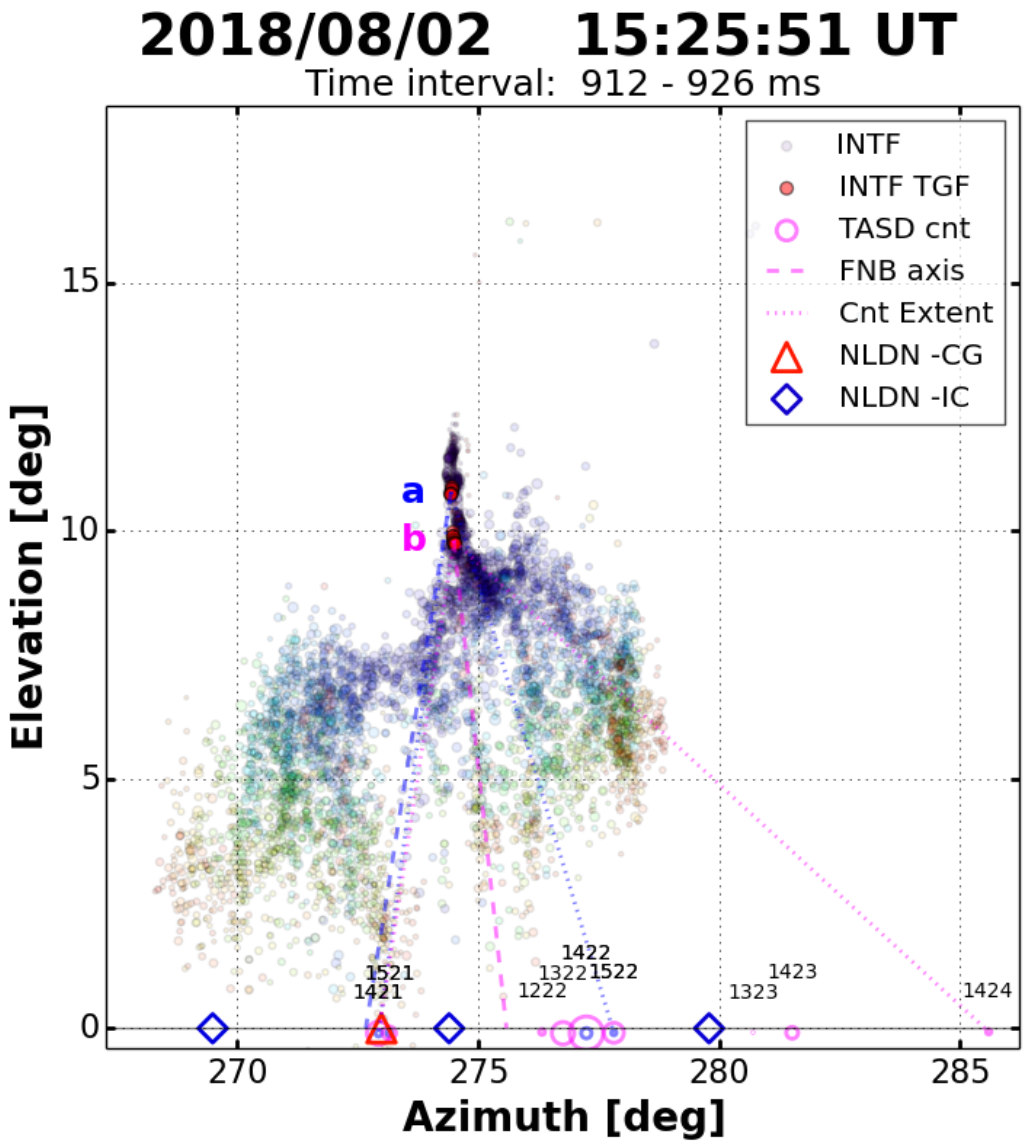

Figure S21. Azimuth-elevation plots for TGF C. Same as Fig. S19, except for the relatively simple and conical TGF C of Figure 5c. The simplicity is seen in the vertically-downward development of the INTF sources. Of interest in this and the other TGFs, the main TGF of each flash (event *a* of TGF A, the only event of TGF B, and event *b* of the present TGF) are all produced by the strongest IBP of the flashes, which occur as the INTF sources start to broaden out, indicative of the onset of branching. After that, the IBPs begin to weaken, suggesting the IBPs are strongest up until branching starts. The weakened IBPs can also produce gamma bursts, however, as seen in TGF A, where the second, weaker gamma event (*b*) occurred $\simeq$100 μs after the main (*a*) trigger and further into the branching (Fig. S19).

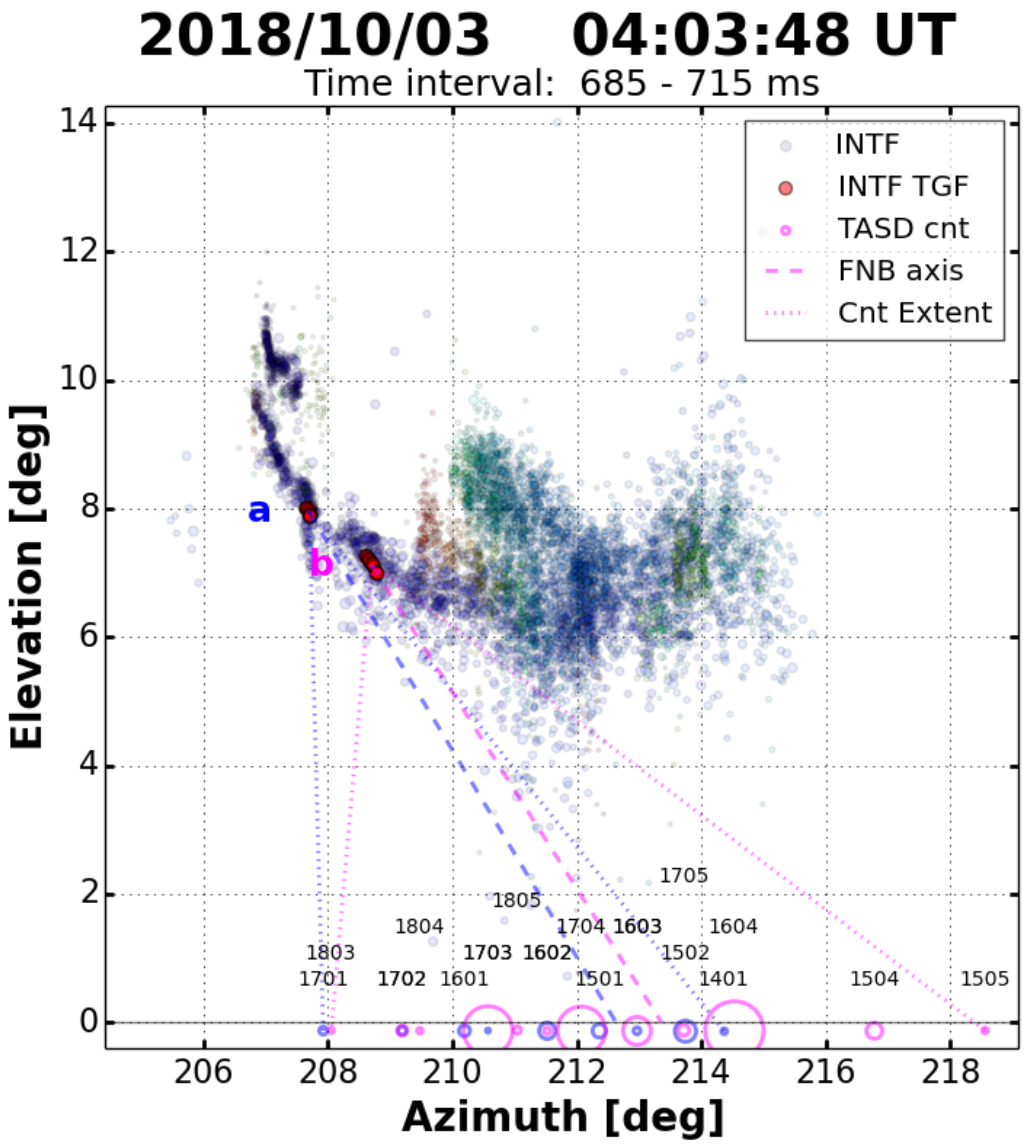

Figure S22. Azimuth-elevation plots for TGF D. Same as Fig. S19, except for TGF D during the strongly-tilted, low-altitude IC flash of Figure 5d. Again, the strongest IBP and TGF occurred at the lowest exent of the downward negative breakdown before it started branching. The flash occurred in a late-season nocturnal storm that had a more complex electrical structure, as indicated by the disjointed nature of the downward negative breakdown before entering the storm's offset lower positive charge region. The IBP that generated the TGF had the longest duration ($\simeq$15 μs) and extent (240 m vertical component—but longer due to being oriented $\simeq 30°$ from vertical).

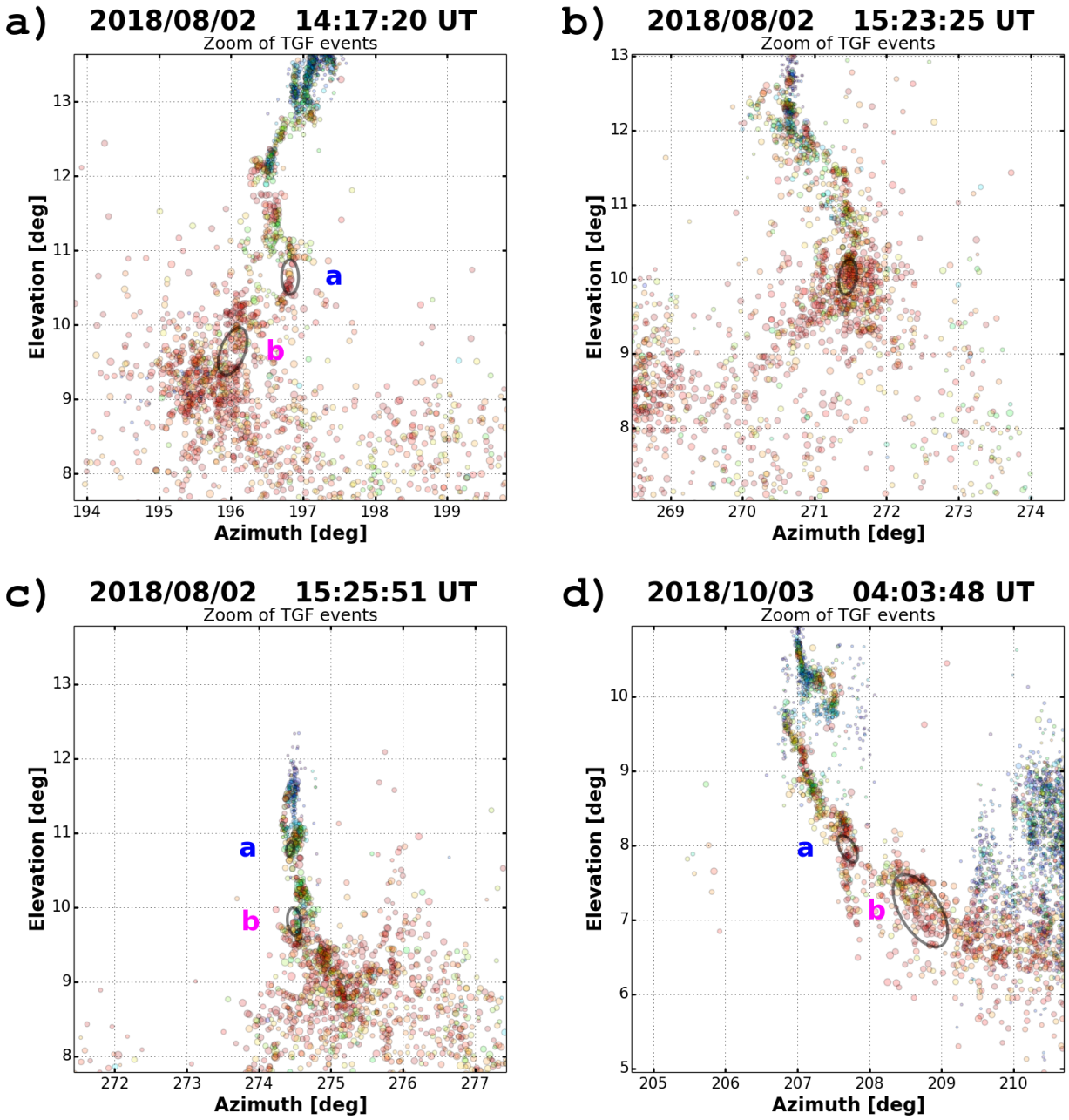

Figure S23. Zoomed azimuth-elevation plots. 6x6 degree view of TGFs A–D. The location of the VHF sources for each TGF trigger are indicated by the ellipses. All VHF sources are rainbow color-coded from blue to red according to increasing power, rather than according to time as in Figures S19–S22.

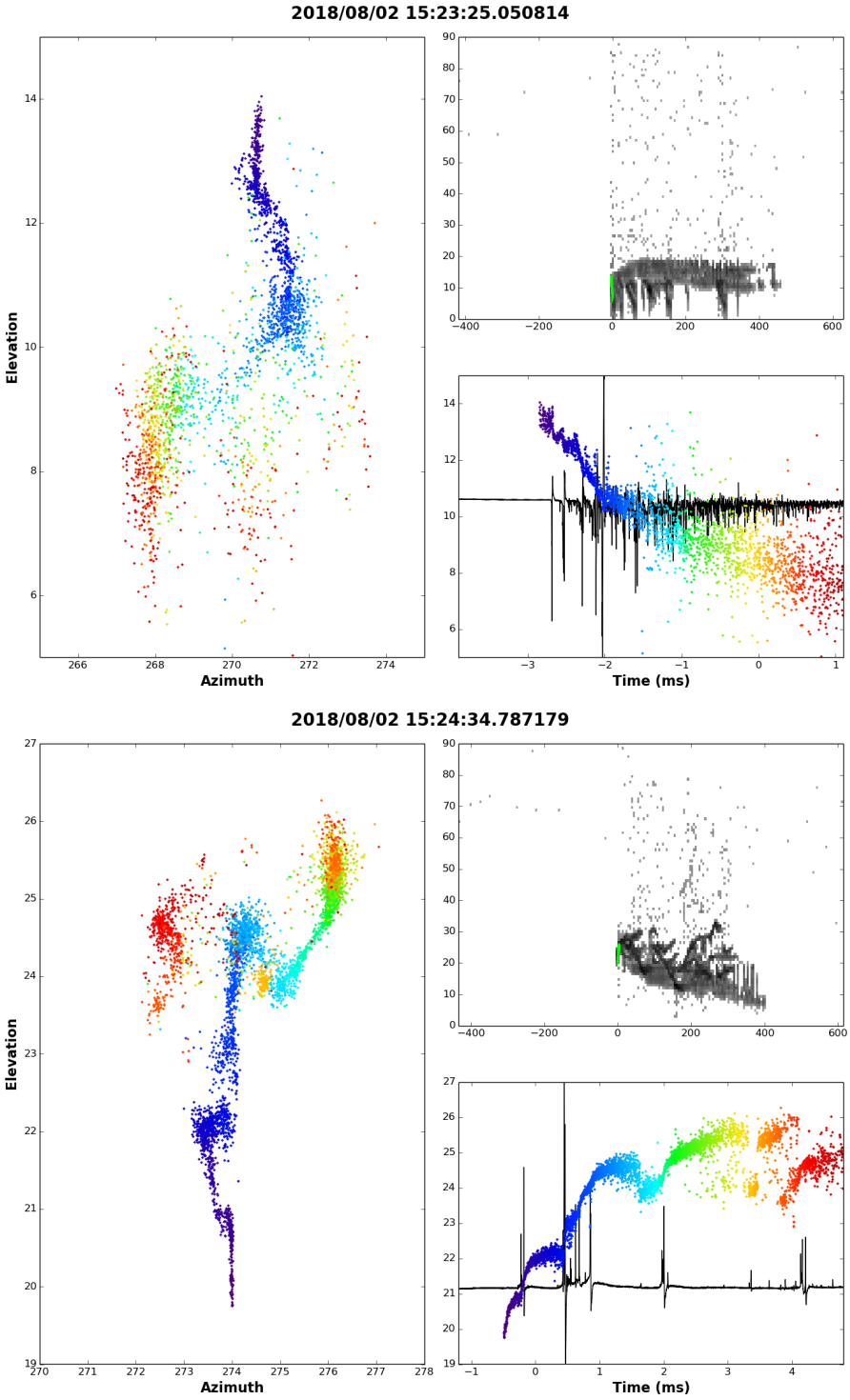

Figure S24. Comparison of –CG and IC flashes. INTF observations of the initial few milliseconds of the –CG flash that initiated TGF B (top panels) and an IC flash that occurred 69 s later in the same storm (bottom panels). For each flash the temporal development is color-coded from blue to red, with the time scale being approximately the same for both flashes. The upward stepping is well-delineated in the elevation vs. azimuth and elevation vs. time plots for the IC flash, and more continuous for the –CG flash. The stepping lengths were ≃350, 350, and

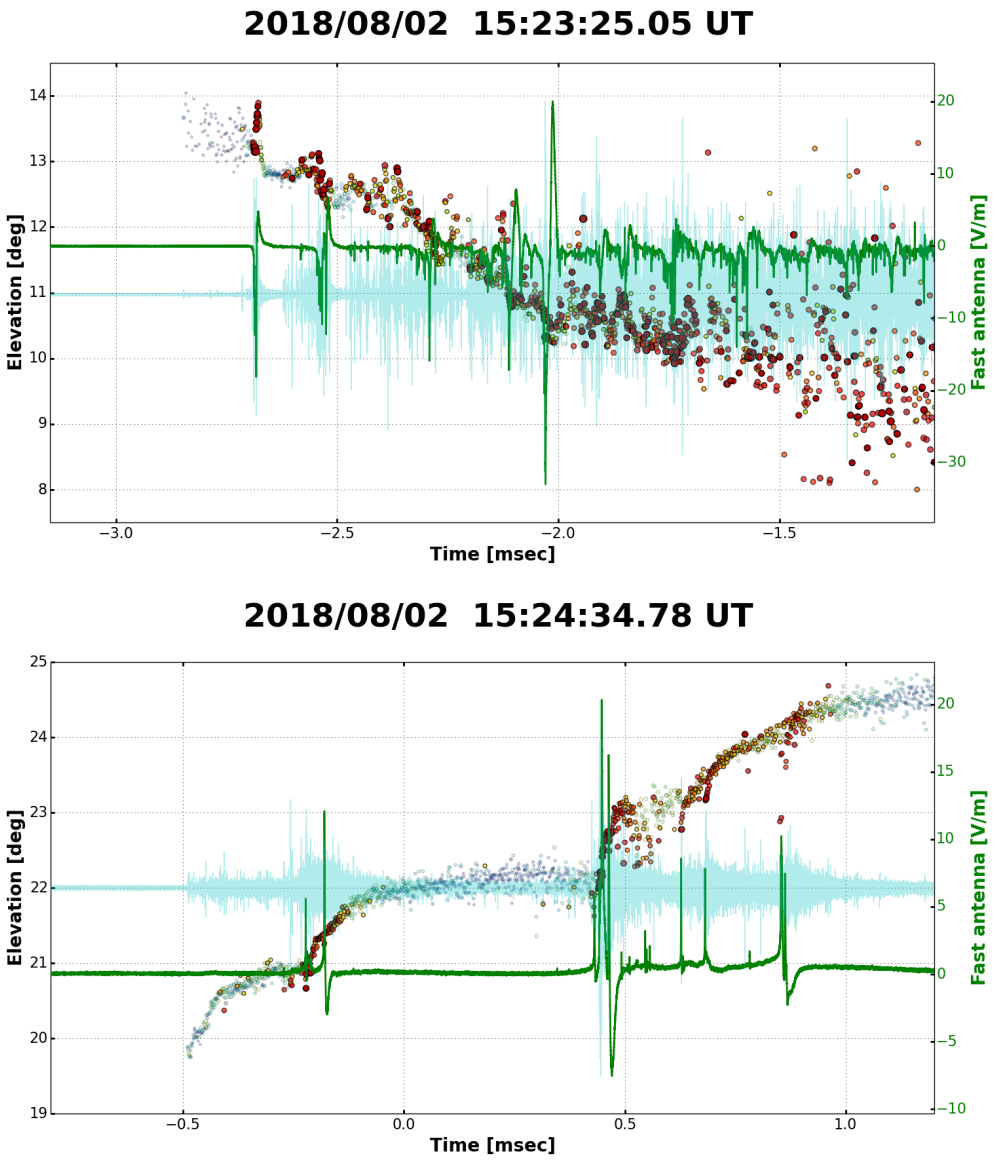

Figure S25. Two millisecond zoom plots. Same as the lower right panels of Fig. S24, but showing the first ≃1.5 ms of each flash, illustrating how –CG flashes develop rapidly and continuously, while IC flashes develop more intermittently, with longer-duration steps and complex sequences of IBPs and sub-pulses. Each of the two IC steps was initiated by an IBP produced by fast negative breakdown having speeds of ≃1–2 $\times 10^7$ m/s, with the second, complex IBP and sub-pulse sequence lasting ≃500 μs.

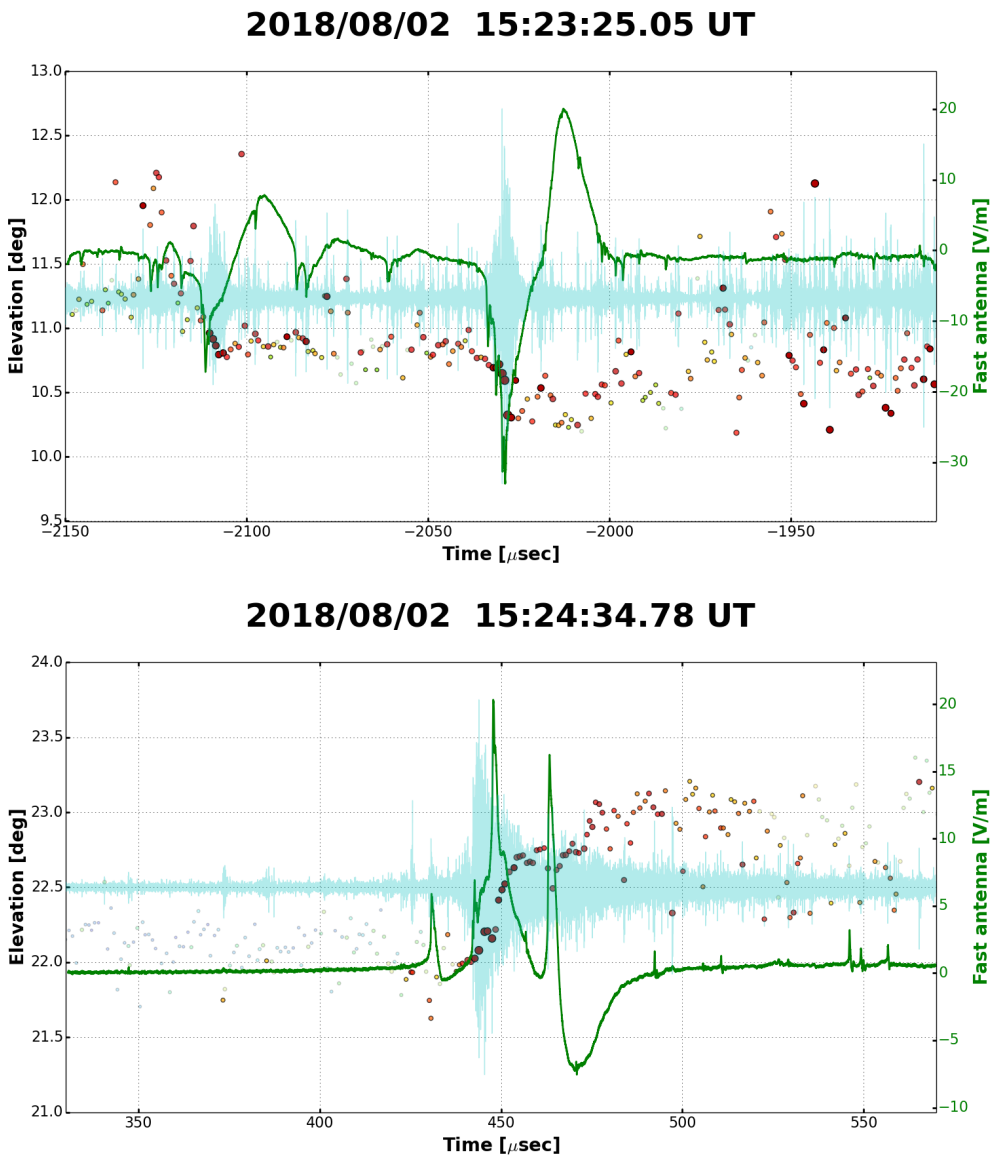

Figure S26. 240 microsecond zoom plots. Comparison of the largest IBPs of the –CG and IC flashes in Fig. S25. In both cases the IBP was produced by fast negative breakdown, having speeds of 1–2 [7] m/s. The sub-pulses of the IC IBP were noticeably stronger and more impulsive than those of the –CG flash, which initiated TGF B. Note the onset of strong VHF radiation at the beginning of the FNB, and sub-pulses occurring both before and during the opposite-polarity field change of the IBP. The overall duration of the IC IBP sferic was somewhat longer than that of the –CG flash, being ≃60 and 40 μs, respectively.

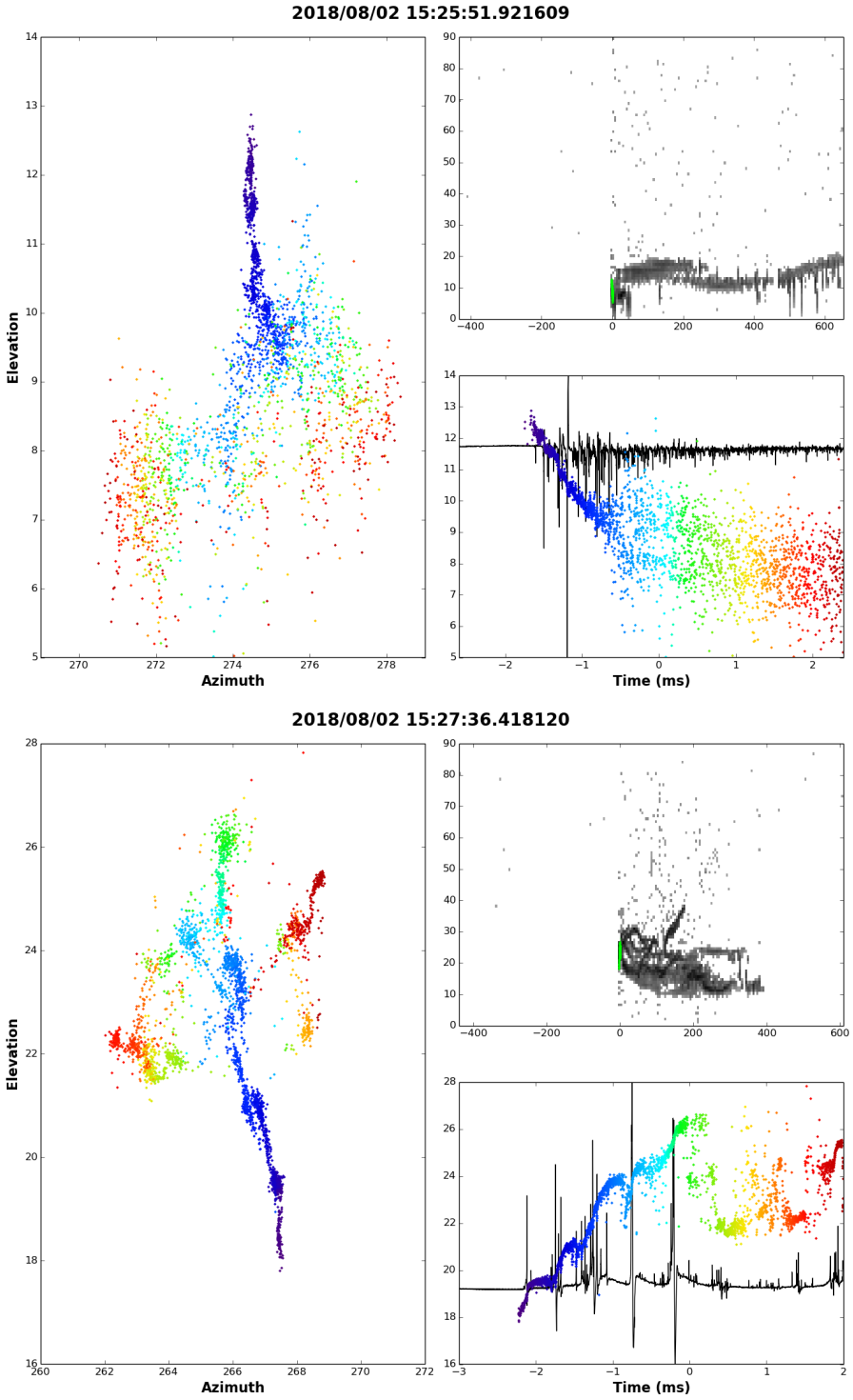

Figure S27. Primary IC/CG flash comparison. Same as Fig. S24, except providing overviews of the –CG flash that initiated TGF C (top panels) and the following IC flash in the storm (bottom panels), corresponding to the examples of Figures 6 and 7 of the main text. Of particular note in both this IC and that of Figure S24 is that the strongest IBP occurred as the upward negative breakdown started to branch out, at which point the strong IBPs abruptly started dying out (lower right panel of the IC). The same observation has been noted in connection

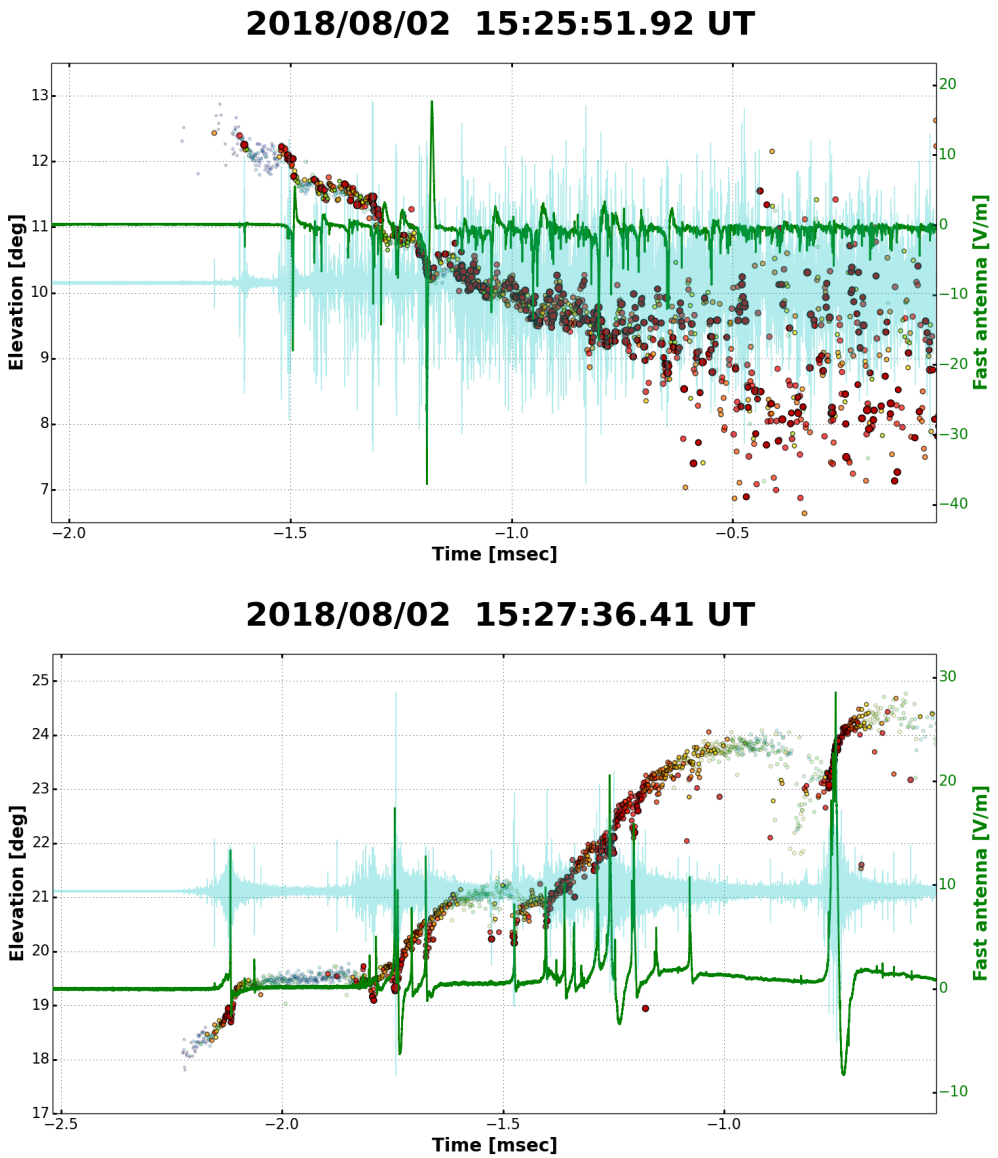

Figure S28. Two millisecond IC/CG comparisons. Same as Fig. S25 and enlarged versions of the top two panels of Figure 6 of the main text, illustrating the complex sequences of the initial breakdown during the post-TGF C IC flash and the role of high-power negative streamer breakdown and sub-pulses in the upward negative breakdown of the IC (see Section 3.2 of the main text). As in the IC/CG comparison of Figure S24, the stepping lengths of the IC were longer than those of TGF C, being ≃400, 570, and 1000 m for the first three IC steps, vs. ≃140 and 180 m for the two largest steps of TGF C's –CG.

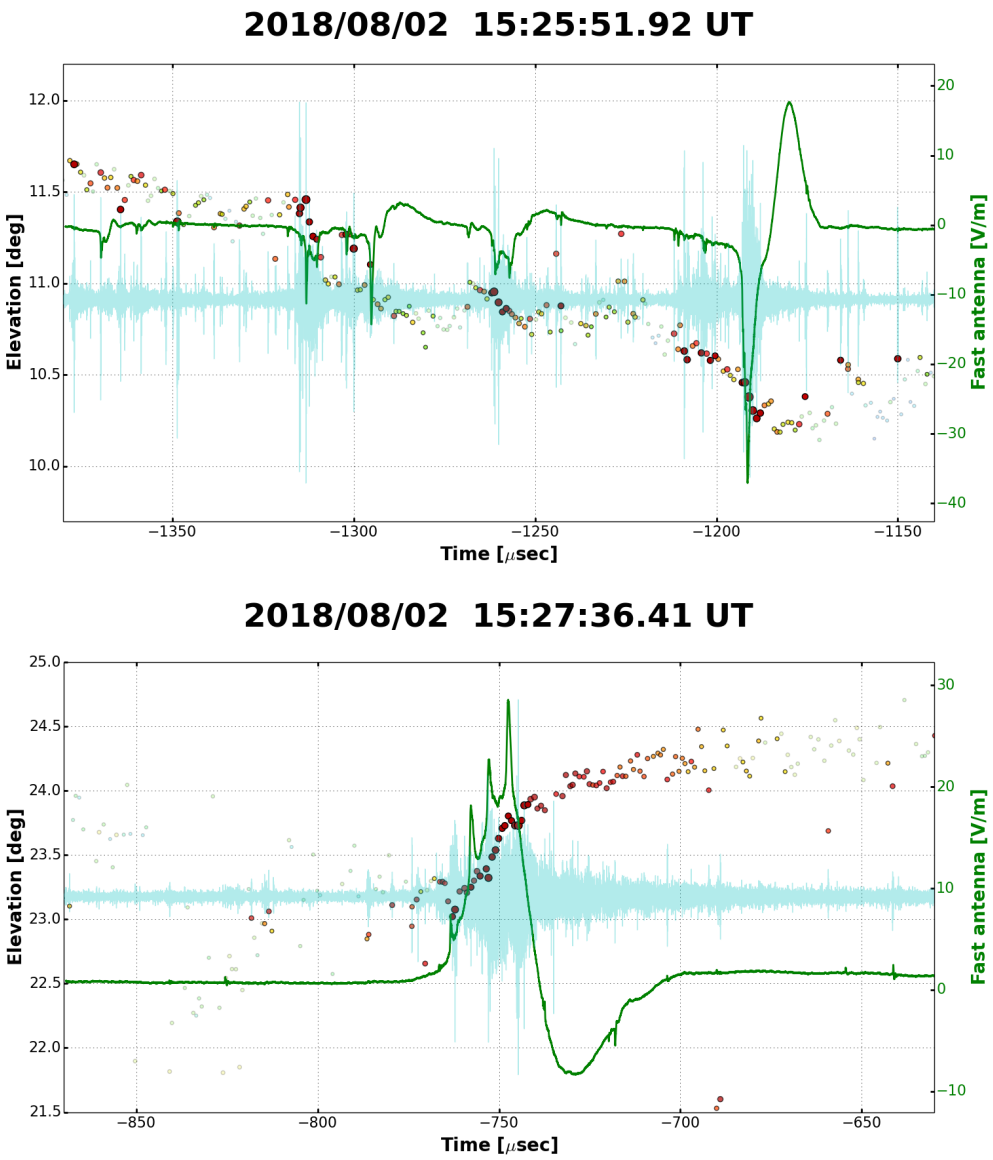

Figure S29. 240 microsecond plots. Comparison of the fourth IBP of the IC flash of Fig. S28 (bottom panel) with the IBP of TGF C (right-hand side of top panel), showing how the IC IBP is substantially stronger in amplitude, duration and in the strength and impulsiveness of the sub-pulses, but is otherwise produced by the same basic process of FNB having embedded sub-pulses. Like TGF C's IBP, the IC's FNB is similarly fast (1.5 $\times 10^7$ m/s) and is initiated with brief fast positive breakdown (in this case downward). Note that the earlier gamma event of TGF C (Figs. S8 and S12c,f) was produced by the relatively weak sferic and FNB event at about –1310 μs in the top panel, indicating how even weak FNB can produce gamma-producing avalanching.

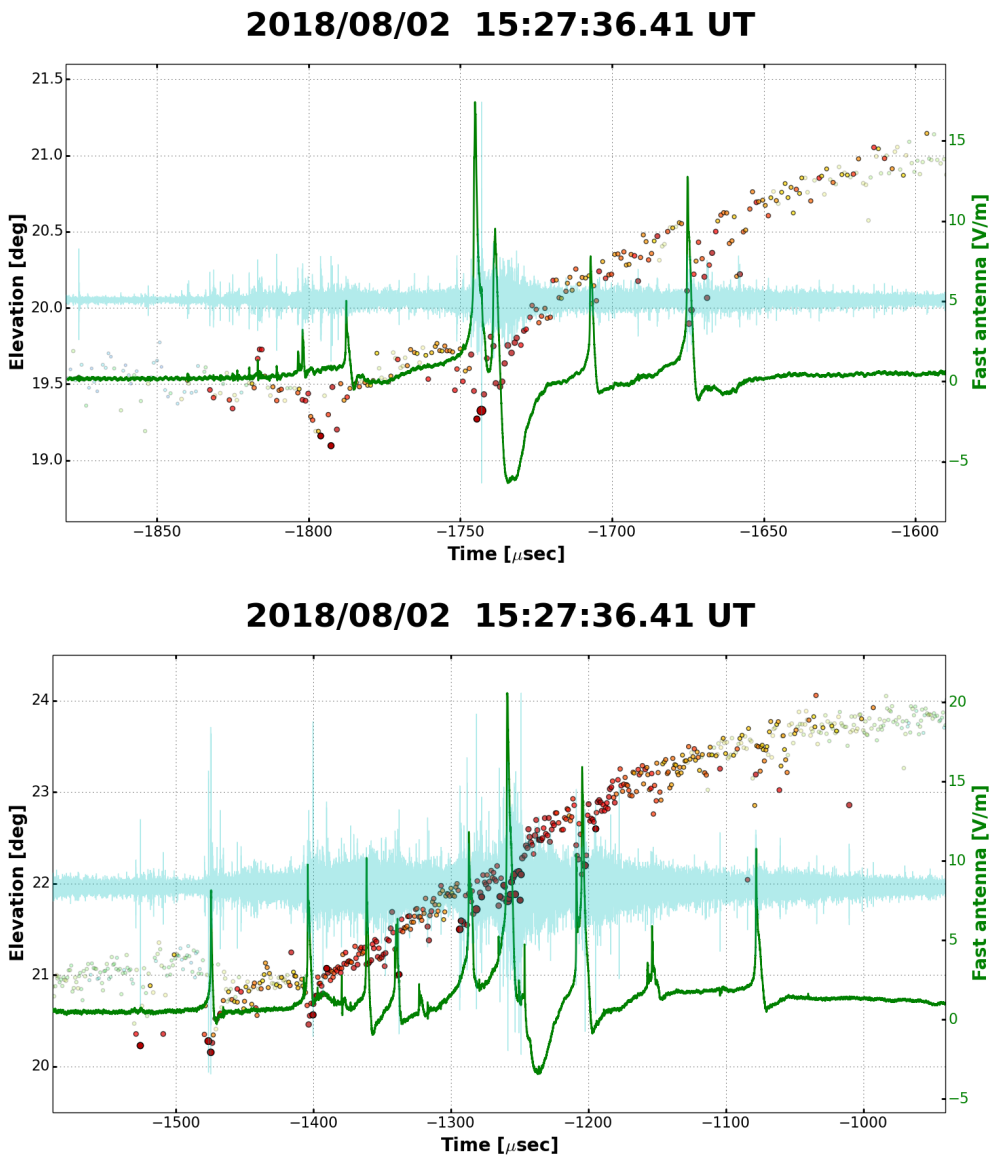

Figure S30. Complex IBP/sub-pulse events. Expanded views of the two complex IBP/sub-pulse sequences of the post-TGF C intracloud flash of Fig. S28 and Figure 7 of the main text. The FNB breakdown of the IBPs and the sub-pulses are each embedded in continuous upward negative streamer breakdown having a propagation speed of $\simeq$2–3 $\times 10^6$ m/s, showing that negative streamer breakdown doesn't have to travel at speeds of 10^7 m/s to produce the sub-pulse sparks. The overall durations of the sferics are $\simeq$130 and 400 μs, respectively, with the first complex event being very similar to that of a Florida IC flash that produced a satellite-detected TGF of 50 μs duration (Sections 3.2 and 3.3 of main text).

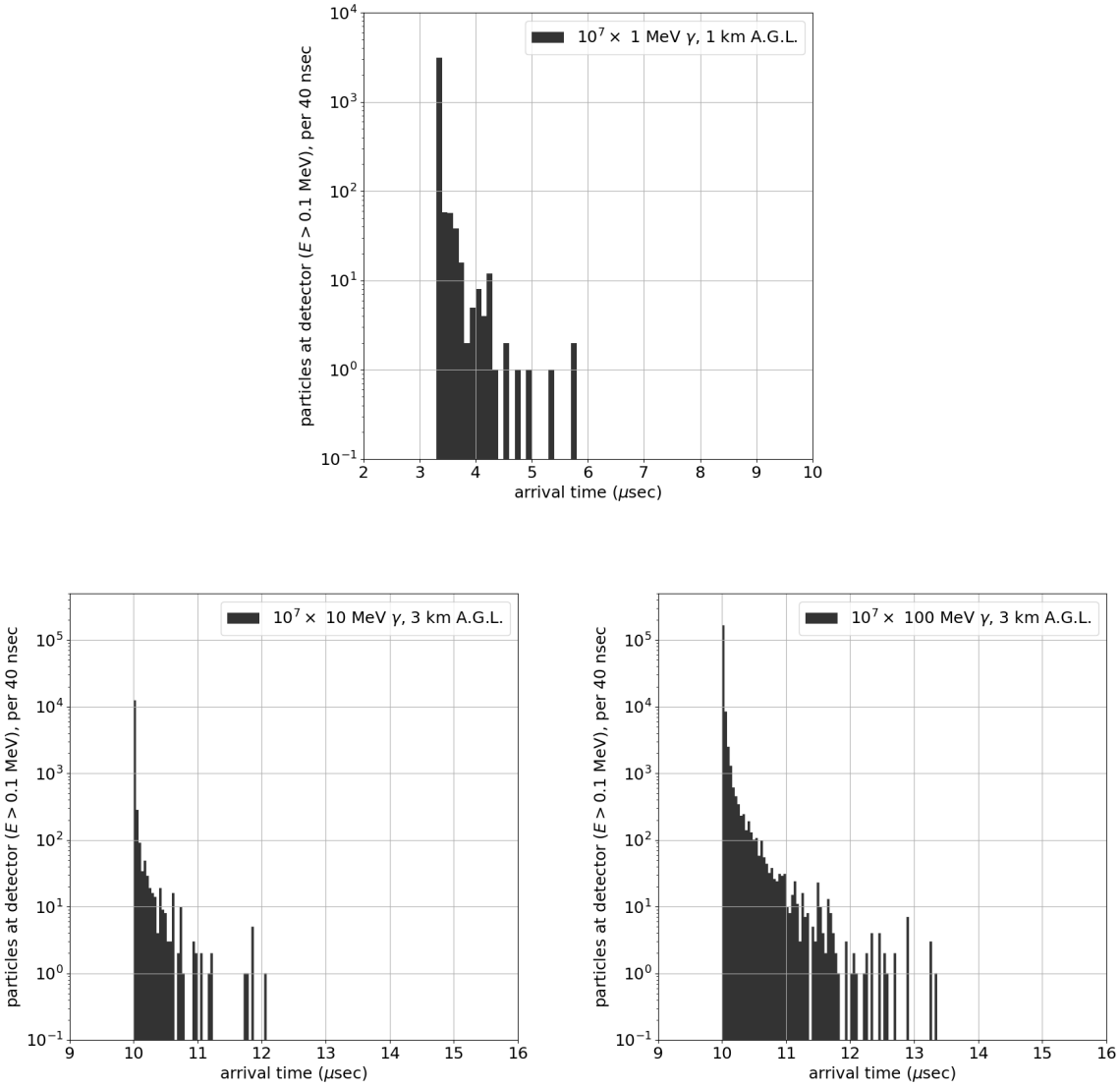

Figure S31. GEANT4 simulation of the effects of Compton scattering, pair production, and bremsstrahlung on the time-of-arrival of gamma ray showers. The lower panels with 10 and 100 MeV photons were generated 3 km above ground level; 1 MeV photons (upper panel) will not produce detectable energy deposit from 3 km, and so were generated at 1 km. In each simulation, 10^7 monoenergetic photons were generated in air at the center of a spherical (in order to remove geometric effects) "detector" of radius 3 km (1 km for 1 MeV case). Particles were scored at the detector if their energies exceeded 0.1 MeV, corresponding to the minimum detectable energy deposit above background (Abbasi et al., 2018). 95% of particles arrive within 20 ns (60 ns) for 10 MeV (100 MeV) primary photons, and within 40 ns for 1 MeV. We conclude

that temporal structure in the TASD waveforms on longer time scales is indicative of the intrinsic

Date	Time	μsec	LMA dBW	NLDN I_{pk}	TASD energy sum VEM/MeV	Number of TASDs
2018/08/02	14:17:20	616655	20.3			
		848		-10.0 kA C		
		851	21.5			
		981		-36.7 kA C		
		987	27.7			
		994			561/1150	9
		617094	27.2			
		104			192/393	8
		191	20.3			
		288		-12.0 kA C		
		294	27.6			
		444	21.8			
2018/08/02	15:23:25	042253	25.4			
		255		-10.9 kA C		
		259		+12.0 kA C		
		279		-3.1 kA C		
		329		-26.9 kA C		
		332	27.2			
		341		-30.1 kA C		
		341			112/229	12
		416	18.1			
		459		-7.6 kA C		
2018/08/02	15:25:51	913524	4.9			
		615		-6.4 kA C		
		633	15.3			
		816	20.1			
		825			35/72	5
		832		-5.0 kA C		
		937		-21.7 kA C		
		938	26.7			
		942			212/434	8
		914016	14.4			
		076		-5.9 kA C		
2018/10/03	04:03:48	687336	22.2			
		696	23.2			
		688177	26.1			
		200	22.0			
		346	24.6			
		436			100/205	9
		508	31.8			
		584			440/902	12
		599	30.5			

Table S1. Quantitative event values. Quantitative values of the LMA, NLDN, and TASD observations for the flashes of TGFs A,B,C,D, during the initial 1–2 ms of the flashes. Shown are the times of the LMA, NLDN, and TASD events [μs], the VHF source powers of the LMA sources [dBW], the peak currents I_{pk} of the NLDN detected events [kA], the sum total energy deposited in all adjacent surface detectors triggered by the gamma bursts, in [VEM] and [MeV], and the number of TASDs contributing to the total. TASD times reported here are the time of detection at ground level, delayed by propagation from the source. LMA and NLDN times correspond to the time of the source itself.

Event	SD	θ_c (deg)	z_a (km)	t_c (μs)	Δt_b (μs)	U/L ratio
TGF A	2208	**10.73 ± 0.03**	**3.21 ± 0.03**	**617,039.2 ± 0.7**	45.2 ± 0.4	1.5 ± 1.0
	2206	10.73 ± 0.03	3.21 ± 0.03	617,039.2 ± 0.9	45.1 ± 0.7	0.6 ± 0.3
	2308	10.73 ± 0.03	3.21 ± 0.03	617,039.1 ± 0.6	45.9 ± 0.3	**1.0 ± 0.6**
	2209	10.73 ± 0.03	3.21 ± 0.03	617,039.3 ± 0.7	42.6 ± 0.3	0.7 ± 0.4
	2307	10.79 ± 0.03	3.23 ± 0.03	617,038.3 ± 0.6	46.9 ± 0.4	1.0 ± 0.6
	2409	10.71 ± 0.02	3.21 ± 0.03	617,041.1 ± 0.6	43.6 ± 0.1	1.4 ± 0.9
	2207	10.73 ± 0.03	3.21 ± 0.03	617,039.8 ± 0.8	45.9 ± 0.5	1.6 ± 0.9
	2408	10.76 ± 0.03	3.22 ± 0.03	617,038.7 ± 0.6	45.7 ± 0.2	0.9 ± 0.6
	2309	10.78 ± 0.03	3.23 ± 0.03	617,038.6 ± 0.7	43.5 ± 0.2	0.8 ± 0.4
TGF B	1419	9.93 ± 0.03	2.91 ± 0.02	42,388.4 ± 0.4	45.0 ± 0.2	1.3 ± 0.8
	1421	10.06 ± 0.02	2.95 ± 0.01	42,384.0 ± 0.3	45.7 ± 0.2	1.0 ± 0.6
	1520	**9.96 ± 0.03**	**2.92 ± 0.02**	42,387.2 ± 0.3	44.35 ± 0.09	**0.9 ± 0.5**
	1320	9.87 ± 0.02	2.90 ± 0.02	42,391.0 ± 0.4	46.5 ± 0.3	0.3 ± 0.2
	1519	9.92 ± 0.02	2.91 ± 0.02	42,389.3 ± 0.4	43.8 ± 0.2	0.7 ± 0.5
	1620	9.96 ± 0.03	2.92 ± 0.02	**42,387.4 ± 0.4**	41.72 ± 0.05	3.0 ± 2.0
	1521	9.98 ± 0.02	2.93 ± 0.02	42,386.4 ± 0.3	44.1 ± 0.1	0.8 ± 0.6
	1621	9.96 ± 0.03	2.92 ± 0.02	42,387.2 ± 0.4	41.48 ± 0.07	0.4 ± 0.3
	1720	9.87 ± 0.02	2.89 ± 0.02	42,391.4 ± 0.4	38.58 ± 0.03	1.6 ± 1.0
TGF C	1424	9.94 ± 0.01	2.80 ± 0.01	913,983.5 ± 0.3	39.9 ± 0.2	2.9 ± 2.3
	1521	**9.83 ± 0.03**	**2.77 ± 0.01**	913,989.4 ± 0.2	43.70 ± 0.05	1.4 ± 1.0
	1522	9.83 ± 0.03	2.77 ± 0.01	913,989.4 ± 0.2	43.45 ± 0.07	**1.0 ± 0.7**
	1421	9.83 ± 0.03	2.77 ± 0.01	**913,989.6 ± 0.2**	44.7 ± 0.1	0.9 ± 0.5
	1423	9.85 ± 0.02	2.78 ± 0.01	913,988.9 ± 0.3	42.6 ± 0.2	2.3 ± 1.7
	1422	9.83 ± 0.03	2.77 ± 0.01	913,989.6 ± 0.2	44.4 ± 0.1	0.9 ± 0.5
	1323	9.77 ± 0.03	2.75 ± 0.01	913,991.3 ± 0.3	42.2 ± 0.2	0.8 ± 0.5
	1322	9.81 ± 0.03	2.76 ± 0.01	913,990.0 ± 0.2	43.9 ± 0.2	1.0 ± 0.5
	1222	9.78 ± 0.03	2.76 ± 0.01	913,991.0 ± 0.3	42.0 ± 0.2	10.6 ± 6.6
TGF D	1704	7.20 ± 0.02	3.02 ± 0.04	688,680.1 ± 1.4	69.3 ± 0.8	1.0 ± 0.6
	1603	7.20 ± 0.02	3.02 ± 0.04	688,680.1 ± 1.5	68.7 ± 1.1	0.7 ± 0.5
	1705	**7.19 ± 0.02**	**3.02 ± 0.04**	**688,680.2 ± 1.4**	67.3 ± 0.6	1.0 ± 0.6
	1702	7.21 ± 0.02	3.03 ± 0.04	688,679.9 ± 1.7	69.5 ± 1.3	4.0 ± 3.0
	1805	7.16 ± 0.03	3.01 ± 0.04	688,681.0 ± 1.3	67.3 ± 0.3	6.8 ± 6.4
	1703	7.20 ± 0.02	3.02 ± 0.04	688,680.1 ± 1.4	70.2 ± 1.0	1.4 ± 1.0
	1803	7.17 ± 0.02	3.01 ± 0.04	688,681.0 ± 1.3	70.2 ± 0.8	1.0 ± 0.7
	1504	7.17 ± 0.02	3.01 ± 0.04	688,680.9 ± 1.6	65.7 ± 1.1	**1.1 ± 0.7**
	1804	7.14 ± 0.03	3.00 ± 0.04	688,681.7 ± 1.3	69.4 ± 0.5	1.8 ± 1.2
	1602	7.19 ± 0.02	3.02 ± 0.04	688,680.1 ± 1.7	68.1 ± 1.4	0.9 ± 0.6
	1604	7.21 ± 0.02	3.03 ± 0.04	688,679.9 ± 1.5	67.9 ± 1.0	1.4 ± 1.0
	1505	7.16 ± 0.03	3.01 ± 0.04	688,681.1 ± 1.6	64.1 ± 1.1	0.6 ± 0.4

Table S2. Calculated source values. Converged iteration values and associated uncertainties for each TGF, calculated independently for each surface detector. SD is the surface detector's identifying number XXYY identifying their easterly (XX) and northerly (YY) locations within the array in 1.2 km grid spacing units. θ_c is the elevation angle corresponding to z_a, which is the source altitude (above a reference plane of 1.4 km). t_c is the determined microsecond of TGF signal arrival at the INTF and Δt is the relative timing difference between INTF and SD signals, and U/L Ratio is the ratio of energy deposit between upper and lower levels of scintillator. Values in bold are the medians for that column and indicate the burst's median onset time/elevation.

Event	D (km)	z_a (km)	t_a (μs)	$\Delta\theta_{FNB}$ (deg)	Δz_{FNB} (m)	Δt_{FNB} (μs)	v_{FNB} (m/s)
TGF A	16.96 ± 0.15	3.21 ± 0.03	616,981.7 ± 0.6	0.55	150	10.0	1.5×10^7
TGF B	16.64 ± 0.08	2.92 ± 0.02	42,331.7 ± 0.3	0.32	100	3.7	2.7×10^7
TGF C	15.98 ± 0.04	2.77 ± 0.01	913,935.1 ± 0.2	0.40	120	4.7	2.6×10^7
TGF D	23.9 ± 0.3	3.02 ± 0.04	688,600.1 ± 1.4	0.56	240	13.4	1.8×10^7

Table S3. Observed fast breakdown characteristics. Extent and duration of fast breakdown occurring during the brightest event for each of the four TGFs, specified by the first column. Second column gives D, the plan distance between each TGF and the INTF. The third column z_a is the median altitude result of the iteration process (Table S2). The fourth column, t_a, is the reconstructed source time. $\Delta\theta_{FNB}$ is the angular extent of downward breakdown which, combined with D, gives the propagation distance, Δz_{FNB}. The fifth column, Δt_{FNB}, is the breakdown's duration in time, which allows for an estimation of the fast breakdown speed shown in the final column v_{FNB}. Note that the final four columns do not include uncertainties, as their values are estimated by simply assuming a linear descent of FNB based on data shown in Figure 4 (and Figures S15-S18).